MAGNETIC RESONANCE IMAGING OF STRUCTURE AND COARSENING IN THREE-DIMENSIONAL FOAMS

A Dissertation

Submitted to the Graduate School
of the University of Notre Dame
in Partial Fulfillment of the Requirements
for the Degree of

Doctor of Philosophy

by

Burkhard A. Prause, B.A.

James A. Glazier, Director

Department of Physics
Notre Dame, Indiana
March 2000

MAGNETIC RESONANCE IMAGING OF STRUCTURE AND COARSENING IN THREE-DIMENSIONAL FOAMS

Abstract

by

Burkhard A. Prause

The rate of growth of individual bubbles in three-dimensional liquid foams (and crystallites in polycrystalline metals) is a major unsolved problem in material science. We have used Magnetic Resonance Imaging (MRI) to observe nondestructively the structure of disordered liquid foams. Volumetric imaging of coarsening foams required a robust imaging method with sufficient spatial and temporal resolution to resolve the small liquid accumulations in the foam's Plateau borders. We have developed an MRI technique to optimize the image quality for foams with very low liquid fraction. The series of three-dimensional images we acquired provides unique insight into the evolution of foams over up to four days of evolution. Automated computerized analysis provides bubble locations, sizes, and the number of faces per bubble. We tracked individual bubbles between data runs to determine that the volume rate of change of a bubble as a function of its number of faces agrees with Glazier's proposed growth law for three-dimensional grains. Manual extraction of vertex locations for several hundred bubbles provided exact bubble shapes and sizes, as well as the relation between a bubble's number of faces and volume.

This thesis is dedicated to Java, my wonderful cat and friend who spent endless hours with me on this project, and who died much to soon.

CONTENTS

TABLES

FIGURES

ACKNOWLEDGEMENTS

I am most grateful to my advisor, Dr. James Glazier, who has given me the opportunity to pursue this extraordinary project. I thank him for putting so much trust in me, and for his patience and encouragement.

I thank Dr. Samuel Gravina at Bruker Instruments, Dr. Greg Karzcmar at the University of Chicago and Dr. Carlo Montemagno at Cornell University. They were the first to attempt to acquaint me with the difficult subjects of MRI and image analysis. I owe tremendous gratitude to Dr. Steve Gibbs at the National High Magnetic Field Laboratory, and Dr. Dieter Gross at Bruker Analytik, for letting me abuse their MRI systems, while they patiently helped me to improve my skills. I deeply appreciate the support and advice of Dr. Gerald Jones and Dr. Bruce Bunker during this project, and Dr. Peter Schiffer's trusting me to use his magnetometer.

Sanity and intellectual stimulation rely on many good friends and colleagues. I was privileged to have both. Thank you Arpita, Sridhar, Mark and Igor, for many helpful discussions and for your friendship. Especially the ones involving a healthy dose of beer, whiskey or window cleaner. Special thanks go to Rob, who lent his friendship unconditionally, no matter how much I abused it. I love my parents for trusting and supporting me through these long years.

Finally I thank my wonderful wife Jacqueline, who has supported, encouraged, counseled and loved me for these long years.

CHAPTER 1

THREE-DIMENSIONAL FOAMS

1.1 Overview

This thesis discusses an experimental investigation of the structure and growth dynamics of three-dimensional liquid foams.

Foams are macroscopically structured materials, in which a network of vertices, edges, and sometimes faces (in all liquid foams, and some solid foams) separate individual domains. This organization at a level above molecular organization makes foams non-Newtonian, and interfacial phenomena at the cell level dominate during unperturbed evolution, as well as during deformation [6, 7, 8]. These properties apply to a whole class of materials, in which relaxation and a gradual approach to equilibrium determine the evolution [9].

All cellular patterns share a common structure; a network of boundaries that divide space into individual, distinguishable domains. Such patterns can be observed in many disciplines. Territorial patterns and cellular structures in tissues are examples in biology [10, 11]. Geology and material science include examples such as basalt structures and crack networks [12, 13, 14], polycrystalline structures in metals and sintered ceramics [15].

Figures 1.1, 1.2, 1.3, 1.4 show a collection of cellular structures, ranging from the atomic length scale, to biological cells in two and three dimensions, to the

honeycomb-like structure of natural cork, to bubbles at the surface of a liquid foam. The commonality of shapes and structure is quite apparent.

In 1949 Lewis noted the similarity of shapes in biological cells and bubbles [16], after devoting nearly three decades to the study of biological cell shapes in two and three dimensions [17, 18, 4]. Three years later, at a metallurgy conference in Cleveland, C. S. Smith suggested using foams to model the annealing of metallic grains. He noted the similarity between the two materials, in which domains seek to minimize their surface areas over time [15].

Thus foams are prototypes for the structure and evolution of cellular materials. We will review some of the relevant recent literature in the following pages. The remainder of this introduction will review investigations of three-dimensional cell shapes, and the theories that are beginning to emerge on three-dimensional cellular dynamics. The discussion will at times include two-dimensional concepts and examples, because they are more easily illustrated and more intuitive.

A separate chapter on Magnetic Resonance Imaging (MRI) follows. The technology is sufficiently new and complex to require a thorough overview, which should illuminate its possibilities, as well as point out its weaknesses and limitations. To preserve a sense of chronology, Chapter 3 will then discuss the experiments we conducted using MRI to visualize liquid foams.

The process of finding and optimizing a technique to visualize liquid foams with MRI is daunting in itself. An equal challenge is finding a method to extract the shapes and sizes of individual bubbles from these images. Chapter 4 will stray from the MRI theme of the previous chapters to discuss this analysis procedure in detail. While the chapter specifically deals with the processing of noisy three-dimensional MRI images and the structural analysis of liquid foams, the techniques we use (some

of which we invented) apply to many materials and image analysis and enhancement problems. Chapter 5 presents and discusses the results of our experiments.

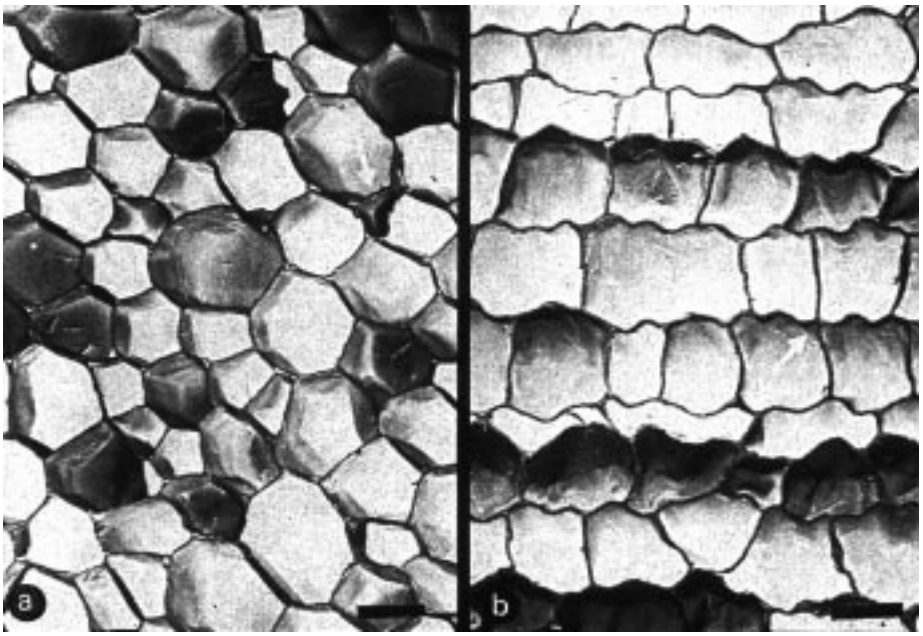

Figure 1.1. Scanning Electron Micrographs of Cork (from Pereira *et al.* [2]).

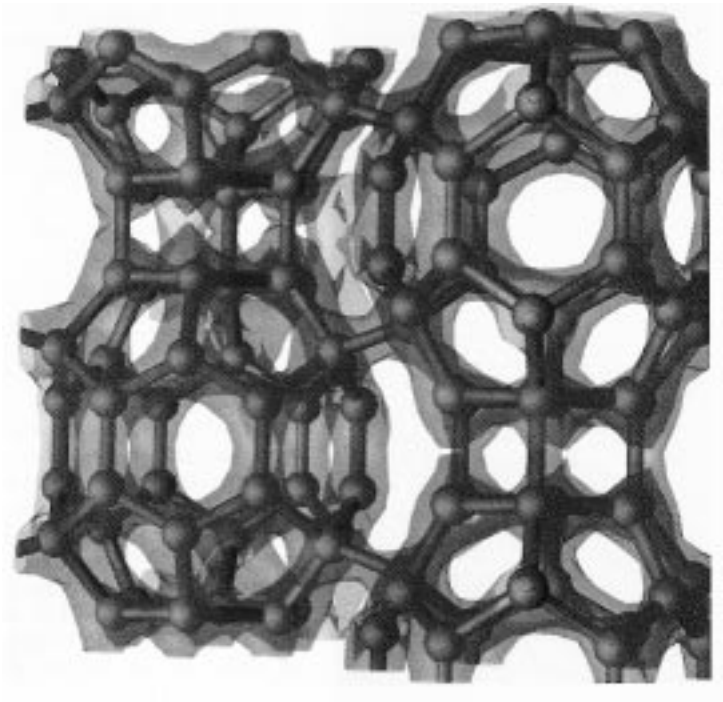

Figure 1.2. Rhombohedral C_{35} Structure: The carbon atoms and their surrounding electron clouds form a complex three-dimensional lattice structure (from Bernholc [3]).

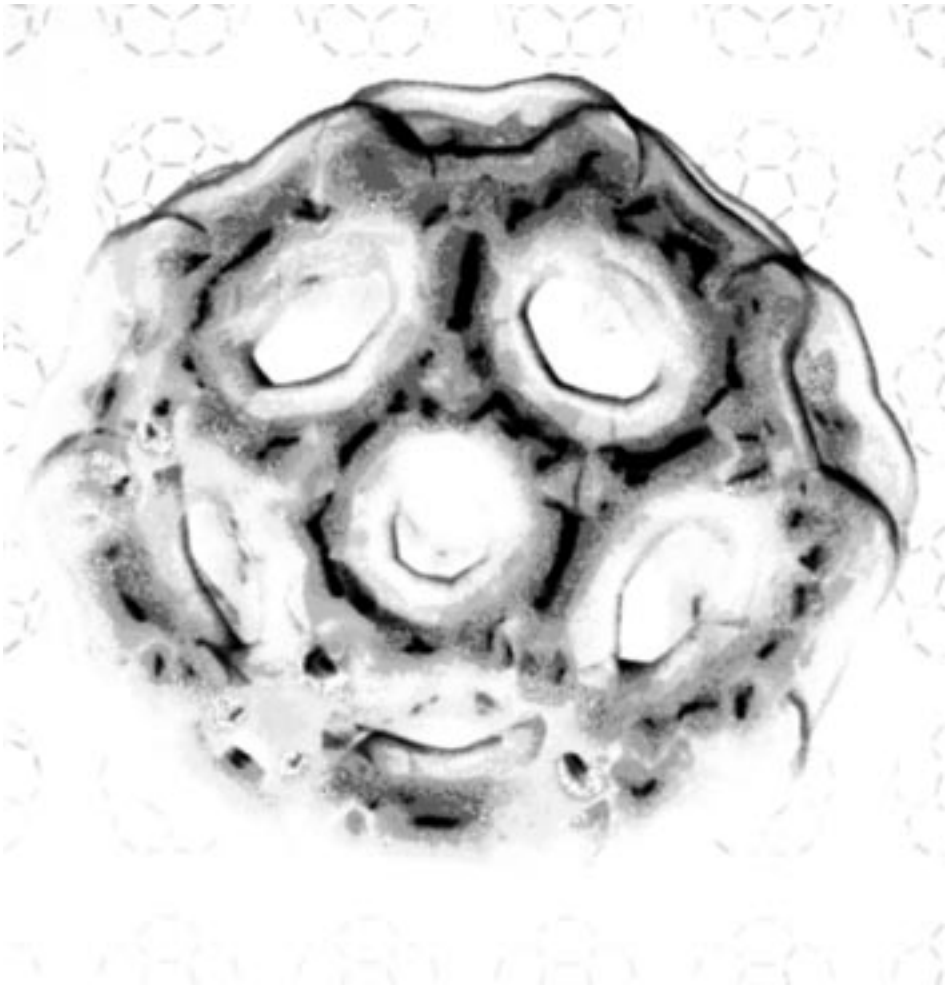

Figure 1.3. C_{60}(Buckyball) Atomic Structure: electron distribution clouds connect the carbon atoms sitting at the vertex locations of five- and six-sided polygons (from Bernholc [3]).

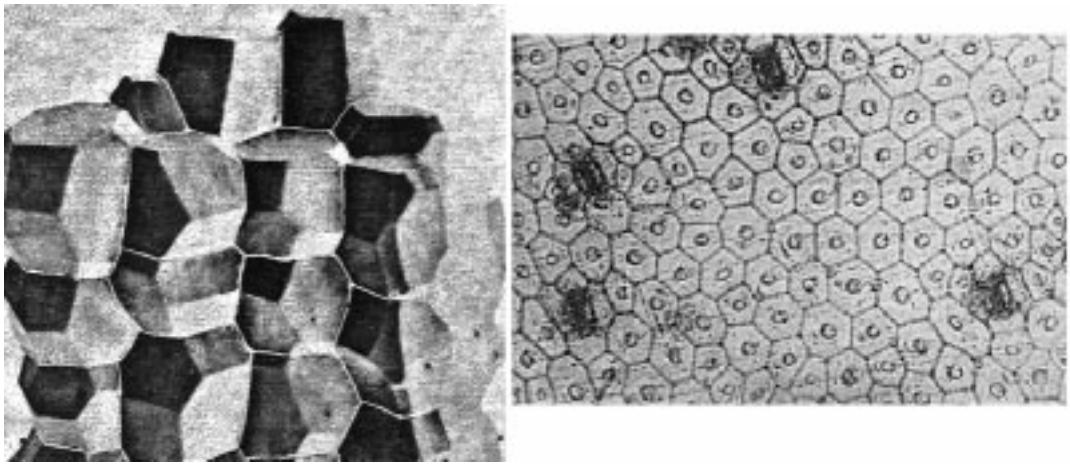

Figure 1.4. Biological Cells. Right: Interior cells of a common weed obtained from sectioning (from Lewis [4]). Left: Epidermal cells of undifferentiated vegetable tissue (from Mombach *et al.* [5].

1.2 Current Literature

The study of cellular patterns is well developed. An extensive review on cellular patterns (including computer simulations and theories related to the subject) by Jiang [19] in 1998 included some 800 publications, making it the most up to date and complete bibliography on the subject.

Scientific research into various aspects of patterns and pattern formation, as well as popular literature (including books for school children) are published frequently. This chapter summarizes the latest and most important works on bubbles and foams, which provide detail on specific subjects, or serve as an entry point for researchers trying to acquaint themselves with this field.

"The Self-Made Tapestry" by Philip Ball [20], published in 1999, gives numerous examples and beautiful illustrations of natural patterns, along with a wonderful narrative, outlining the history of scientific curiosity about patterns' origins. The book is easily readable, and while it covers a broad range of natural patterns, it

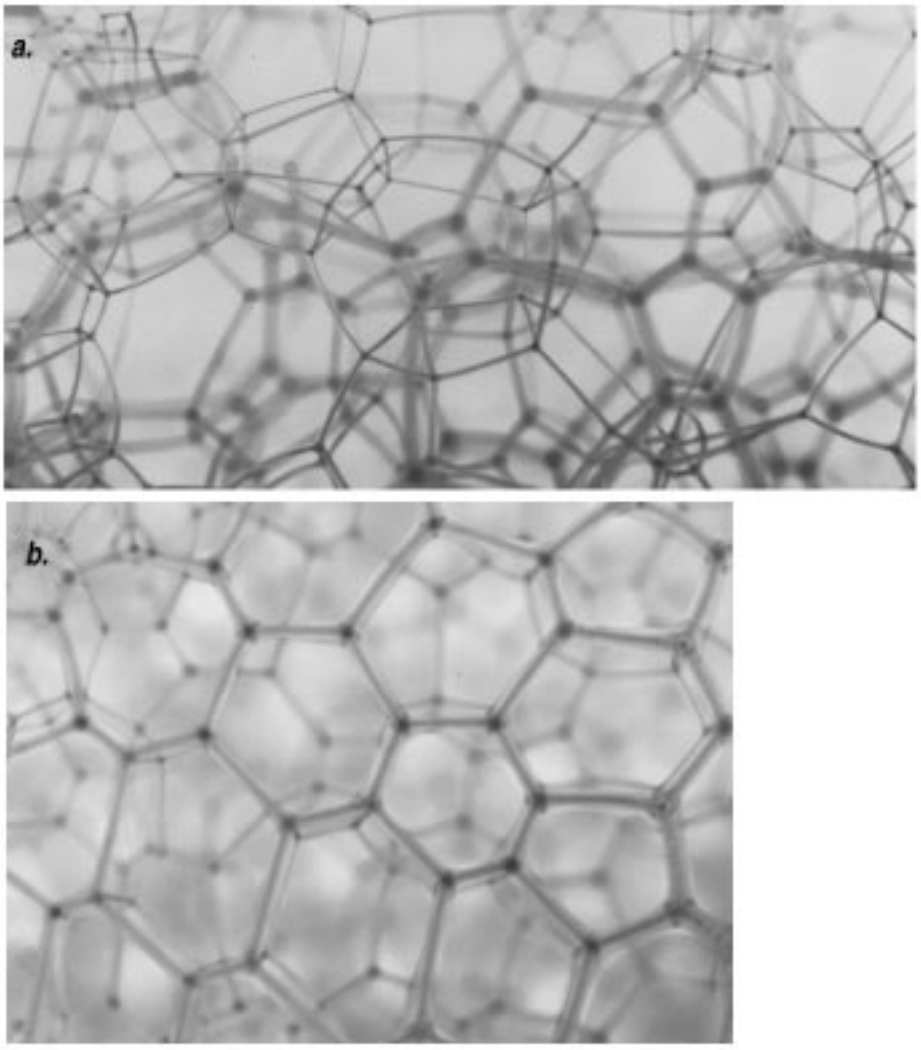

Figure 1.5. Liquid Foams: Images of bubbles in a liquid foam. a) Shows bubbles in the first and second layers. b) Focuses on the edges in contact with the outside wall of the container which resemble a quasi two-dimensional pattern.

devotes an entire chapter to bubbles, underlining the importance of bubbles as a tool for understanding many processes in general pattern formation.

Bubbles and soap films are the fascinating subject of children's books and early science education texts by Cassidy [21], Lovett [22], and Isenberg [23].

Rivier [24, 25] and Stavans [26] have published excellent reviews on the evolution of two- and three-dimensional cellular structures and their statistics. Glazier's thesis [9] is another outstanding overview of two-dimensional cellular patterns, while Jiang's dissertation [19] provides great detail on the state of computer simulations and theories about the dynamics of cellular patterns, again both in two and three dimensions.

Weaire *et al.* have investigated bubble shapes and minimal area partitions [27, 28, 29, 30, 31, 32, 33], vertex stability [34] and foam drainage [35, 36]. A 1996 book by D. Weaire, "The Kelvin Problem" [32] is the most current and complete study of the problem of space partitioning. Their research on the physics of foam dynamics and foam drainage has been summarized in the dissertations by Hutzler and Findlay [37].

Glazier [38], Weaire and Glazier [39] and Sire [40] have investigated the theory of growth in three-dimensional cellular patters. Monnereau's [41] confocal optical studies of bubbles in 1998 provided the first experimental measurements of three-dimensional coarsening of individual bubbles. de Almeida *et al.* [42] have developed a statistical model for three-dimensional scaling properties, which have previously been investigated experimentally by Durian *et al.* [43, 44, 45] and Gonatas *et al.* [46].

The relation between a foam's structure and its mechanical and rheological properties is important in many industrial applications of foams, as well as for modeling and understanding the properties of other cellular materials. Applications lend some urgency to the investigation of foam structure and evolution. The mechanical re-

sponse of bubbles to deformation has been studied by Reinelt and Kraynik [7, 8], while Kraynik [6] reviews the theory of foam flow, as well as range of applications which require detailed understanding of foam structure and dynamics.

1.3 Cellular Patterns

While the laws of thermodynamics imply increasing disorder for the universe as a whole, there are many places in nature, large and small, exhibit symmetry and order. Many of these patterns emerge from simple physical processes. Others, such as the territorial patterns of hunting and gathering species [10], require a more Darwinian explanation, while the multi-faceted physical origins of many ordered geological structures are the subject of ongoing speculation [12].

Many types of patterns exist, generated by the flow of rivers, wind ripples in the sands of deserts, chemical reactions, such as the Belousov-Zhabotinsky reaction and Turing patterns, or the abstract geometries of fractals (Ball [20] gives examples of many such patterns).

We will study patterns of a particular kind, a subset of *cellular* patterns, which derive their name from their resemblance to biological cells, and which are characterized by a continuous network of boundaries that separate individual domains. The cellular patterns we will study are caused by surface tension, diffusion and geometrical constraints, not described by reaction-diffusion equations as in biological morphogenesis or Turing patterns. Rather, relaxation dictates the shapes of domains and their evolution, in which energy minimization determines the rates of growth or shrinkage of the domains, and the shapes they assume over time.

Such cellular patterns include foams, metallic grains and crystallites and biological cell aggregates. For each of these classes, different physical processes shape the evolution, but the underlying fundamental constraints are the same:

1. The domains need to fill space.

2. Domains either have fixed volume, or diffusion (annealing, division) determines volume rates of change.

3. In the absence of external influences, energy minimization produces minimal surface cell shapes.

We will use the terms cells, grains and bubbles interchangeably to describe the individual domains within a cellular pattern.

1.4 Cell Shapes

Foams are a cellular patterned material. The most fundamental question that arises quite naturally when looking at say, a honeycomb, or the pattern on the wing of a dragonfly, is why do we see these almost repetitive and ordered patterns? Does a common organizing principle favor the hexagonal symmetries found in such diverse natural patterns as basalt columns and cucumber skin?

The ancient Greeks speculated on the extent of willful execution in the bee's design of the honeycomb [20]. Modern scientific explanations about the origins of naturally ordered patterns emerged in the 19th century. Charles Darwin pointed to natural selection and minimization of metabolic cost as the origin of the efficiency of the honeycomb design [20]. D'Arcy Thompson [47] studied the shapes of cells in a developing geranium and honeycomb. He proposed the mathematics of minimal surfaces and surface tension as the physical explanation for the formation of patterns. Thompson pointed out that Darwin's elaborate explanations were not necessary to explain the elegant solution the bees had found for their storage space problems. He recognized the importance of surface tension and the minimization of surface area as the force behind the hexagonal arrangements of bubble rafts [47]. By likening the

wax in the honeycomb to a sluggish fluid, he was able to explain by purely physical forces the appearance of this highly organized insect made structure.

Frederic T. Lewis [17] studied many analogs in three dimensions, hoping to demonstrate that surface tension was indeed the chief factor in the organization of cellular structures.

1.4.1 Two-Dimensional Cells

Filling space with regular polygons leaves a limited number of choices in two dimensions. A space filling partition can be created using triangular, rectangular or hexagonal regular unit cells. Neither pentagons nor octagons alone can fill space completely.

An argument based on the minimization of the energy associated with cell boundaries illuminates the two-dimensional case:

Simple geometry shows that three-fold vertices with 120° angles require shorter boundary lengths than non-symmetric three-fold vertices, or vertices at which four or more edges join. Figure 1.6 illustrates that a single four-fold vertex requires a larger boundary length per unit area than two three-fold vertices, making the later configuration energetically more favorable.

That the energy associated with edges strongly favors three-fold vertices allows some simple deductions using Euler's theorem:

$$\mathrm{F} - \mathrm{E} + \mathrm{V} = \chi, \tag{1.1}$$

where F is the number of faces (which in two dimensions is the number of cells), E the number of edges, and V the number of vertices. For a simple two-dimensional foam in the Euclidean plane $\chi = 1$. If all vertices in the network possess a coordination number $z = 3$, valence relations hold between the vertices, edges and faces:

1. $V/E = 2/3$, since each edge links two vertices.

2. $\sum_n nF_n = 2E$, where n is the number of edges for each cell F.

Using these valence relations in Euler's theorem (1.1) we find the average number of edges $\langle n \rangle$ in the pattern:

$$\mathrm{F} - \frac{1}{2}\langle \mathrm{n} \rangle \mathrm{F} + \frac{1}{3}\langle \mathrm{n} \rangle \mathrm{F} = 1. \tag{1.2}$$

Thus in the limit of large patterns ($F \to \infty$) the average number of sides per cell is six:

$$\langle n \rangle = 6. \tag{1.3}$$

Symmetric three-fold vertices thus explain the dominance of hexagons in two-dimensional patterns that evolve due to surface tension.

1.4.2 Three-Dimensional Cells

The case becomes more complex in three dimensions. Euler's theorem gains an extra degree of freedom, the number of polyhedral cells C:

$$-\mathrm{C} + \mathrm{F} - \mathrm{E} + \mathrm{V} = \xi, \tag{1.4}$$

where $\xi = 1$ is the topological characteristic of three-dimensional Euclidean space.

In 1873 Joseph Plateau [48] determined rules governing the number of edges that can meet at a single vertex, and the angles at which they meet, for three-dimensional bubbles. In three dimensions the surfaces which bound the cells meet at 120°, creating an edge. Four edges meet at a vertex, with the edges radiating outward from the vertex at equal angles of 109.5° (the tetrahedral angle, $cos^{-1}(-1/3)$) from one another.

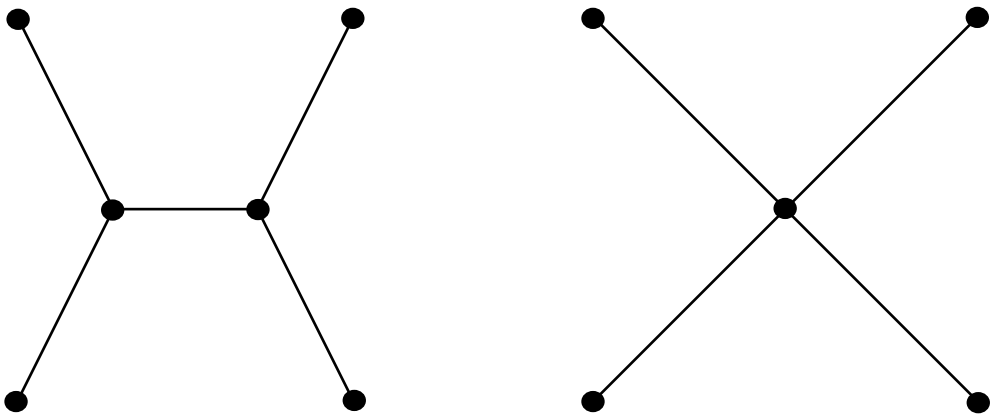

Figure 1.6. Length Minimization. The length of vectors that connect four vertices positioned at the edges of a unit square through a four-fold vertex at the center of the square (90° vertex) is $2 * \sqrt{2} = 2.828$. The same four vertices can connect via two 120° threefold vertices, where the total length of the connecting vectors is 2.732, a 3.5% shorter boundary length.

Similar to the two-dimensional case, Plateau's rules lead to valence relations between the numbers of cells, edges and vertices (e.g. 2V = E, since each edge links two vertices, and four edges meet per vertex), from which we can obtain:

$$\langle \mathrm{f} \rangle = \frac{12}{6 - \langle \mathrm{n} \rangle}, \tag{1.5}$$

This relation requires two parameters, the number of faces and the number of edges per face, to characterize structure in three dimensions.

Plateau's rules mean that no regular space filling polyhedron (such as a simple cube) can fulfill Thompsons minimal surface requirement. In 1887 Lord Kelvin [49] identified a semi regular volume filling cell shape as a candidate for minimizing surface area for an enclosed volume: Figure 1.7 shows the 14-faced tetrakaidecahedron, also known as a truncated octahedron. To satisfy Plateau's rules about adjoining angles, the six-sided faces of Kelvin's tetrakaidecahedron have a small but non-zero surface curvature. A second theoretical candidate was proposed in 1994 by Weaire and Phelan [29]. Their somewhat less elegant solution to the "repeat unit" contains eight cells, two pentagonal dodecahedra, and six 14-faced barrels, with 12 pentagonal and two hexagonal faces, which is shown in Figure 1.8. While all but the hexagonal faces are irregular in this solution, it fills space while obeying Plateau's rules, and has a 0.3% smaller surface area than Lord Kelvin's proposition.

Space filling structures composed of either of the two proposed partitions will have different geometric properties. Kelvin's single 14-sided polyhedron has an exact average number of faces $\langle f \rangle = 14$, and an average number of edges per face $\langle n \rangle = 5.14$. The Weaire-Phelan structure requires fewer faces per domain on average, with $\langle f \rangle = 13.5$, and a slightly lower average number of edges per face $\langle n \rangle = 5.11$.

Edwin Matzke [50, 51] in the 1940's was the first to test Kelvins proposition. An apparently eminently bored botanist, he studied over one thousand bubbles under a

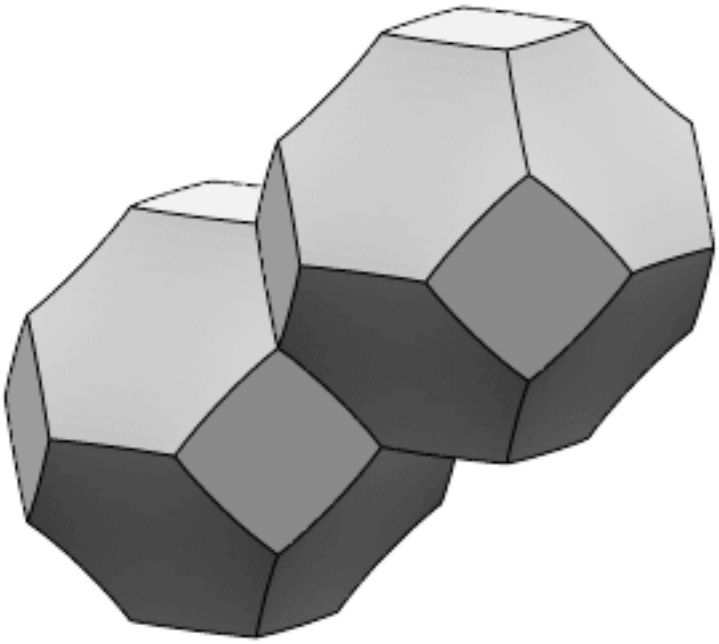

Figure 1.7. Two Semi Regular Kelvin Tetrakaidecahedra. Lord Kelvin proposed the fourteen-sided truncated octahedron in 1887 as the ideal minimal surface candidate for a space filling partition. It consists of six four-sided and eight six-sided faces.

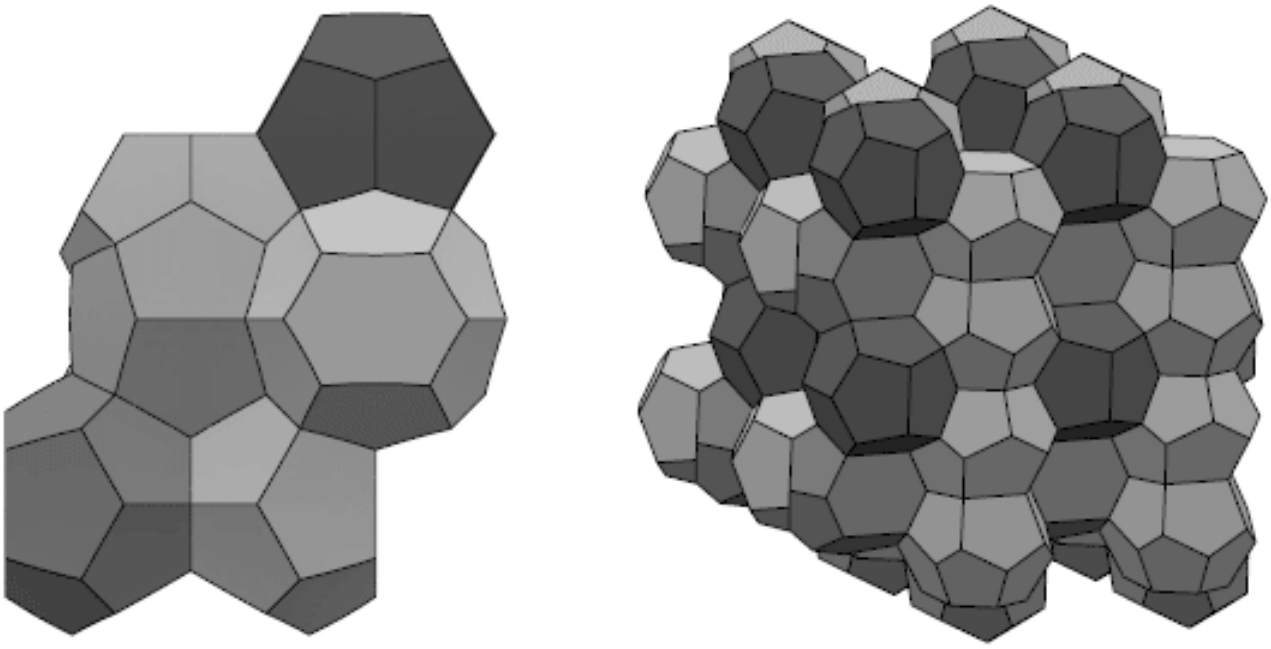

Figure 1.8. The Weaire-Phelan β-Tungsten Partition. Left: Eight cells that make up the partition unit for a minimal surface area partition proposed in 1994 by Weaire and Phelan. Right: A regular arrangement of these cells. Each partition unit contains six fourteen-sided and two twelve-sided cells.

microscope, diligently recording the number and shapes of their faces. While trying carefully to create ordered bubbles - one at a time, he did not observe a single Kelvin tetrakaidecahedron. In fact, his counting found three times as many five-sided faces as six-sided faces, and six times more five-sided than four-sided faces. The average number of faces for all bubbles in his studies was 13.7. Matzke did not record the relative position of bubbles with respect to one another, so he would not have noticed a repeat unit existing of more than one irregular polyhedron.

More recently, Kose [52] (using rigid foams) and Monnereau [53] have found similar results, with $\langle f \rangle = 13.6$ and $\langle f \rangle = 13.4$, respectively. They also found structures dominated by five-sided faces.

Weaire and Phelan have found ordered structures resembling their proposed minimal space filling partition in carefully prepared stacks of bubbles in narrow columns [28]. However, not a single unit cell consisting of all eight irregular cells has been identified, much less a repetitive pattern. Rivier also points out that the Weaire-Phelan solution is unlikely to be the best solution to a minimal surface repeat unit, pointing to an array of metallic phases which serve as other candidates [54].

While experimental results cannot refute the validity of the minimal area propositions, they can support the physical assumption that, indeed, foams tend to minimize surface area when given time to evolve, if such structures were to be found. Since real 3-d foams always start out far from equilibrium, it is important to study the same bubbles over long periods of time to see if ordered structures emerge. It is intriguing to note the relative ease with which natural patters assume ideal shapes in a two-dimensional perspective (while not actually being two dimensional), while we seem to have such a hard time finding the mathematically idealized shapes we predict in three dimensions.

1.5 Grain Growth

1.5.1 Background

The study of metals provided the incentive for the modern scientific investigation of grain growth. The growth and annealing of crystallites in metals is of great importance to metallurgy. In 1952 Smith recognized the analogy between growth in bubbles and crystallites, and proposed foams as a prototypical model for the study of grain growth [15]. While many cellular structures, such as fracture patterns observed in basalt and across the frozen surface of the moon Europa, appear fixed in time, many evolve at their own glacial pace, driven by repeated freeze-thaw cycles or tectonics. Biological cells divide and grow into carefully arranged patterns.

Grain growth requires time evolution, and an energy associated with the boundaries. More complex requirements, such as size, functionality, outside stresses influence cracking patterns and biological cell arrangements.

The domain growth we investigate applies to cellular patterns that evolve due to diffusion and surface energy minimization.

1.5.2 Grain Growth Laws

John von Neumann related the area rate of change of a two-dimensional grain to the grain's number of sides [55]:

$$\frac{\mathrm{da_n}}{\mathrm{dt}} = \kappa(\mathrm{n} - 6), \tag{1.6}$$

where $\mathrm{a_n}$ is the area of a cell with n sides, and κ is a diffusion coefficient depending on the surface tension and diffusion constant across the boundary. Equation 1.6 is exact if the diffusion rate is linearly proportional to the pressure difference across a boundary (in the case of foams), or for which the local boundary velocity is proportional to local curvature (as may be the case in metallic grains) [9, 19].

Despite the success of von Neumann's law in describing the time evolution of two-dimensional grains, a three-dimensional equivalent based on similarly simple assumptions has not been found. Recent simulations have led to a better theoretical understanding of three-dimensional growth and the scaling properties of grains [38, 39, 40, 42].

Analogous to von Neumann's law for two-dimensional grain growth [55], based on computer simulations, Glazier proposed an averaged growth law for three-dimensional grains [38]:

$$\langle \mathrm{V}_f \rangle^{-1/3} \langle \frac{\mathrm{dV}_f}{\mathrm{dt}} \rangle = k(f - f_0). \tag{1.7}$$

The averaged volume rate of change for a group of bubbles with f sides depends only on its number of sides. On average, bubbles with f greater than f_0 will grow, while bubbles with a smaller number of faces will shrink. k is a diffusion constant. For the relation between f and f_0 , Weaire and Glazier deduced that [39]:

$$f_0 = \langle f \rangle \left(1 + \frac{\mu_2}{\langle f \rangle^2} \right), \tag{1.8}$$

where $\mu_2 = \langle f^2 \rangle - \langle f \rangle^2$ measures the disorder of the foam. Eqn. 1.8 is exact provided that the average volume of a bubble with f faces scales as $\langle V_f \rangle \propto f^3$, which was true in Glazier's Potts model simulations.

Sire [40] used the form of Glazier's proposed relation 1.7 and a set of topological assumptions to derive a generalized expression for three-dimensional grain growth from the Young-Laplace law:

$$\mathrm{V}_f^{-1/3} \frac{\mathrm{dV}_f}{\mathrm{dt}} = \mathcal{F}(f), \tag{1.9}$$

where $\mathcal{F}$ is an increasing, almost linear function of f only.

Most experimental studies have concentrated on two-dimensional domain growth, including bubble rafts, magnetic domains and lipid mono-layers, which are easy to create and observe [56, 57, 58, 59]. The results have verified von Neumann's assertion in a wide range of materials, to the extent that an averaged form of his law is found to hold. Glazier proposed the same for three-dimensional grains. Durian [43, 44, 45] and Monnereau [41, 53] have independently studied grain growth in three dimensions using Diffusing Wave Spectroscopy and Confocal Optical Tomography, but the results could not verify Glazier's proposed law directly.

Durian *et al.* used diffusing wave spectroscopy (DWS) to measure the rates of rearrangement and the averaged grain volume growth exponents in bulk shaving cream, [43, 44, 45]. They found that the average radius grew according to a power law $\langle r \rangle \propto t^{\beta}$, with $\beta = 0.5$, consistent with "self-similar" growth, in which the normalized distribution of bubble volumes does not change over time. DWS can examine very large numbers of bubbles (hundreds or thousands) over many decades of growth in length scale. But while it can measure the mean free path, and hence averaged bubble diameters, DWS cannot provide direct information on bubble size distributions, or grain shapes and topologies which are needed to verify growth laws.

Confocal optical tomography can determine the growth and shapes of individual bubbles in dry foams [41, 53], but only for foams with few interior bubbles (Monnereau *et al.* studied a total of 28). COT is anisotropic with limited spatial resolution, and requires black film boundaries, which restricts it to extremely dry foams in which the volume of the liquid phase is negligible.

The most careful study of three dimensional bubble shapes was done by the botanist Matzke (see previous section on structure) [50, 51], using a simple binocular microscope and near endless patience. He studied 1900 individual bubbles, noting their numbers of faces and edges. While providing valuable data on the shapes of

such grains, he could not provide information on volumes and locations, lacking the ability to determine exact vertex locations, or to track a bubble's evolution over time.

The following discussion will introduce MRI as a method to investigate the shapes and sizes of three-dimensional bubbles. Previous work that has looked at the shapes of bubbles, was always limited to investigating bubbles near surfaces, and either very small or very dry samples. No one has performed studies over long periods of coarsening. We will study samples of liquid foam over long periods of time, allowing us to observe individual bubbles as they coarsen.

The information obtained from tracking individual bubbles, and recording the number of faces f and volume V(t) for those that do not change number of sides between data runs allows us to investigate Glazier's growth law 1.7 directly. The integral at constant topology between t_0 and t of Equation. 1.7 yields for the volume rate of change:

$$\frac{\mathrm{dV}_f^{2/3}}{\mathrm{dt}} = \kappa(f - f_0), \tag{1.10}$$

where $\kappa = 2/3k$.

Verifying the form of Glazier's growth relation would be an important step in establishing a three-dimensional growth theory based on grain topology.

CHAPTER 2

MAGNETIC RESONANCE MICROSCOPY

2.1 Background

2.1.1 From NMR Spectroscopy to NMR Imaging

Nuclear magnetic resonance is the accepted name describing the stimulated absorption and emission of energy from nuclei that are polarized inside a magnetic field. Bloch and Purcell shared the 1952 Nobel price in physics for their independent 1946 discoveries of this phenomenon [60, 61]. Today NMR spectroscopy is widely used to study the structure and dynamics of molecules and to predict a molecule's usefulness as a chemical reactant or metabolic agent.

This thesis will not review in detail the classical or quantum mechanical descriptions of NMR principles and methods. A well established body of literature exists, and the interested reader is advised to peruse the original work done by Purcell [60] and Bloch [61, 62, 63], the first published review of the NMR phenomenon by Bloembergen and Purcell in 1948 [64], as well as the discovery of spin echoes and the development of complex pulse sequences described by Hahn [65] and Carr and Purcell [66]. Fergusen published a concise review of NMR and its history was published in 1967 in *Science* [67]. Since then the development of specialized applications and the breadth of highly specialized research in NMR, has relegated introductory writing about NMR to the realm of increasingly specialized textbooks.

Standard contemporary texts on NMR include a quantum mechanical description by Goldman [68], and a general NMR review by Fukushima and Roeder [69].

Academic Press publishes regularly a series of reviews of the state of the art in NMR under the title *Advances in Magnetic Resonance* [70, 71].

Lauterbur first described the possibility of using magnetic field gradients to localize the stimulated signal emission during regular NMR spectroscopy in a groundbreaking article in *Nature* [72] in 1973. Mansfield and Morris developed fundamental concepts of localized spectroscopy, such as the reciprocal-space representation that same year [73]. While Lauterbur proposed the name "Zeugmatography" (from the Greek word $\zeta\varepsilon\upsilon\gamma\mu\alpha$, "that which is used for joining"), and early texts referred to NMR imaging, the accepted name since the mid 1980's has been Magnetic Resonance Imaging, or simply MRI. Section 2.2 will give a brief summary of concepts underlying localized spectroscopy, MRI, while section 2.3 will discuss the specific application of MRI to imaging of foams. For a more thorough treatment of general MRI principles, Elster [74], NessAiver [75] and Woodward and Orrison [76] have published excellent texts, which are easily understandable by the non-expert reader.

2.1.2 Medical MRI

MRI has evolved into a common and irreplaceable tool for diagnostic medicine. It is ideal for studying biological tissues, muscle, brain and organs, which contain a high natural abundance of excitable water and that are transparent to x-rays. It is used in the early diagnosis of tumors, lesions and other organic abnormalities. Special MR scanners aid surgeons during surgery, while drug research relies on MRI to study the effectiveness of experimental drugs. Research is under way to monitor organ transplant rejection, abnormal brain activity and heart conditions [77]. The complexity of research has led to the establishment of several regularly published journals devoted to developments in MRI. Once basic principles of NMR are understood from reading introductory texts (see section 2.1.1), the best way to learn

about medical MRI is to study introductory textbooks into the very diverse sub categories of MRI.

A standard text covering biomedical applications of MRI is the first thorough and concise overview written by Mansfield and Morris [78] in 1981. Updated collections of reviews have been published by Chien and Ho in 1986 [79], Wehrli in 1988 [80], and Certaines [81] in 1992. As in NMR spectroscopy, books on specialized MRI methods now appear on a regular basis. One recent publication by Prince, Grist and Debatin [77] on functional three-dimensional imaging of the heart (MR Angiography) can serve to illustrate the current complexity of the subject, as well as the direction in which biomedical MRI is heading.

2.1.3 Non-Medical MRI

Diagnostic MRI facilities are available at most medium and large sized medical facilities throughout the developed world. These imagers typically employ magnetic fields between 0.02 Tesla ("ultra low field scanners") and 1.5 Tesla ("high field scanners") with many levels of hardware sophistication available [74]. Spatial resolutions are on the order of $1mm^3$, and most scanning techniques employ slice-selective imaging, in which quasi two-dimensional slices are selected one at a time, using typical magnetic gradient strengths of 5-10 Gauss/cm (0.05 - 01 mT/m).

In contrast, non-medical MRI has developed comparatively slowly. First non-biological applications in the late 1980s led to the newly emerging interest by material scientists, chemists and physicists in complex physical structures and dynamics, that could not be investigated before the arrival of sophisticated MRI scanners [82]. The development of reliable high field gradients, fast digital acquisition, high powered rf-amplifiers and resonators, and of new, specialized imaging techniques have allowed researchers to investigate non-biological subject matter over

the last decade [82, 83, 1, 84]. Imaging is possible at resolutions of a few microns using gradients up to a hundred times stronger than those found in medical scanners, while fields up to 14 Tesla (600 MHz proton resonance) allow relatively high polarization densities. Complex excitation and signal extraction techniques can image samples with few free protons (or other polarizable nuclei) [84].

NMR-microscopy applications range from food and agricultural sciences (disease, spoilage, baking), to chemical engineering (fluid dynamics, turbulence, multi-phase flow, material microstructure), to chemistry (diffusion of solvents and gases, reaction anisotropy, curing, polymerizations), to material science and physics (physical defects in ceramics, crystals, polymeric materials, stress, wear and aging) [1].

Winfried Kuhn published the first review on the technical fundamentals, as well as the possibilities and limitations of this new field of MRI research in 1990 [82]. Komoroski published a broad based review on a large variety of applications of non-medical MRI in 1993 [1]. While many publications in many areas of NMR/MRI prevent singling out one authoritative text, Paul Callaghan's 1991 book *Principles of Nuclear Magnetic Resonance Microscopy* [83] is a standard reference used in non-medical NMR microscopy.

2.2 Principles of MRI

I will briefly review the fundamental principles and terminology used in MRI. Understanding these concepts is necessary to the discussion of applying MRI to foams, and the detailed description of the experimental setup and procedures in Chapter 3.

2.2.1 Basic Nuclear Magnetic Resonance

The most basic relationship in NMR is given by the Larmor Equation (2.1), which describes the resonance condition for polarizable nuclei inside a magnetic field:

$$\omega = \gamma \mathbf{B}, \tag{2.1}$$

where ω is the frequency of precession of the nucleus inside a magnetic field $\mathbf{B}$ and γ is the gyromagnetic ratio of the nucleus. Protons are used for almost all imaging purposes, because of their high abundance in a large variety of materials (usually as water), and their large gyromagnetic ratio of 42.8 MHz/Tesla.

The protons can be excited by an rf-pulse which matches their precession frequency ω. In this process the protons also acquire phase coherence. The amount of maximum excitation under normal conditions and at room temperature is proportional to the strength of the applied magnetic field $\mathbf{B}$, and is on the order of a few parts per million. At maximum excitation the combined magnetic moment vector of the protons (*net magnetization*) precesses entirely in the plane perpendicular to the applied magnetic field. This resonance condition is called *transverse magnetization*, immediately after application of a *90° pulse*.

The protons start to lose both their phase coherence and excitation immediately after the rf-pulse is applied. The emission of rf energy from the protons as they de-excite is picked up by suitable receiver circuits, and constitutes the principle signal in NMR spectroscopy called *free induction decay*, or **FID**.

2.2.2 Relaxation Times

This FID signal is originally equal to the net transverse magnetization of the sample $\mathcal{M}_0$. In the standard reference frame inside the bore of a magnet, the $\hat{z}$ direction is the direction of the primary magnetic field vector $\mathbf{B}$, while the $\hat{x}\hat{y}$-plane lies perpendicular to it. The time dependent magnetization vectors within the $\hat{x}\hat{y}$-plane, and the projection along the $\hat{z}$-axis can be described in terms of two characteristic time constants:

$$\mathcal{M}_z(t) = \mathcal{M}_0(1 - e^{-t/T_1}) \tag{2.2}$$

and

$$\mathcal{M}_{xy}(t) = \mathcal{M}_0 e^{-t/T_2}. \tag{2.3}$$

The equations are named after Felix Bloch, who first derived them in 1946 [62]. Equation (2.2) describes the loss of excitation in the sample, and the time it takes for the net magnetization to return to the longitudinal $\hat{z}$ direction. **T1** is called the *longitudinal relaxation time*, or *spin-lattice relaxation time*, as it is due to interactions of individual nuclei with the lattice environment [68]. Equation (2.3) describes the loss of phase coherence within the xy-plane, which leads to a vanishing of the transverse magnetization, typically much faster than longitudinal relaxation. **T2** is called the *transverse relaxation time*, or *spin-spin relaxation time*, and is due to the magnetic interactions of excited nuclei with their direct spin neighbors, which causes small phase shifts [68]. Both T1 and T2 are characteristic time constants for a given sample and need to be measured to ensure optimal resonance conditions. Differences in relaxation times can provide additional contrast in NMR images that contain regions with different time constants.

Due to these interaction phenomena, the FID is a dampened oscillating wave, which carries frequency components representing the exact Larmor frequencies of all nuclei excited by the rf-pulse. For a given **B** field, the amplitudes of the frequency components are proportional to the abundance of the nuclei. In the case of an ideally homogeneous **B** field, a pure water sample would emit an FID with a single frequency component as shown in Figure 2.1A, representing the Larmor frequency of the hydrogen bound only to oxygen in the water molecules. The time varying NMR signal $s(t)$ can be written as a Fourier series:

$$s(t) = a_0 + a_1 sin(\omega_1 t + \phi_1) + a_2 sin(\omega_2 t + \phi_2) + ... \tag{2.4}$$

A discrete inverse Fourier transform can extract the frequency components from the signal. These frequency domain data represent the NMR spectrum of a given sample, shown in Figure 2.1B. High resolution spectra contain detailed information about the chemical composition and even molecular structure inside the sample. Details on NMR-spectroscopy can be found in [68, 74, 75] and many other texts.

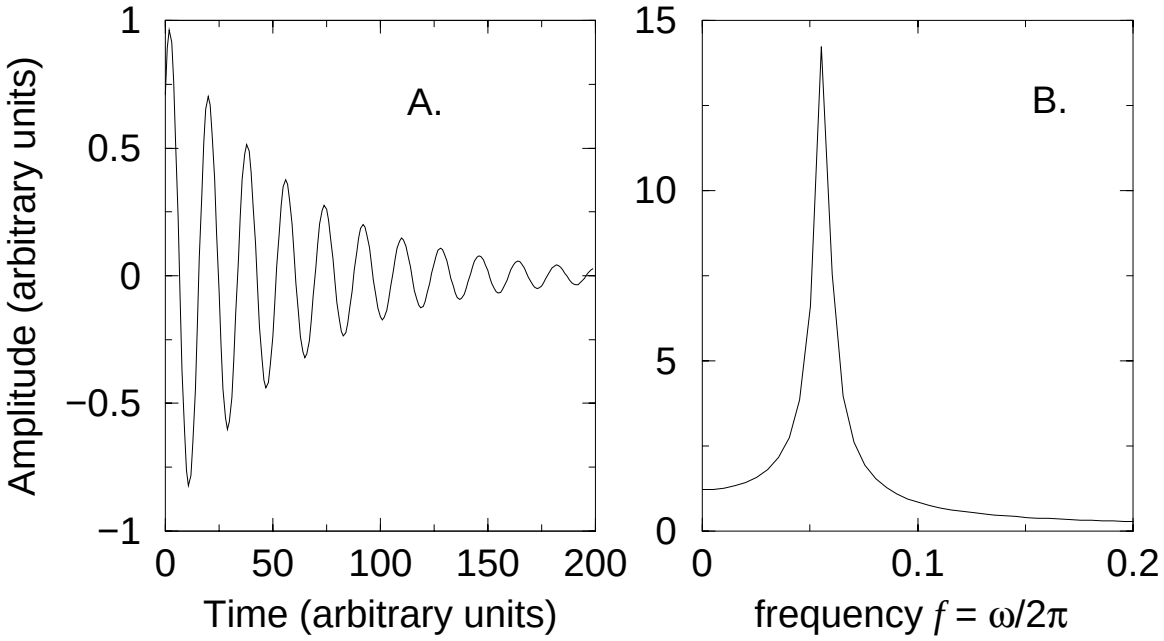

Figure 2.1. A) Time Varying Oscillating Signal: The "Free Induction Decay", or FID, is emitted by the relaxation of excited nuclei. B) shows the inverse Fourier transform of the signal, with one single frequency component.

2.2.3 Spin Echoes

Spin echoes are a phenomenon discovered very early in the evolution of NMR by Hahn [65], and developed into a standard spectroscopic technique by Carr and

Purcell [66]. Due to hardware constraints, measuring the FID from the very moment when it is strongest, which is ideally at the exact end of the rf-pulse application, is physically impossible. The delay in measuring the FID means that the strongest part of the signal is not recorded.

Hahn [65] showed that while a 90° pulse transfers the net magnetization into the xy-plane, two consecutive 90° pulses, or one 180° pulse after that, should first "invert" the direction of the magnetization into the $\hat{z}$ direction, and then back into the $\hat{x}\hat{y}$-plane, only 180° out of phase from before. The effect of this shift is that spins that were dephased by a positive phase shift of $\Delta\phi$ in the time TE/2 between the application of the 90° pulse and the 180° pulse, now have a phase shift of $-\Delta\phi$ immediately following the 180° pulse. After evolving another time step TE/2 the phase shift of these spins will be $-\Delta\phi + \Delta\phi = 0$ again, hence the original transverse magnetization is fully restored and can be measured. This restoration is called a *spin echo*, or **SE**. The characteristic time at which it occurs is the *echo time*, or TE. Acquisition techniques using spin echoes are common today, both in NMR and MRI.

2.2.4 Spatial Encoding: Basic Image Acquisition

MRI is concerned with obtaining spatial information from the resonance signal of a sample. Equation (2.1) states that the frequency that is both absorbed and emitted during the excitation and relaxation of a nucleus is proportional to the local magnetic field **B**. Stimulated excitation by means of an rf-pulse also leaves the excited nuclei in initial phase coherence.

While there are different techniques of spatial encoding, the most widely used techniques involve successive applications of three magnetic field gradients, along fixed orthogonal principal axes. Depending on hardware and software capabilities,

these axes can be at oblique angles with respect to **B** inside the magnet and need not be fixed along the principal $\hat{x}$,$\hat{y}$ and $\hat{z}$ axes.

A slice selective two-dimensional Spin-Echo (SE) pulse sequence provides the most basic two-dimensional snapshot of a region, or *slice*, in a sample. Figure 2.3 diagramms the detailed pulse program sequence in standard form. Figure (2.2) shows a schematic of the applied gradients. A 90° and a 180° pulse are used to obtain a spin echo, while a set of gradients encodes the spatial dimensions:

1. During the application of a 90° rf-pulse with a well defined frequency bandwidth, the magnetic field gradient changes the Larmor frequencies of the protons in the sample along one axis. Due to the Larmor relation (2.1) only protons with a Larmor frequency within the rf-pulse bandwidth experience excitation and phase coherence. This step is called *slice selection*. The thickness of the slice is proportional to the rf-pulse bandwidth, and inversely proportional to the applied gradient strength.

2. Immediately following the slice selective rf-excitation, a gradient is applied along the (arbitrary) $\hat{x}$-axis within the image plane. This gradient is the first of two applications of a *frequency encoding gradient*, effectively dephasing the spins in a defined manner in a column along the $\hat{x}$-axis.

3. Perpendicular to the frequency encoding gradient, along the y-axis, a third *phase encoding gradient* is applied, dephasing the spins along the $\hat{y}$-axis by a known, fixed amount.

4. At time TE/2 a 180° pulse is applied.

5. At time TE the magnetization vector rephases and the FID signal is acquired. At this time the frequency encoding gradient is turned back on, now also

called the *readout gradient*, giving spins along the $\hat{x}$-axis different resonance frequencies, while maintaining phase coherence for a short time.

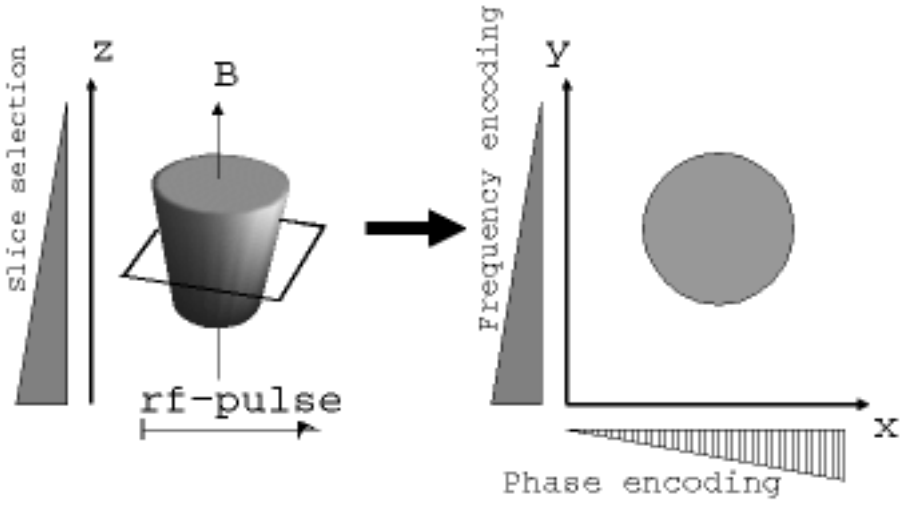

Figure 2.2. Schematic of the Applied Gradients: An applied rf-pulse selects a single slice along $\hat{z}$. The consecutive applications of a phase encode gradient along $\hat{x}$, and a frequency encode gradient along $\hat{y}$ during signal readout encode the remaining two directions.

Repeating steps 1 - 5 N times produces an image with N x N distinct frequency and phase components, resulting in an image with N x N pixels. During the repeats, which are separated by a characteristic time period **TR**, the *repetition time*, the strength of the phase encoding gradient (step 3) is changed, providing N separate FID's, each containing the same frequency components, but different phase information for each repetition. As the phase change for each of the N elements along the phase encode axis can be calculated from the strength of the gradients, each of the N x N elements corresponds to a unique phase and frequency.

Finally, two consecutive discrete Fourier transforms extract first the phases and then the frequency components in each FID and map them to spatial coordinates, as

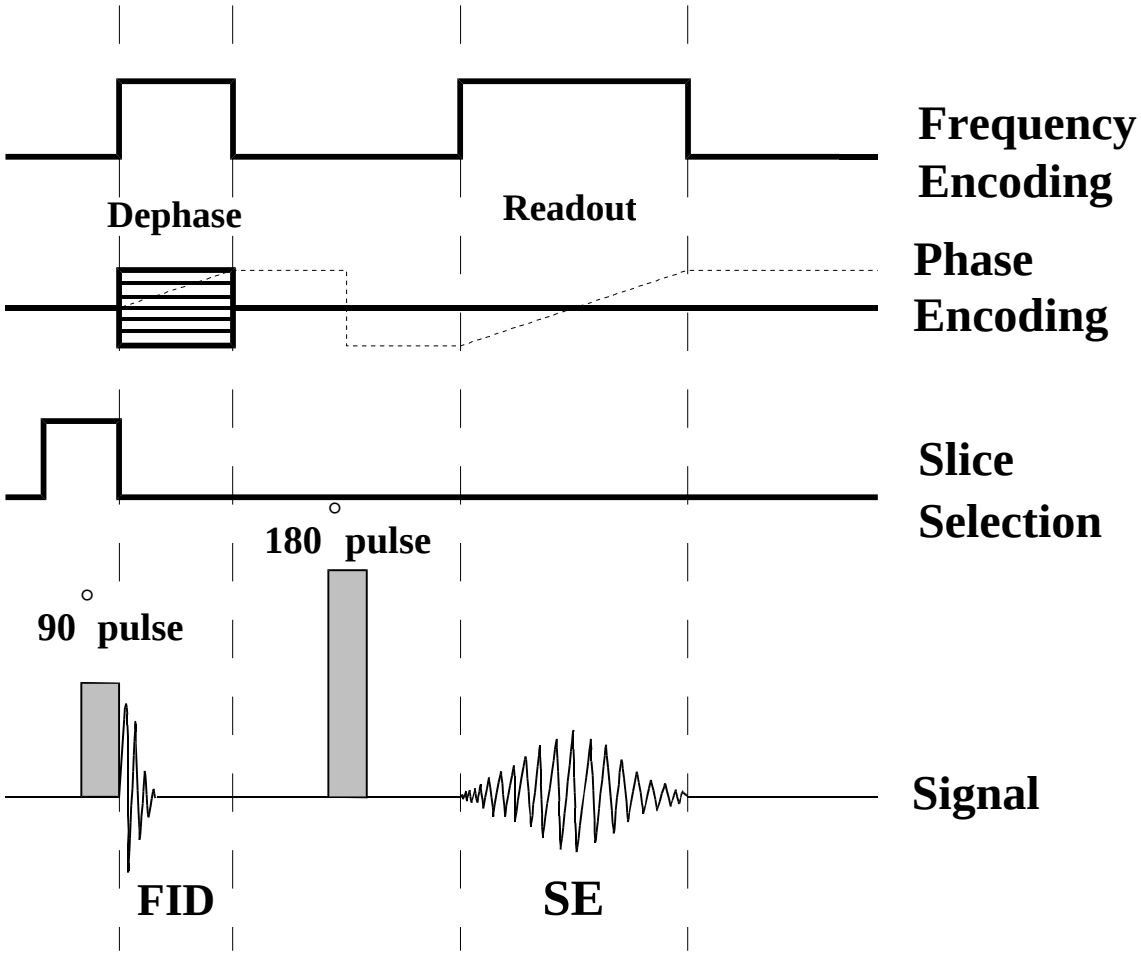

Figure 2.3. Pulse Program for a Basic Two-Dimensional Spin-Echo Pulse Sequence. A 90° rf-pulse selects a slice. Immediately after both frequency and phase are encoded during signal dephasing. A 180° pulse begins to rephase the signal at time $t = TE/2$. At time TE the "spin echo" (SE) rephases. Frequency and phase gradients are applied again during this readout phase.

shown in Figure 2.4. The amplitude of each component is proportional to the intensity value assigned to the corresponding pixel. This technique is called a *magnitude reconstruction* of a two-dimensional image. This basic technique yields a single slice of finite thickness through a sample. An extension is to use several slice selections during a single repetition. Steps 1 - 5 can easily be repeated for slightly different frequency ranges in the rf-pulses, selecting different slices each time. This is especially convenient, since TR typically needs to be on the order of several hundred milliseconds or more, due to spin-lattice relaxation times (T1) which are often of that magnitude. This way 8, 16, 32 or more individual slices can be imaged in the same time it takes to acquire a single slice. The limiting factors here are the ratio of TR/TE (where TE is somewhat determined by T2), and the duty cycle of the gradients and rf amplifiers.

2.2.5 Pulse Shapes

Two-dimensional image acquisitions rely as a first step on the simultaneous application of a slice selection gradient and an rf-pulse. For the slice selection to work properly, the frequency spectrum of the rf-pulse must be well defined. The shape and bandwidth of the applied rf-pulse are the most important contributing factor determining the exact localization and homogeneity of the spin excitation.

An ideal slice-selective rf-waveform would produce a rectangular frequency spectrum S(ω) under an inverse Fourier transformation. Rf-pulses are often shaped like modified *sinc* functions, where:

$$sinc(x) = \frac{sin(\pi x)}{\pi x}. \tag{2.5}$$

Figure 2.5 shows two standard NMR *sinc* pulse shape envelopes and their respective frequency spectra. The pulse shapes were generated using the Bruker XWIN-

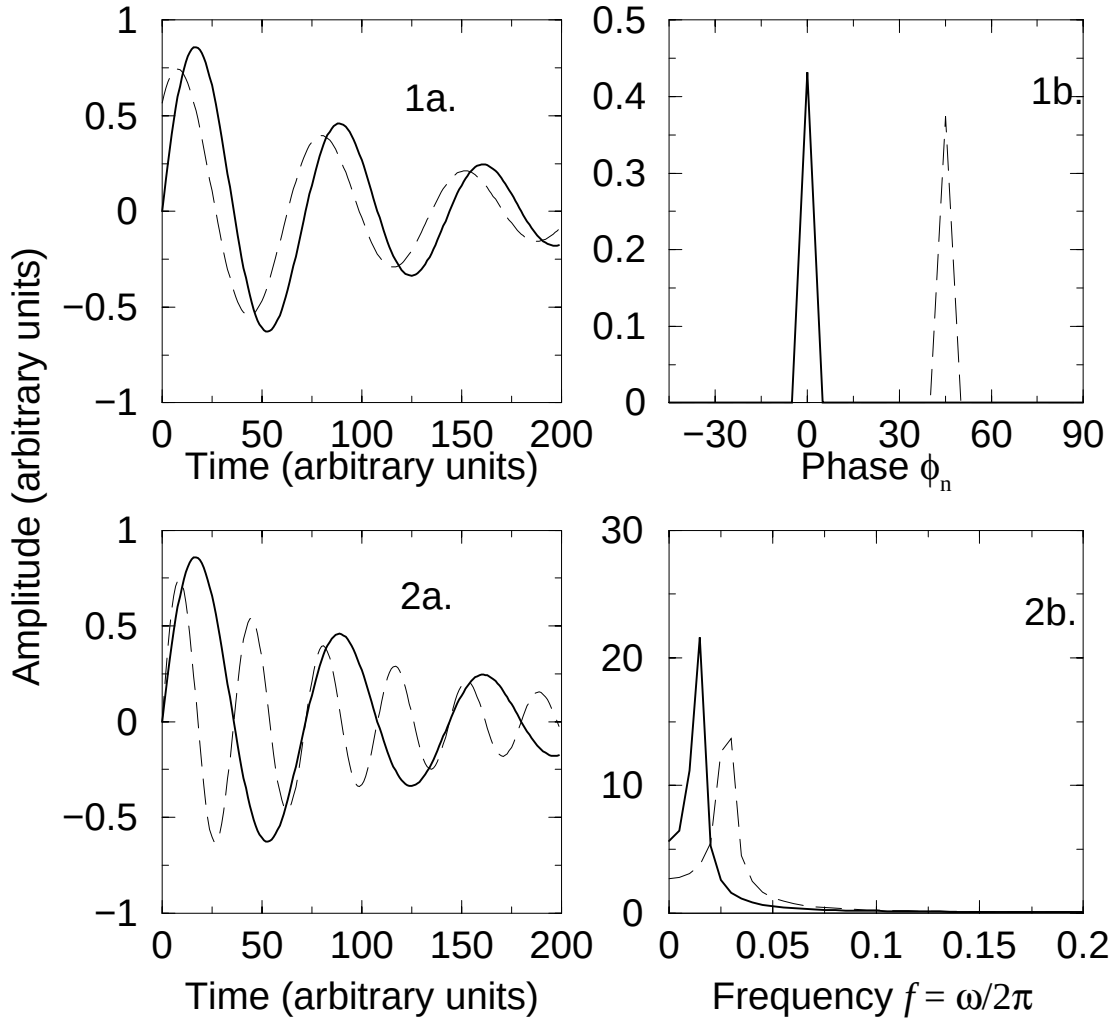

Figure 2.4. Frequency and Phase Encoding and Their Fourier Transform: 1a) and 1b) show time and frequency domain representations of two sinusoidal waveforms with identical frequencies but 45° out of phase. 2a) and 2b) show the same representation for two waveforms with identical phases but different frequencies. The frequency domain representation can assign to each frequency and phase component a corresponding location in space and an intensity.

NMR standard pulse shape library and recorded on a Tektronix 400 MHz digital storage oscilloscope. The pulse shape library defines the envelope for a selected rf-waveform. The rf-amplifier generates the exact specified amplitude at the selected "basic frequency" (the resonance frequency to which the imager was tuned). Both pulses shown had 100μs duration. The excited frequency range is inversely proportional to the width of the side lobes, while the homogeneity of the excitation increases with the number of lobes [74]. The sketches on the left show an approximation of their frequency spectra. The *sinc5* pulse (one main lobe and four side lobes) excites a frequency range of 100000 Hz fairly homogeneously. The *sinc2* pulse excites a much narrower frequency range (40kHz) and is much less homogeneous across the spectrum. The quality of the slice selection will therefore depend on the quality of the *sinc* pulse envelope produced by the NMR imager, and the basic frequency of the signal. All other factors being equal, the selection of thin slices (narrow frequency ranges) will result in less homogeneous excitation within the slice than will a thicker slice. Ideal rectangular Fourier spectra would require an infinite number of lobes (and hence infinitely high frequencies). Typical slice selective applications in biomedical imaging require bandwidths of no more than 500 Hz to 10000 Hz, resulting in typical medical slice thicknesses of 500μm to 1500μm, depending on the basic frequency and gradient strength. *Sinc3* pulses usually suffice for such applications.

A very different technique of imaging, volumetric imaging (discussed in Section 2.4: Imaging of Volumes), sometimes relies on so called *broadband pulses* (which is why some three-dimensional imaging is also referred to as *hard-pulse* imaging). A single rectangular pulse envelope is generated by the pulse program, typically with very short duration, on the order of 5μs to 50μs. The bandwidth of the rf-pulse is inversely related to the duration of the pulse and is of order t_p^{-1} [83]. The

homogeneity of the excited bandwidth is determined by the time it requires for the amplifier to reach the maximum desired power output, or by the width of a single half-cycle of the rf base frequency (whichever takes longer). Generally the homogeneity is better throughout the excited volume than during *sinc* pulse based slice selective imaging. Bandwidths of such non-selective pulses are in excess of 20 kHz and may be as high as 200 kHz, which is sufficient to excite all nuclei of a given spin species (with the exception of some solids).

2.2.6 Detection Bandwidth and Aliasing

When sampling a continuous wave-form for computers, the signal must be digitized and represented in a finite space of data points. In NMR and MRI N data points are sampled at intervals t_s. This discretization limits the frequencies which can be distinguished. Wave-forms with periods less than $2t_s$ will appear to oscillate with a period longer than $2t_s$, so that the maximum frequency that can be measured is $f_{max} = 1/2t_s$. A spectral component with frequency $1/2t_s + \delta$ will appear at $1/2t_s - \delta$. This effect is known as *aliasing*. It limits the frequency components we can detect to between $\pm 1/2t_s$, so that the *detection bandwidth* is the inverse of the sampling interval, namely $1/t_s$.

An important consequence of this bandwidth limitation is that we need to prevent unwanted aliasing of signals outside the desired observation bandwidth. A standard solution is to employ digital bandpass filters, which, in an ideal experiment, should have the identical bandwidth to the detection signal. We will discuss aliasing and its effects during foam imaging experiments and analysis in Chapters 3 and 4.

A. SINC2-PULSE

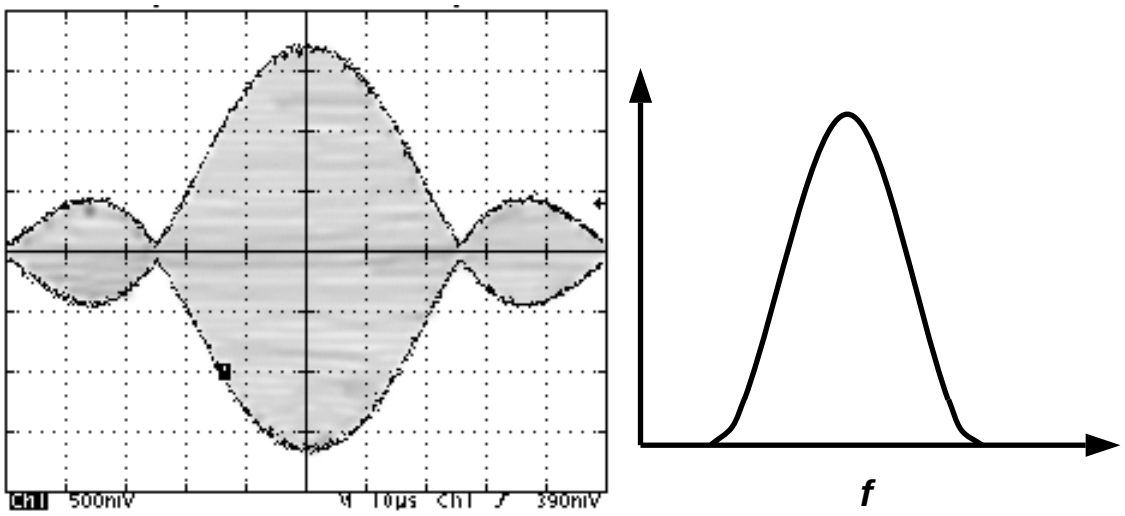

B. SINC5-PULSE

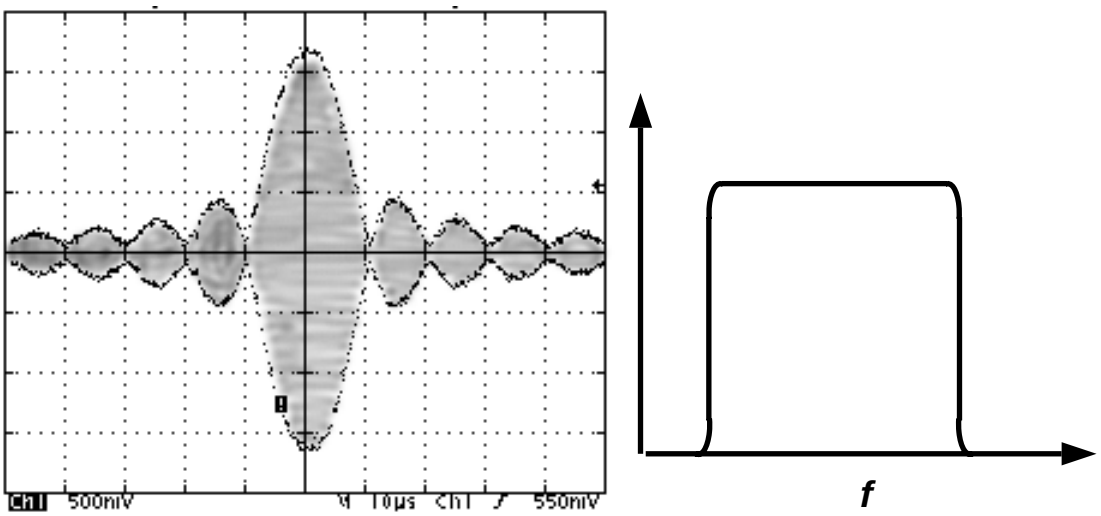

Figure 2.5. Rf-Pulse Shapes and Their Frequency Spectra (Pulse shape images courtesy of Dr. I. Veretennikov).

2.2.7 Contrast

Spin-echo pulse sequences can be adjusted to enhance specific tissues such as lesions and tumors, which contain more water than healthy tissue, and which are more penetrable to contrast agents that alter their T1 and T2 relaxation properties. Figure 2.6 illustrates the dramatic effect of relaxation time differences on images, and how they can be exploited for contrast. The sample imaged is a standard phantom, which reveals geometric distortions, as well as allowing calibration of time constants and sequence parameters. One circular region in Figure 2.6 contains liquid with reduced T1 and T2 compared to the rest of the sample, resulting in varying contrast, depending on the selection of TE and TR in the imaging sequence.

The first eight images are from a sequence with increasing echo times TE. The shorter T2 in the circular region means that as TE gets longer, fewer spins can be rephased and the signal becomes weaker compared to the rest of the sample. The contrast provided by choosing a long echo time TE is called T2 *weighted*.

The two bottom rows show the effect of T1 relaxation, which can be exploited by changing the repetition time TR, the rate at which FIDs are acquired. The time between consecutive rf-pulses needs to be long enough for the sample to relax to its ground state through spin-lattice (longitudinal) interactions. The weaker the spin-lattice interaction, the longer T1. By repeating an rf-pulse before parts of the sample are fully relaxed, we can catch it in a partially saturated state, in which the signal returned from each 90° pulse diminishes. The bottom eight images in Figure 2.6 show a sequence of increasing TR, called T1 *weighting* (short TE, short TR). While the short T1 of the small circular region relaxes fast enough to provide good signal even at very short TR, the rest of the phantom shows increasing signal intensity as TR becomes longer. Each image is individually rescaled to 256 gray levels, which is why the signal in the small circular region appears to be decreasing

in the last few images. It does not. The rest of the phantom's signal becomes stronger, but the images are all scaled to the same value. This phenomenon can lead to misinterpretation of MRI images, particularly in medicine, where determinations of tissue types are often made based on relative contrast! The last image might in isolation suggest an extremely long T1 for the circular region.

The last few images are *proton density weighted* (short TE, long TR). The regions have slightly different polarizable proton densities that are solely responsible for the contrast.

Figure 2.6. Series of Images of an Imaging "Phantom": The phantom contains regions with different T1 and T2 relaxation times. Adjusting imaging parameters changes the contrast between the regions.

2.2.8 Imaging Techniques

The previous discussion has focused on a basic two-dimensional imaging technique, the two-dimensional spin echo experiment, which teaches the most important fundamental concepts of magnetic resonance imaging. In its most basic form it enables researchers to obtain a single slice of finite thickness, a cross-section at an arbitrary location through a sample. An extension of this basic technique can image several slices during a single acquisition, and, if relaxation times permit, establish a quasi three-dimensional image by layering the separate slices back together.

For most subjects, repetition times TR are much greater than the echo time TE, reflecting the common combination of long T1 and short T2. After acquiring an echo, and before a new repetition begins, the MRI imager is essentially idle. Hence, the entire process of slice selection, frequency and phase encoding can repeat several times during this "dead time", each time for a slightly different resonance frequency.

The ratio of TR/TE in the pulse sequence (where T2 somewhat determines TE), and the duty cycle of the gradients and rf amplifiers determine the number of slices that can be acquired this way, typically eight or more slices.

Acquiring many slices this way results in a quasi three-dimensional image. The drawback of multislice imaging is that the excitation strength within each slice is not entirely homogeneous along $\hat{z}$, and that a small interslice spacing must separate slices to prevent signal overlap [74]. Thus we cannot achieve true isotropic resolutions (where the linear resolution along each imaging axis is the same).

Another drawback of SE techniques is the long repetition time TR. After flipping the magnetization vector by 90°, biological tissues take from several hundred microseconds up to a few seconds, to revert to full longitudinal magnetization (at typical medical field strengths). TR then needs to be at least that long to obtain transverse magnetization during consecutive excitations.

Gradient Echo (GRE) techniques allow faster imaging [76, 74, 78]. GRE allows very short TE and TR by flipping the longitudinal magnetization by only a few degrees with each repetition. A gradient reversal instead of a second rf-pulse refocusses the spins. Like SE, GRE allows multislice acquisitions with the same restrictions. While GRE is considerably faster, it suffers from much lower signal strength and is more sensitive to susceptibility and chemical shift artifacts [74](Section 2.3 discusses artifacts in more detail). GRE is useful in *in-vivo* medical applications, where scans have to be completed in a few seconds, and signals are usually very strong [76, 77]. Due to the low signal intensities and sensitivity to magnetic field inhomogeneities, GRE is not suitable for imaging of foams (as discussed in Chapter 3), and is included here for completeness as the second basic image acquisition methodology in MRI.

Many other techniques exist, some mere combinations of the previous methods, some relying on different physical aspects of excitation. They are too numerous to mention, filling dozens of texts, with hundreds of papers written. Most techniques that are not mere alterations of SE or GRE are suitable for exotic purposes, such as constant-time (or single-point) imaging [84], which can be used to image bound nuclei in solids. While many texts give an overview of the most widely used techniques in biomedical imaging, Callaghan's 1991 *Principles of Nuclear Magnetic Resonance Microscopy* [83] provides the most detailed theoretical discussion of all major approaches to resonance localization.

2.3 MRI in Non-Medical Applications

Outside of medicine, magnetic resonance imaging provides non-invasive chemical and physical characterization of regions in the interior of a sample. It has the unique ability to study inhomogeneous objects, from the macroscopic, to the microscopic

and molecular levels. Because of its high resolution, and to distinguish it from biomedical MRI, such imaging is referred to as *Magnetic Resonance Microscopy*.

This section reviews the differences between medical MRI applications, and techniques used in MR microscopy. Table 2.1 adapts and expands Komoroski [1], providing an idea of the range of non-medical applications of MRI.

Sample shapes and sizes vary enormously compared with samples for medical imaging, often requiring non-standard magnet and rf-coil designs. Studies on coal and wood use 1 - 10 cm sections of a sample, which can be sliced to avoid aliasing effects. These samples have yielded linear resolutions of 100 μm using standard imagers [1]. In 1989 Kuhn [82] imaged two-dimensional sections of a plant leaf using a 7 Tesla high resolution imager with 1 Tm^{-1} gradients and a standard two-dimensional spin echo sequence (see Figure 2.3), yielding a pixel resolution of $10^2 \mu m^2$ (with a slice thickness of 100 μm), a one hundred fold increase in linear resolution performance over medical imagers in two-dimensional imaging.

Section 2.4 covers techniques used for volume imaging, which is useful in many areas of MRI microscopy. Figure 2.7 shows an example of the resolution attainable in three dimensions. The image of glass beads (average diameter 1.0 mm) suspended in water was taken at the Notre Dame 300 MHz imaging facility, using a 2mm solenoid rf-transmitter. The voxel (a three-dimensional pixel) resolution is an isotropic $22^3 \mu$m^3, which is roughly 45 times the linear resolution typically used in medical imaging. The signal per voxel is therefore a factor 45^3 or nearly 100,000 times smaller! Such resolutions in three dimensions require expensive hardware, as well as long acquisition times, making two-dimensional imaging the more widely used method to date.

Two-dimensional spin echo techniques successfully studied aging and inhomogeneities in rubber and other elastomeric materials in 1989, and phase separation in

Table 2.1. Non-Medical Applications of MR Microscopy, Based on a List Published by Komorosky in 1993 [1]

Polymeric Materials

Manufacturing defects
Voids, occluded solvents or particles, cracks, channels

Phase structure
Mixing of blends, composites, fillers, plasticizers, foams

Reactions
Polymerization, thermoset curing, adhesives, crosslinking

Diffusion
Swelling agents, solvents, gases

Environmental effects
Aging, wear, mechanical or other stress, oxidation, heat distribution

Chemistry & Chemical Engineering

Reactions in solutions
Spatial heterogeneity of reactants, products or conditions, oscillations, kinetics.

Solid state reactions
Anisotropy of reactions, kinetics

Chromatography
Column packing, band spread, elution

Coal
Pore size, microstructure

Flow
Fluid dynamics, turbulence, multiphase flow

Bioreactors
Design

Inorganic Materials

Ceramics
Cracks, voids, binder distribution

Oil well cores
Physical defects, fluid quantification, distribution and mixing, diffusion, flow

Metals and crystals
Hydrogen distribution, current flow, defects

Agriculture & Food

Wood and plant biology
Knots, defects, water flow and diffusion, disease

Soil and grain
Water content, distribution and transport

Agricultural products
Damage, ripening, diseases, insects, baking, storage, spoilage

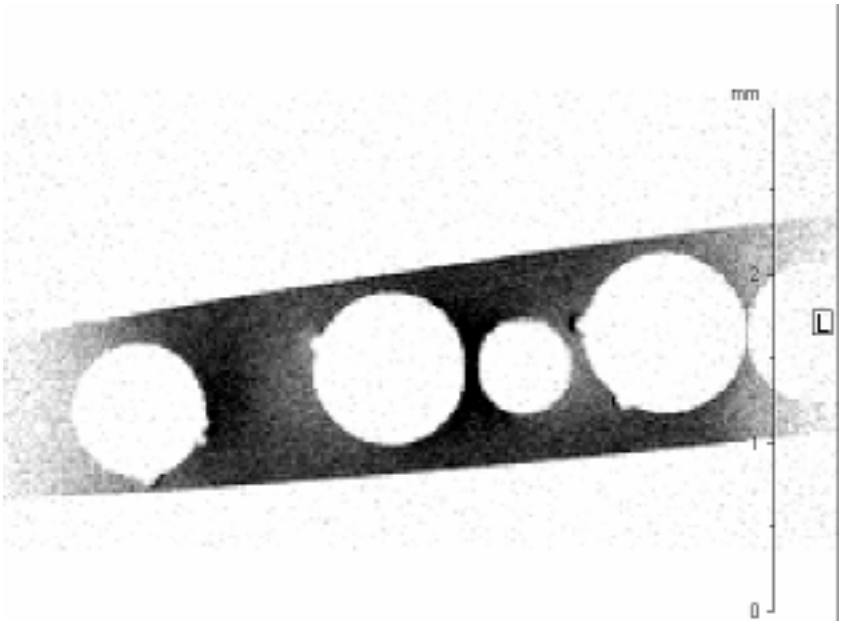

Figure 2.7. Glass Beads Suspended in Water: A slice from a three-dimensional spin-echo acquisition shows T1 reduced water inside a 1.2 mm capillary filled with glass beads (average diameter is 1.0 mm). Isotropic voxel resolution is 22μm. The small distortions of the beads surfaces are dust particles.

1991 [85], obtaining resolutions of 30 x 30 x 300 μm^3. Heil analyzed water migration and void formation in baking biscuits [86], no doubt contributing a great deal to the unsurpassed quality and homogeneity of today's packaged biscuits! German *et al.* investigated foam drainage by measuring the water content inside a column of liquid foam over time [87]. In keeping with this spirit, they evaluated the drainage characteristics of beer foam [88], reinforcing the importance of MRI as a tool to improve the lives of people everywhere.

Foams are a very good example of how MRI of physical materials differs from biomedical MRI, and why physical MRI requires a thorough understanding of imaging parameters and the interplay of different physical effects during imaging, and places unusually high demands on many imager components.

German *et al.* were not able to distinguish more than a few isolated large bubbles during their investigations, due to the rapidly evolving nature of the sample, including simultaneously shifting bubble boundaries, liquid drainage and gas diffusion.

Biomedical imaging limits the ways in which a subject can be altered, or "optimized" for the purpose of imaging. Luckily, the subjects usually start out with good potential. Not so in MR microscopy, where researchers often struggle to obtain signal from inorganic materials or microscopic samples. Careful selection and optimization of the sample are as important as the hardware and imaging method. Gonatas *et al.* succeeded in imaging two-dimensional slices of an optimized foam, measuring the bubble size distributions over long periods of time [46]. They were able to control the coarsening and drainage rate well enough for their purpose, while using gradient and rf-hardware capable of resolving close to 100μm.

2.4 Imaging of Volumes

Many purposes require the exact shape or structure of a feature under investigation. In biomedical MRI the experienced radiologist can often infer from a two-dimensional image which section of an organ is seen, and can make further assessments of its extent in the third dimension. For less well studied subjects, or for complex materials, this option does not exist. Imaging should provide a means to visualize the third dimension, and indeed it does. This section discusses various techniques used in three-dimensional imaging, as well as their respective advantages and disadvantages in imaging liquid foams.

Three-dimensional images can be reconstructed from series of two-dimensional slices acquired with conventional SE or GRE methods. These methods are inefficient, however, when trying to acquire more than a few slices, and often result in either incomplete reconstructions (due to slice spacing), or multiple aliasing, in which the slices overlap. As discussed in Section 2.2.5, slice selection is never homogeneous, and requires very short and powerful rf-pulses for each slice to be imaged, in order to attain reasonable resolution, putting tremendous demands on the imager and resulting in unacceptably long acquisition times.

We wished to study the evolution of liquid foams in three dimensions, which required visualizing a continuous space as homogeneously as possible. The several ways to look at a foam present different possibilities and limitations for using MRI. A liquid foam can be seen as a collection of isolated gas cells, or as a network of edges and vertices that contain (mobile) liquid, similar to a network of blood vessels in biomedical imaging. The faces resemble solid membranes, and, in a sufficiently dry foam, the entire network structure can - as far as MRI is concerned - behave like a solid.

MRI approaches each case differently, though none is ideal for imaging a material as complex as a liquid foam. This section will review some of the techniques we considered for three-dimensional imaging of foams.

2.4.1 Non Slice-Selective Imaging

True volumetric imaging can be done quite ingeniously, using all of the already familiar concepts. The major difference is the first step, which omits slice selection. Instead of a slice selective rf excitation in the presence of a magnetic gradient, the 90° pulse is applied with no magnetic gradient present. The pulse envelope is a close approximation to a rectangle, with rise and fall times (slopes) determined by the imager's basic rf-frequency (the resonance frequency). The bandwidth of the rf-pulse is the inverse of the duration of the pulse and is of order t_p^{-1} [83].

Figure 2.8 shows the generic three-dimensional spin-echo (SE3D) sequence in the familiar format. Instead of a slice selection gradient, the sequence uses two phase encode directions instead of one to encode the second and third spatial dimensions. In a typical imaging sequence of 128 x 128 x 128 data points, the imager acquires 128 phase encode steps (repetitions) along the first phase encode axis, then 128 phase encode steps along the second phase encode axis. The efficiency of this method arises from eliminating the series of slice excitations (which require extra rf-pulses and slice selection gradients) within a single repetition.

A further advantage arises from using a spin echo. The 180° pulse is applied after the resonance frequency is encoded along the read axis (shown in Figure 2.8). This 180° pulse has a finite excitation bandwidth, determined by its duration. Hence only spins contained within the frequency range of the 180° pulse will be refocused at time TE, when the echo is recorded. This feature is of great importance during foam imaging experiments, allowing us to select the resonance frequency of water

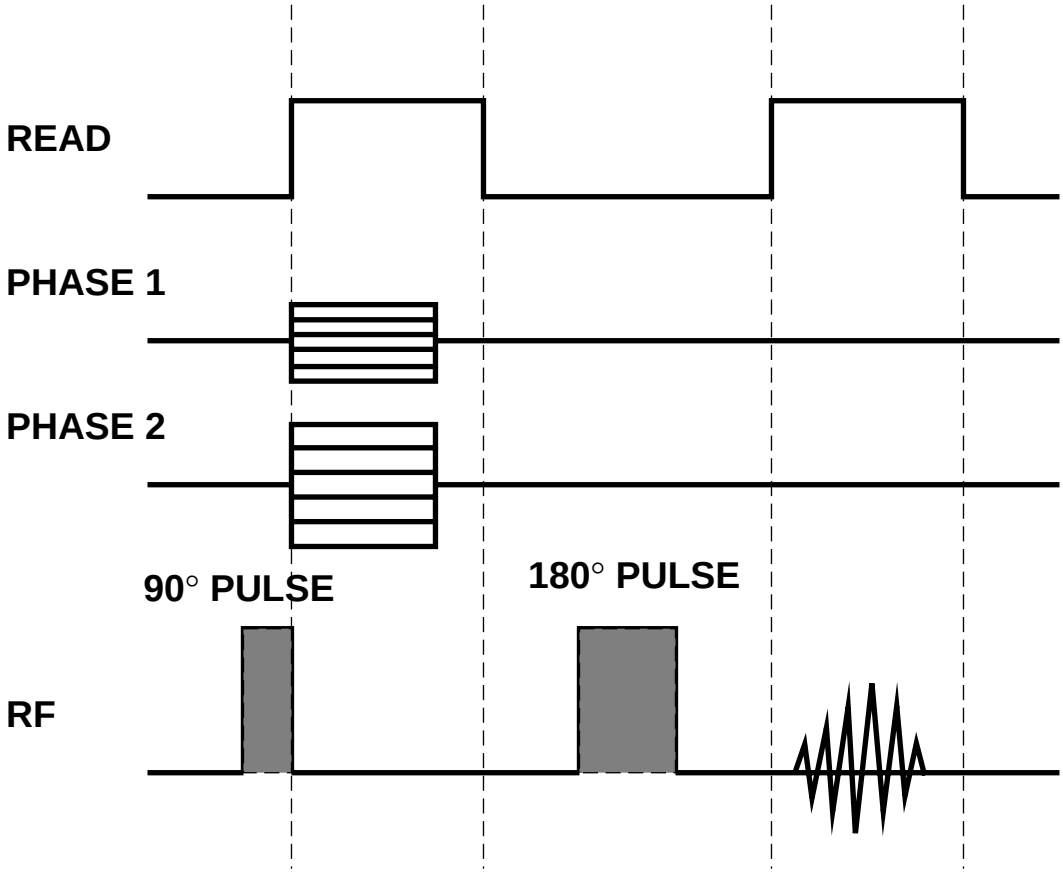

Figure 2.8. Three-Dimensional Spin Echo (SE3D) Pulse Sequence: The schematic shows the timing for the three gradients and the rf transmitter/receiver channel. Transverse magnetization is achieved without a gradient field, and two spatial dimensions are consecutively phase encoded.

accumulations at the bottom of the sample to remain outside the excited frequency range!

The technique relies on so called *hard-pulses*, meaning very short bursts of rf-energy, which require much power. The 90° rf-pulse must now excite nuclei contained in a large volume (instead of a slice) rapidly enough to excite a sufficiently wide range of frequencies. Here again, the second 180° pulse is most important. It must be short enough to excite the full frequency bandwidth inside the desired imaging volume, and powerful enough to invert the net magnetization. By design, the 90° and 180° pulses have the same amplitude, with the pulse duration twice as long for the 180° pulse. Selecting the correct width for the 180° pulse, and finding the correct pulse power for full transverse magnetization, result in optimal signal throughout the imaging volume.

During the high resolution foam imaging experiments with the 300 MHz imager at Notre Dame we frequently used the rf-amplifier at the maximum allowed power level for a series of rf-resonators. Under these conditions it becomes very important to continuously cool the resonator. The rf-hardware specifications warn about strong frequency drift and jumps due to heat accumulation at high power. While running the imager at high duty cycles, and maximum allowed rf-power for several days during many experiments (with both water and air cooling for gradients and rf-resonators), we did not observe any serious drifts or jumps beyond regular dissipative adjustments to the basic frequency. Figure 2.7 (discussed in Section 2.3) shows a slice from a high resolution SE3D acquisition, which took about four hours.

2.4.2 Imaging of Gas

Gases such as ^{3}He, ^{19}F and ^{129}Xe possess a net nuclear magnetic moment, and can theoretically be used for MRI. High resolution NMR spectroscopy can easily reveal

the presence of single atoms of ^{13}C or ^{19}F in a molecule (often requiring many days of acquisition) [68], so theoretically we could use polarizable gases for imaging, despite their low densities. Foams consist mainly of empty space (*i.e.* gas), making them suitable for gas imaging.

Medical imaging of lungs and lipid bilayer membranes is notoriously difficult [89] with conventional techniques. Spin densities in atmospheric pressure gases are too low even to obtain two-dimensional images during a single breath cycle (lungs) or heart beat. In 1994 Albert *et al.* [89] developed a new technique using laser-polarized ^{129}Xe gas to image lungs in mice, as well as dissolved xenon in cell membranes. The laser-polarization increased the polarization density (magnetization) of the gas by a factor of 10^5, enabling faster image acquisitions than in regular proton based clinical MRI. A drawback is the loss of polarization that occurs during consecutive excitation cycles, which limits the number of excitations (images) that can be obtained using a trapped volume of gas.

Saam *et al.* studied edge enhancement effects at gas-solid boundaries using hyper-polarized ^3He [90]. While the technique is promising, the signal enhancement occurs near impenetrable boundaries only (where diffusion is significantly reduced), and we do not expect any significant signal enhancement near the more permeable membranes in liquid foams.

Using hyper-polarized gases to image bubble volumes is very promising. Setting up polarized gas (or solution) based experiments will be initially time consuming, and we have not attempted them for that reason. However, the techniques for creating hyperpolarized gases, particularly xenon (which has a tremendous cost advantage and lower diffusion compared to helium), are well established. Song *et al.* [91] describe the development of applications in materials research. Albert [92] reviews appropriate pulse sequence methodology and gives a detailed discussion of

relaxation and material (tissue) interactions, specifically addressing the need for very low flip angle techniques to preserve polarization. A standard imager would need no modifications, beyond a broadband rf-amplifier and suitably tunable rf-transmitter.

In summary, hyperpolarized gas imaging can provide unsurpassed signal and fast acquisition times, making it ideally suited for imaging materials that contain large empty volumes. Depolarization is of concern when trying to study material evolution over time, and needs to be addressed using suitable imaging sequences.

2.4.3 Imaging of Solids

Solids have very short transverse relaxation times T2, due to strong dipolar spin-spin interactions and the common presence of ionic bonds and paramagnetism in the sample. This rapid dephasing of the FID, referred to as *Bloch decay* [83], poses a formidable barrier to imaging. Limitations due to signal strength and dephasing that apply to imaging of solids also apply to liquid and solid foams.

The resonance line width in solids is the major factor limiting the attainable resolution. The localized magnetic fields experienced by the excited nuclei fluctuate strongly, due to the short range nature of the dipolar spin coupling in a solid molecular environment, resulting in a broad resonance line. The width $\Delta\nu$ of the NMR signal is defined as the width of a Lorentzian line at half its maximum height:

$$\Delta\nu = \frac{1}{\pi T_2}. \tag{2.6}$$

In order to distinguish two resonance curves that are centered inside neighboring pixels, their peaks must be separated by $\Delta\nu$. Typical resonance line widths in true solid materials can be 100 kHz, but most elastomeric materials, such as rubber and polyurethane have resonance line widths on the order of 5 kH to 20 kHz. Acquiring 128 data points at $\Delta\nu$ = 5kHz then requires a frequency encoding range (sweep

width) of 640 kHz. Such wide frequency ranges result in very low S/N and place tremendous demands on magnetic gradients.

Callaghan [83] discusses limitations and possible approaches to imaging solids in great detail. Line narrowing techniques such as Magic Angle Spinning (MAS) are useful in true solids, but require rotational speeds of several kHz, which would certainly leave a liquid foam sample in a less than ideal state. Chapter 3 discusses appropriate relaxation agents to homogenize the localized magnetic fields to narrow line widths in liquid foams.

Fortunately this line narrowing sample preparation allows us to use regular volumetric imaging techniques for liquid foams, which are easier than poorly developed solids imaging techniques. This approach often applies,as in the case of porous media (*i.e.* solids), in which filling the connected space with a more suitable imaging medium (*e.g.* water) produces a reverse image. Assink *et al.* [93] and Kose [52] have imaged open-faced solid foams in this manner.

If this approach is not possible, a nascent technique referred to as "single point" or "constant-time" imaging may help [83, 84]. In this technique, phase-encoding gradients provide all spatial information, so it is not limited by bandwidth or relaxation times. However, the three separate phase encode steps for each voxel result in very long acquisition times and high duty cycles for the imager. The technique is therefore suitable only for true solid (*i.e.* motionless) materials.

CHAPTER 3

THREE DIMENSIONAL IMAGING OF FOAMS

3.1 Sample Preparation

3.1.1 The Base Liquid

Liquid foams contain very little actual liquid per net volume. The liquid largely resides in a network of vertices and edges. In foams with a finite (non-zero) liquid fraction ϕ, the junctions of faces -*the edges*- and of edges -*the vertices*- are called *Plateau borders*, after the Belgian mathematician who investigated the rules of equilibrium for conjoined soap films in the 19th century [48].

For foams in which the faces can be treated as surfaces with zero thickness, Plateau's rules state that vertex stability requires two conditions:

1. The edges form at the intersection of three faces (or films), with mutual angles equal to 120°.

2. The vertices form at the junction of four edges, with mutual angles equal to the tetrahedral angle $cos^{-1}(-1/3)$, or ∼109.5°.

In practice these rules apply to less ideally dry foams, with finite thickness in the Plateau borders and volume liquid fractions of about one percent [28, 29, 30, 34]. Weaire showed in 1996 that for foams that are not near the ideal dry limit, metastable eightfold vertices can exist [34].

These considerations are important in the preparation of foam samples for MRI experiments, which face a set of constraints:

1. MRI requires the presence of hydrogen nuclei contained in water. A high liquid fraction is therefore desirable.

2. A liquid fraction above $\phi \sim 10\%$ in a heterogeneous foam leaves spherical bubbles suspended (*wet limit*) within the liquid phase.

3. Vertex instability and motion cause artifacts during image acquisition.

4. Gravitational drainage leads to thinning, motion artifacts, drying and collapse during experiments.

Studies of bubble shapes and topological distributions require distinguishable interfaces between two neighboring bubbles. The bubbles must be polyhedral, not spherical as at high liquid fractions or in suspensions. The faces have a smaller membrane curvature than the Plateau borders at their joining edges and vertices. They contain very little liquid, and do not significantly contribute to drainage. This geometry leads to very large interface areas between the liquid and the gas (air) in the sample, with liquid present only inside the network of edges and vertices.

As a result, liquid foams with polyhedral bubbles produce very little signal for their volumetric size, since at most a few percent of the total volume contains free protons.

We measure the wetness of a foam in percent of volume liquid fraction ϕ. Optical studies of surface bubbles in foam mixtures confirm that in order for foams to contain only polyhedral bubbles, less than 5% volume liquid fraction is desirable. While a suspension of spherical bubbles requires significantly more than 10% liquid, we find that even above 5% the liquid sometimes accumulates in small pockets, in which one or a few spherical bubbles can remain suspended. These bubbles will not participate in diffusion driven coarsening (since they possess no thin film walls) and basically constitute a small structure unto themselves, interfering with

measurements of neighboring bubbles in ways which we cannot quantify. We avoid such accumulations by keeping the total liquid fraction in the sample as low as possible, while allowing sufficient liquid in the films and edges to permit substantial coarsening without drying the sample.

We determined the liquid fraction in the samples by measuring the volumes of the foam and the accumulated liquid over time, until all liquid has drained out of the sample, and the foam collapsed. We mixed purified water (70%) and glycerin (30%) with a commercial detergent (a mixture of ionic and non-ionic surfactants), providing a non-drying, easy to use liquid. Fluorescein (Sigma Chemicals) is added to provide contrast under UV-lighting.

We also used optical means to examine surface bubble size distributions in gelatin based foams. A 720 x 470 pixel CCD camera set at a shallow depth of field recorded coarsening over 24 hours. We attached a micrometer scale to the front of the sample as a size reference. The study estimated the fraction of bubbles that were too small to resolve in early two-dimensional MRI images of gelatin foams by Gonatas *et al.* [46], and first three-dimensional acquisition by Prause *et al.* [94] in 1995.

We processed the images using a simple thresholding algorithm to create binary images (black and white only). A Laplacian edge enhancement filter creates an image with reasonable accurate outlines of the bubble edges [95]. Figure 3.1 shows the raw images (with some contrast adjustment for printing purposes) and edge outlines at two stages of coarsening. Due to a lack of appropriate computer programs at the time, we printed the images, and measured the bubble diameters by hand, binning them into sub-threshold ($< 200\mu$m), near threshold (200 to 400μm) and above threshold ($> 400\mu$m) categories. Figure 3.2 shows that after 10 hours, the fraction of bubbles below 200μm diameter is less than 20%.

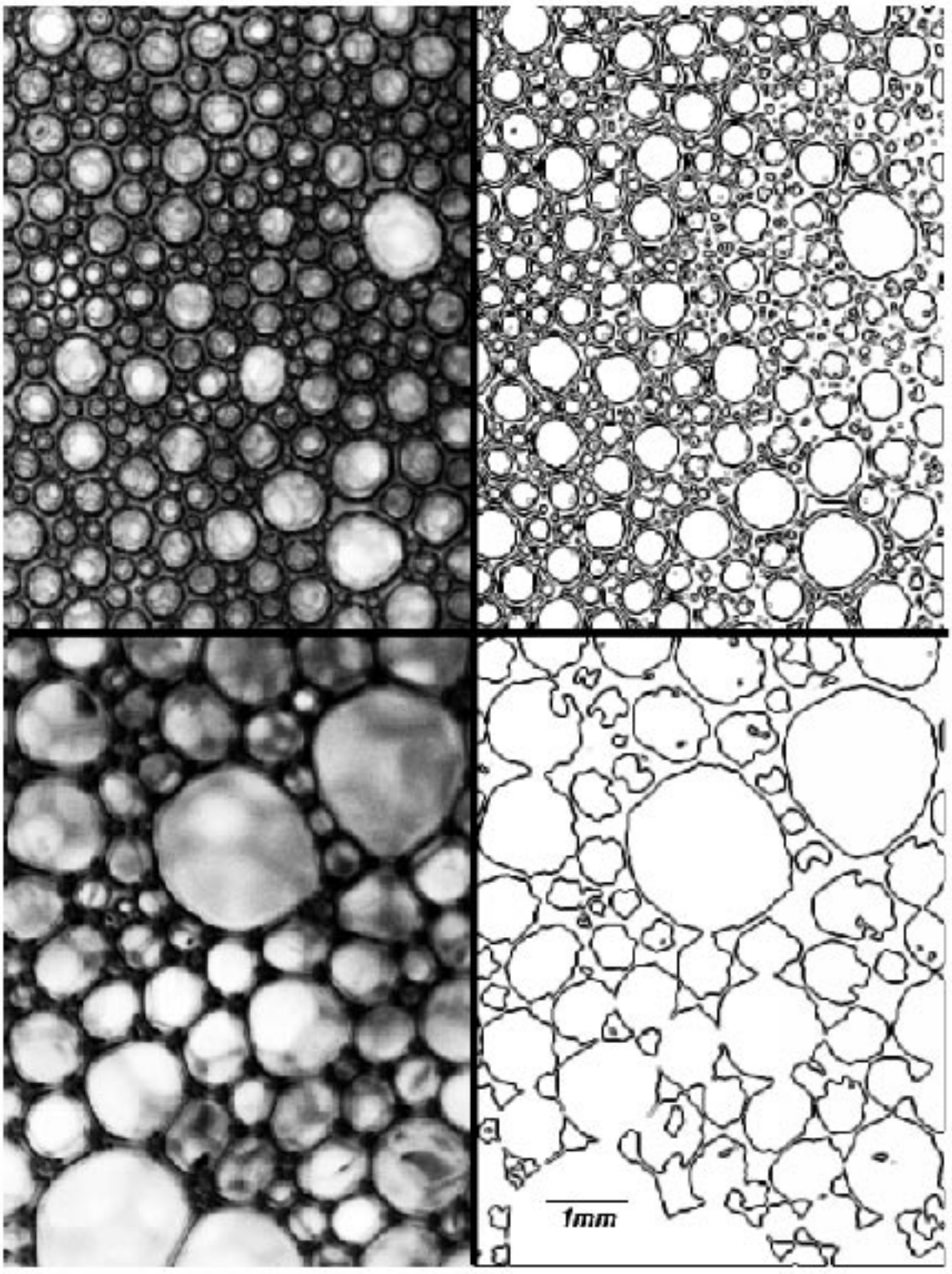

Figure 3.1. Images of Surface Bubbles After 4 (top) and 12:30 Hours (bottom). The left side shows the images after thresholding and edge enhancement.

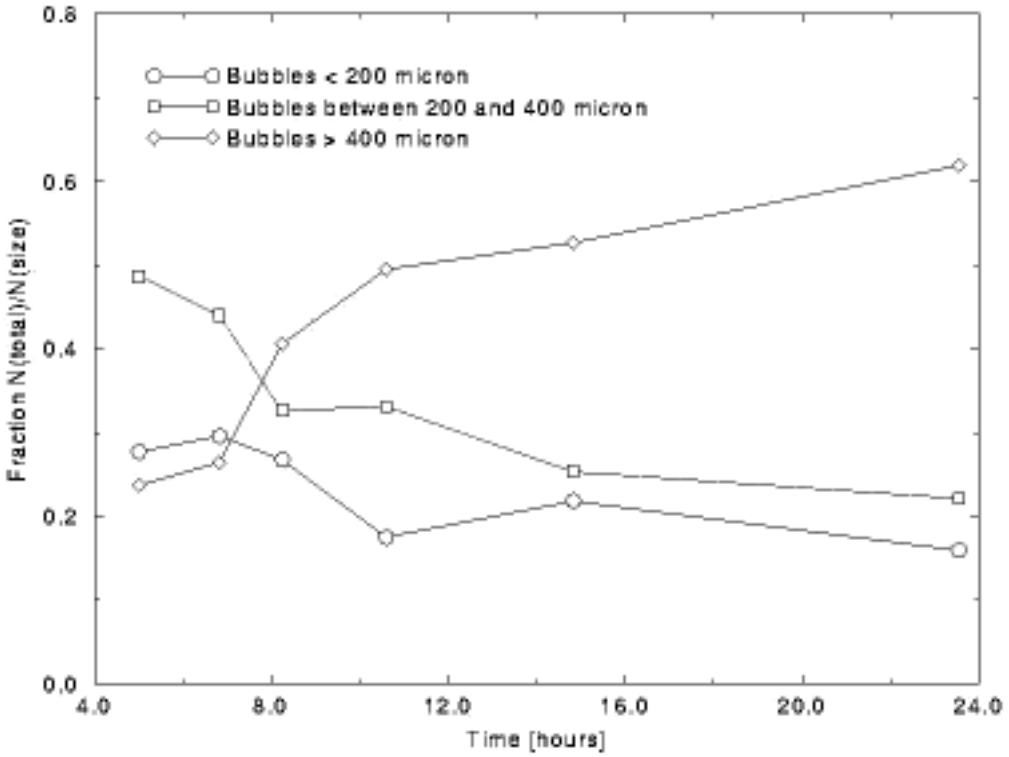

Figure 3.2. Bubble Size Distributions for Surface Bubbles in a Gelatin Based Foam. The foam was created using an electric mixer. The bubble sizes were analyzed by manually fitting circles on images obtained with a CCD camera.

The optical studies we conducted allowed us to verify bubble shapes, drainage times and bubble size distributions (for surface bubbles only) for a large variety of liquid compositions and foam producing techniques. The experience we gained in digital image acquisition using CCDs, as well as the development of image analysis routines for two-dimensional domains, aided our investigation of the flow and shearing dynamics of two-dimensional bubble layers.

We tested a number of liquids for their suitability to MRI experiments. The liquid in the foam sample needs to have high viscosity and film strength, thus limiting diffusion while draining slowly, without drying out over long periods of time. The liquid would also have to be suitable for NMR imaging of hydrogen. Mineral oils, agar and many protein solutions contain insufficient free hydrogen (nuclei that are not bound to a large molecule, and whose resonance frequencies are not shifted), or are too magnetically inhomogeneous to allow imaging.

We found that glycerin based solutions did not provide stable enough foams, while the water content was high enough to provide a localizeable resonance signal. Glycerin/water based foams coarsened rapidly for about 24 hours before collapsing. Wall breakage occurred at all times.

Polyvinyl alcohol (PVA) can be hydrated to achieve a desired level of liquid viscosity, and foams prepared using PVA and SDS as a surfactant were stable for between 24 and 48 hours. However, the foams drained very rapidly, leaving $\ll 1.0\%$ liquid within the foam after only a few hours. We measured the resonance line width of PVA solutions, which is greater than 1200 Hz, compared with a few tens or hundreds of Hertz for other solutions we tested. The extremely low liquid fraction, together with a fast transverse relaxation time below 0.3ms, made it impossible to generate a spatially localized NMR signal in the amount of time available to observe the foam during coarsening.

We found that a highly purified protein gelatin solution (Norland Hi-Pure brand, fish skin derived Teleostean gelatin) fulfills the requirements best. The foams created with water/gelatin solutions resisted film rupture, drying and polymerization over many days. Drainage was slow and consistent, continuing measurably for up to 36 hours. Optical studies and experiments with foams based on other gelatins (agar, or Sigma Chemicals brand Teleostean gelatin) produced unstable foams that collapsed within 24 hours. Our optimal mixture was 50% (by volume) Norland gelatin content, with the rest consisting of water and added surfactants and relaxation agents.

Glycerin based foams are used in two-dimensional studies of rafts and layers, and are useful in experimenting with foam generating techniques. Gelatin is very hard to remove from surfaces when hardened and is best used in imaging, where its stability is crucial.

3.1.2 Magnetic Susceptibility Matching

Interfaces between regions of different proton densities and magnetic susceptibilities lead to localized magnetic inhomogeneities in a sample [83]. These inhomogeneities act as random local magnetic gradients, causing spins to dephase more rapidly than in magnetically homogeneous samples that are affected by spin-spin dipolar interactions only [74]. The faster spins dephase, the less signal the FID produces.

This fact is exploited in medical imaging, where contrast between tissues is often enhanced through the use of contrast agents, which alter the proton density (water storage), or magnetic relaxation times[1] T1 and T2 of specific tissues [81].

Foams represent an extreme case, however, where interfacial areas are very large, and proton density differences between the liquid and gas are many orders of magnitude. Large magnetic inhomogeneities arise from susceptibility differences caused by the presence of paramagnetic oxygen in the air, and the diamagnetic properties

[1] see Chapter 2: Introduction to Magnetic Resonance Imaging.

of the macro-molecular protein in the gelatin. While we cannot change the foam's structure - which is the subject of investigation after all - we can address the low signal and magnetic inhomogeneities through careful optimization of the base liquid.

We used a SQUID (Single Quantum Interference Device) magnetometer to measure the magnetization of the base liquid as a function of the applied magnetic field, and for different concentrations of the paramagnetic relaxation agent $DyCl_3$. We took measurements at 0.5 Tesla increments between 0 and 7 Tesla. The liquid samples were held inside sealed 5mm NMR tubes in the evacuated bore of the magnetometer. To compensate for contributions from the NMR tube, sample holder and Teflon tape, an empty tube was used for background measurements and the values subtracted. Figure 3.3 shows the sample magnetization for varying $DyCl_3$ concentrations as a function of the applied field. A transition from diamagnetic (negative) magnetization to paramagnetic magnetization occurs about halfway between 15 mM and 20 mM concentrations of $DyCl_3$. As expected, the magnetization of the samples changes linearly with the applied field.

The magnetization measurements verified the diamagnetism of the gelatin, and indicated the amount of $DyCl_3$ required to effectively null the magnetic susceptibility mismatch with respect to air.

3.1.3 Relaxation Properties of the Sample

To optimize the imaging pulse sequence, we needed to measure the signal's relaxation times T1 and T2 (see Section 2.2.1). Due to susceptibility concerns, the method of choice for three-dimensional imaging is a three-dimensional spin-echo sequence, which requires large flip angles (90° and 180°, respectively). While the susceptibility induced dephasing should keep T2 very small (rapid dephasing), T1 in most liquids is quite large, between several hundred milliseconds and a few seconds for water

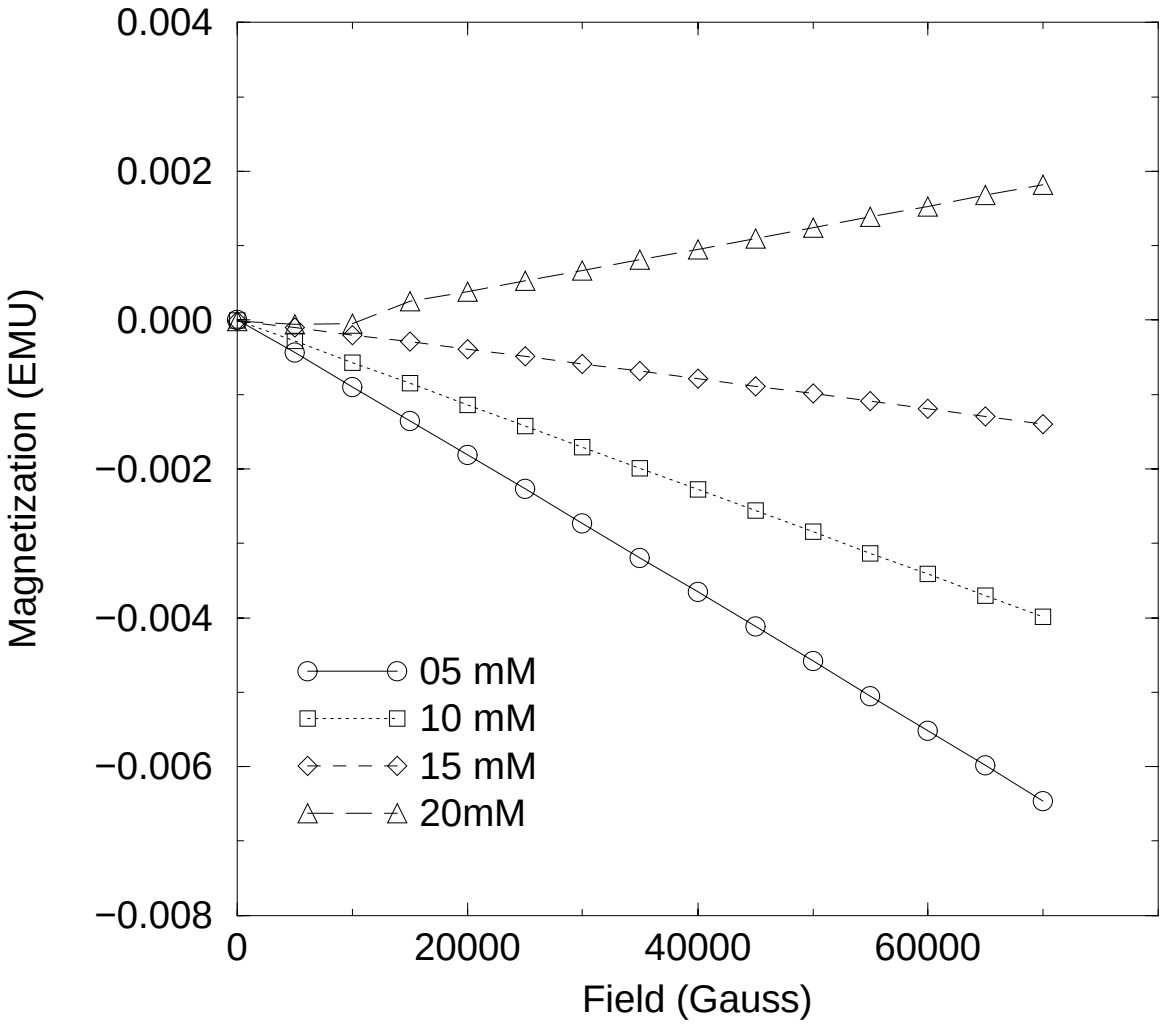

Figure 3.3. Magnetization Measurements: The magnetization values for air have been subtracted from the measurements. A negative magnetization indicates the liquid is diamagnetic with respect to air. Positive magnetization indicates stronger paramagnetism than air.

in a 7 Tesla field. Ionic contrast agents, such as many Gadolinium complexes in human studies [81, 74], or $MnSO_4$ and $CuSO_4$ in non-biological applications, reduce T1 (and to some extend T2).

While we determined the range of $DyCl_3$ concentrations which minimized the magnetic susceptibility mismatch between the liquid and the air, we needed to measure both T1 and T2 for a variety of concentrations of $DyCl_3$ as well as $CuSO_4$, which we added to shorten the longitudinal relaxation time T1.

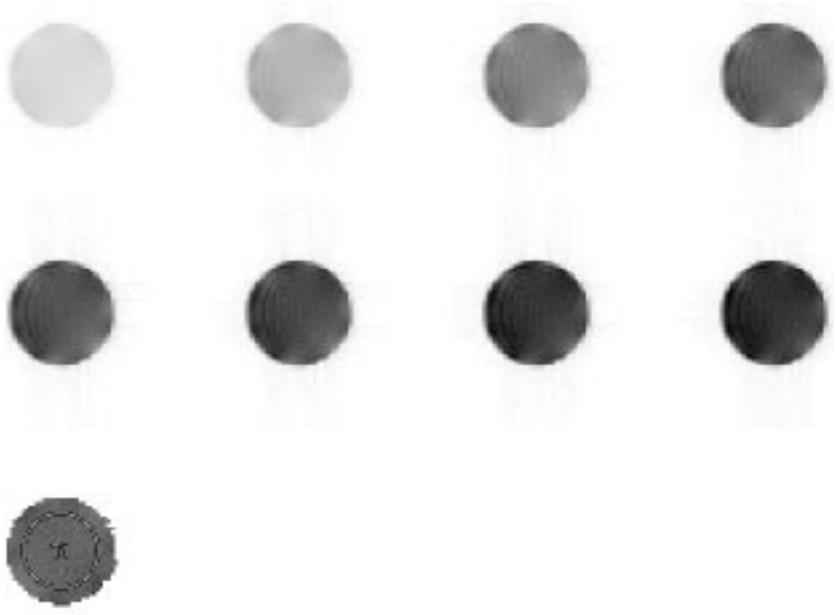

Figure 3.4. Increasing TR: The repetition time TR is increased during a sequence of eight acquisitions of a sample liquid. As TR lengthens, the signal strengthens, as T1 relaxation allows more spins to return to longitudinal magnetization. The image in the third row is a T1 reconstruction, where each pixel intensity is proportional to the spin-lattice relaxation time extracted from the time series. Measuring specific regions in this image allows extraction of T1 from any part or region in the image. See text for details.

At the same time, we monitored the line width of the resonance signal. The susceptibility induced changes in localized magnetic field strength aid the local de-

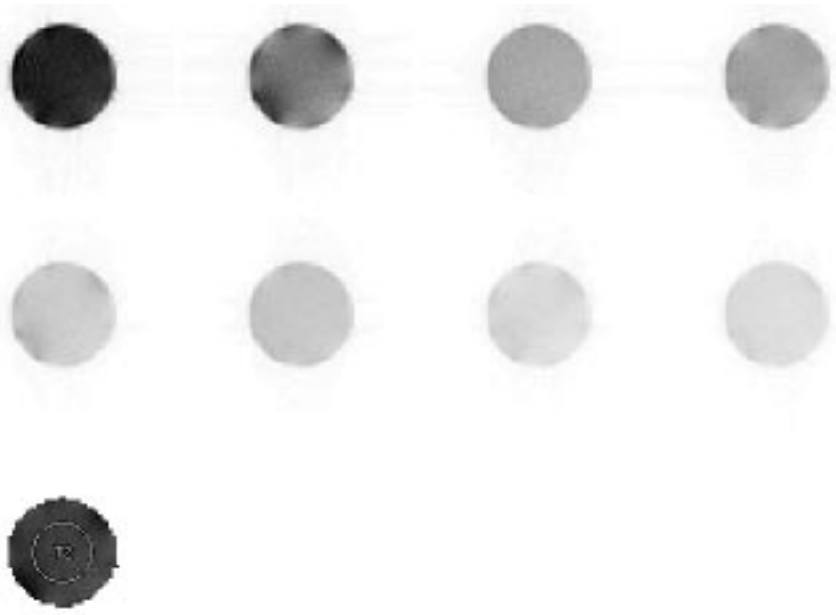

Figure 3.5. Increasing TE: A multi-echo MSME sequence (Carr-Purcell-Meiboom-Gell, or CPMG) with equally spaced echo times provides a series of images with decreasing signal intensities. For each consecutive echo fewer spins rephase. As in Figure 3.4 this decay gives T2 information. See text for details.

phasing of spins, with a characteristic time constant called T2*, which is generally shorter than T2. The relaxation line width at half maximum in the absence of gradients is $1/\pi T2^\star$ [83]. In magnetically homogeneous samples, T2 determines pulse sequence parameters, such as TE, and the number of echoes or slices that can be acquired in a single repetition. When T2* differs markedly from T2, we use it instead. Measuring both T2 and T2* for different concentrations of $DyCl_3$ and $CuSO_4$ is another way of minimizing magnetic field inhomogeneities by minimizing the difference between T2 and T2*.

The Bruker Avance imager and ParaVision acquisition software package provide a set of tools to measure T1 and T2 at any point or region in a sample [96]. A basic 2DSE imaging sequence (the Bruker name is Multi-Slice Multi-Echo: MSME) allows a series of rephasing 180° pulses, from which we read the signal from each echo as a separate image. While each application of a 180° pulse recovers all dephasing due to T2*, true T2 dephasing (spin-spin interactions) will lead to loss of signal with each echo [83, 74]. Figure 3.5 shows images obtained with a sequence of eight echoes.

We can measure T1 relaxation by altering the repetition time during a series of acquisitions. If TR is much smaller than T1, subsequent excitations will create very little transverse (exact 90°) magnetization, resulting in low signal intensities. Figure 3.4 shows 8 images of a slice, obtained with increasing TR.

Substituting TE and TR into the appropriate Bloch equations, they now become:

$$\mathcal{M}_z(t) = \mathcal{M}_0(1 - e^{-TR/T_1}), \tag{3.1}$$

and

$$\mathcal{M}_{xy}(t) = \mathcal{M}_0 e^{-TE/T_2}. \tag{3.2}$$

Using the same intensity scaling for all images in the series, and a precise 90° pulse to eliminate correction factors for different transverse magnetizations $\mathcal{M}_0$,

we can extract T1 and T2 by fitting the intensity (which is proportional to the magnetization) information contained in each pixel as a function of the time steps TE, or TR respectively [96].

We prepared a series of liquid samples, each containing the same basic ingredients as the base liquid that we use to create the foam samples. While we could measure T1 and T2 using the foams directly, simply measuring the base liquid relaxation is much faster, both in preparation and experiment time. T1 and T2 are unaffected by the magnetic homogeneity inside the sample, so that only $T2^{\star}$ differs between a liquid and its corresponding foam. The amount by which $T2^{\star}$ changes between a given liquid and its foam counterpart measures how well we have avoided susceptibility mismatches.

We varied $CuSO_4$ and $DyCl_3$ concentrations independently while imaging a series of increasing TE's and then TR's. Figure 3.6 shows the changes in magnetization for constant 15 mM $DyCl_3$ and varying concentrations of $CuSO_4$. Figure 3.7 shows the magnetization for varying concentrations of $DyCl_3$ while $CuSO_4$ is held constant at 15 mM. Table 3.1 summarizes T1, T2, and $T2^{\star}$ for a series of contrast agent concentrations:

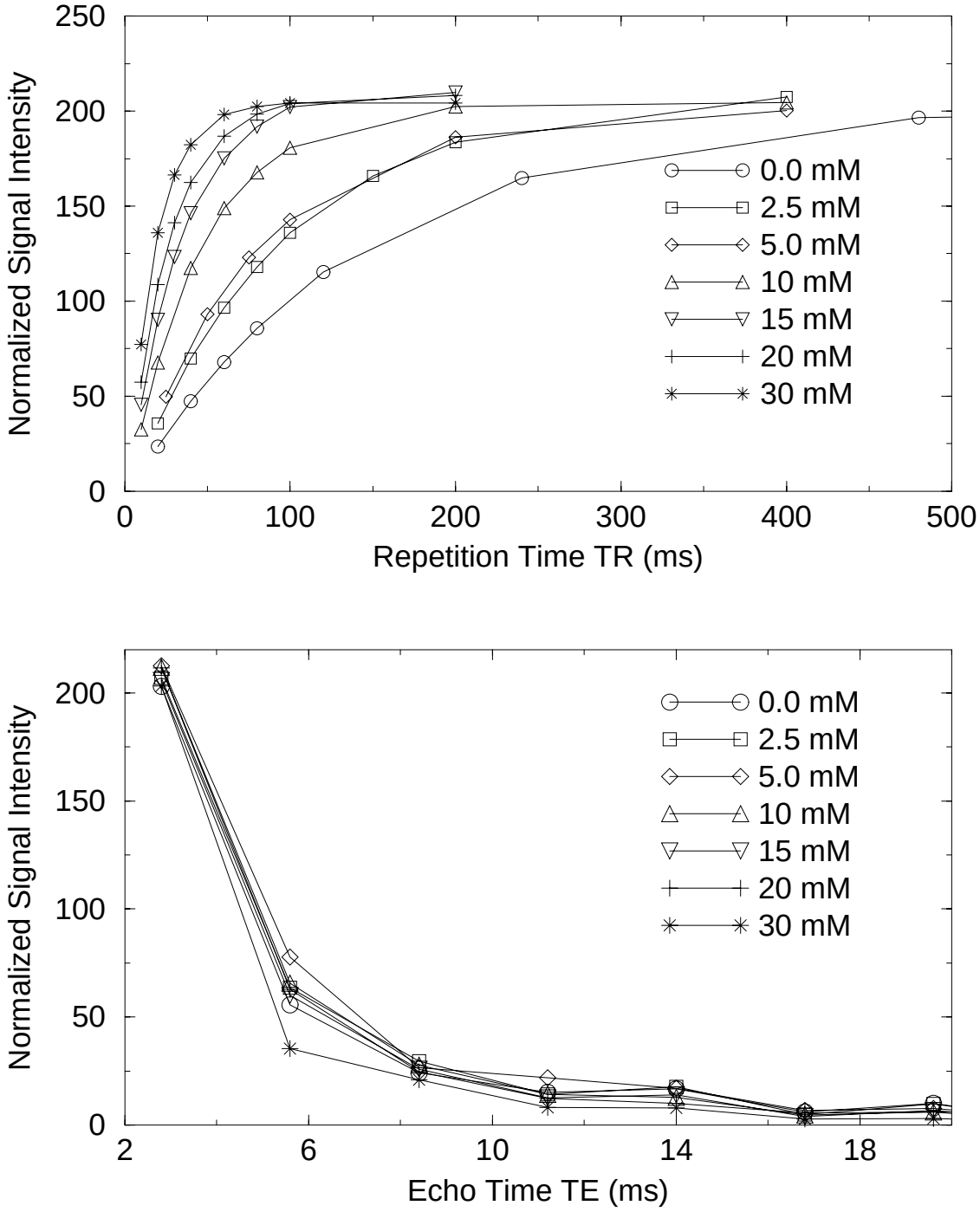

Figure 3.6. $CuSO_4$ concentration series: Signal intensities for varying concentrations of $CuSO_4$, for a series of TR and TE.

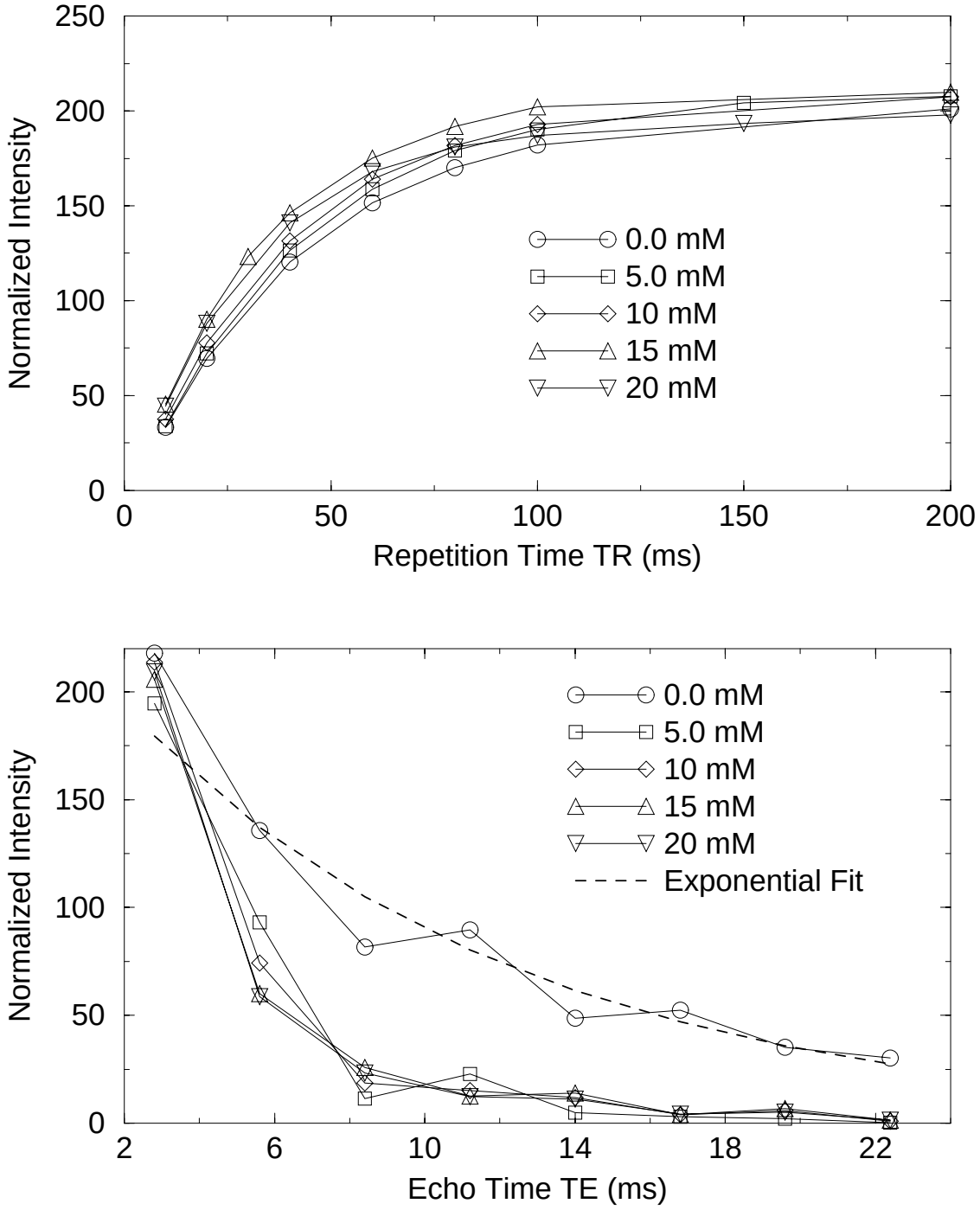

Figure 3.7. $DyCl_3$ concentration series: Signal intensities for varying concentrations of $DyCl_3$, for a series of TR and TE.

Table 3.1. Relaxation Times for Variations in Concentration of $DyCl_3$ and $CuSO_4$.

Constant $DyCl_3$ = 15mM

$CuSO_4$ concentration (mM)	0.0	2.5	5.0	10	15	25	30
T1(ms)	142	95	77	45	32	25	17
T2(ms)	2.4	2.6	3.0	2.7	2.5	2.5	1.8
T2*(Hz)	300	480	460	650	500	860	780
T2*(μs)	1061	663	692	490	637	370	408

Constant $CuSO_4$ = 15mM

$DyCl_3$ concentration (mM)	0.0	2.5	5.0	10	15	25	30
T1(ms)	43.4	-	40.3	35.5	32.0	29.9	-
T2(ms)	8.52	-	3.1	2.6	2.5	2.4	-
T2*(Hz)	1610	-	1750	1000	500	1050	-
T2*(μs)	197	-	182	318	637	303	-

3.1.4 Preparing Stable Foam Samples

We can produce liquid foams in three different ways:

1. Chemical reaction: many industrially important foams and porous materials are created by outgasing during chemical reactions [6]. Polystyrene and Polyurethane foams are created this way, where, as the reaction slows, the liquids polymerize and arrest at the desired stage of coarsening. The process is complex, difficult to control, and would introduce numerous problems with respect to imaging (time scales, chemical composition), which we have just spent considerable time eliminating!

2. Agitation: Whipping up a good foam is as easily done as said. A cheap electric mixer from Sears can generate a decent froth in no time. These foams are initially very wet, $\phi = 50\%$, but drain to less than $\phi = 10\%$ after a few hours, producing a moderately wet polyhedral foam, with bubble sizes ranging from 30μm to 300μm. The foams are polydisperse, but the bubble sizes are

smaller than for any other means we attempted, giving us the longest time to observe the foams as they coarsen.

3. Gas injection: We tried gas flow through pipette and syringes, which is the preferred method of Weaire and Fortes in producing two- and three-dimensional bubbles. The high viscosity of our base liquid delayed separation of the gas bubbles from the head of the pipette long enough to produce only large (3 to 6mm diameter) bubbles. As an alternative, we used a somewhat more "chaotic" bubble generator, a commercial millipore (fish tank) filter. Gas flow through this filter produced very dry (initial volume liquid fraction $\phi = 3\%$) foam, with an initial average bubble diameter of 2.0mm $\pm$ 0.3mm.

We experimented with different preparation techniques throughout the years, and found that both agitation and "filtering"(gas flow) work well, providing us with different initial wetness and sizes for imaging. We will discuss details whenever they become relevant during the imaging experiment descriptions.

Due to the non-zero liquid fraction, gravitational drainage of liquid through Plateau borders and edges affects coarsening in the foam, as well as gas diffusion across the films, vertex coalescence and wall breakage. During the course of the experiments we found that holding the sealed glass cells containing the foam at a constant temperature of about 280°K limited the rate of drainage and kept air from drying the foam walls. Samples prepared in this manner coarsened without breaking down for as long as six days, at which time the gelatin in the faces started polymerizing, inhibiting growth.

3.2 MRI of Foams

3.2.1 History

MRI of foams was first performed in the context of studying porous materials. Many solid foams consist of little more than a network of edges connecting the vertices, with no faces separating the domains. Assink *et al.* obtained density profiles of liquid draining through such open pore spaces in solid foam [93]. Kose used water to fill the pores of a polyurethane foam and obtained three-dimensional images of the water distribution [52]. His choice of a foam with very large pore sizes (2 to 6 mm in diameter), and edges that were several hundred micrometers thick, enabled him to acquire a "negative" image of the foam, where the pore space contains signal, and the edge network is empty (similar to the technique we proposed for using hyperpolarized noble gas inside closed liquid bubbles). Using a high linear resolution of 150μm he was able to resolve the particularly wide edges and vertices in his sample. The experiment was successful, and his analysis of the structure of two dozen bubbles (traced by hand) closely agreed with the findings of Matzke [50, 51], in that he found no evidence of the ordered polyhedra that were suggested by Kelvin [49] or Weaire and Phelan [29].

Early imaging of liquid foams was independently performed by German *et al.* [87, 97, 88, 86] and Gonatas [46]. Both employed two-dimensional spin-echo sequences to obtain single slice images. The experiments conducted by German *et al.* concentrated on extracting one-dimensional spin density profiles in absence of a phase encoding gradient, which did not require optimization of the sample's MRI signal even at time resolutions below one minute (inferred by the author from published sequence parameters and standard protocols). The acquisition of full two-dimensional images, however, took well over one hour in very wet beer and egg-white foams,

resulting in images that revealed only few very large bubbles [87]. He could not determine the sizes or structure of individual bubbles.

Gonatas *et al.* in 1995 were able to image two-dimensional slices in a gelatin based foam with sufficient spatial resolution (100 -130μm, non isotropic) to reveal detailed bubble structure. They optimized their base liquid for their low field spectrometer, resulting in acquisition times of 50 minutes for a single, high resolution slice. The images were of high enough quality to manually determine the sizes of individual bubbles, down to a resolution threshold of about 250μm. The results of acquiring time series of two-dimensional slices of a single foam were used to study the changes in bubble size distributions over time [46].

3.2.2 Early Development of Three-Dimensional MRI for Liquid Foams

We began developing suitable techniques and hardware for three-dimensional imaging of liquid foams early in 1995 with visits to the Department of Radiology Magnetic Resonance Imaging Facility at the University of Chicago under Dr. Gregory Karczmar. Our efforts during the visits concentrated on the possibility of using gradient echo techniques for rapid multi-slice image acquisitions.

During two visits in January and February 1995, we imaged several wet foam samples with initial volume liquid fractions $\phi \sim 50\%$. The Biospec imaging facility consisted of a 40cm bore 4.7 Tesla (200 MHz) horizontal bore GE primary magnet, with 10 Gauss/cm gradients and a custom 40 mm rf solenoid transmitter/receiver.

The images we obtained during these trials failed to reveal any distinguishable bubble structure. Due to the short periods of time during which the imaging system was available, we could perform little parameter testing and sequence optimization. Other contributing factors were the inadequacy of sample optimization at the time, as well as the imaging hardware and the selection of gradient echo imaging methods.

The magnetic homogeneity inside the sample, both due to primary field fluctuations and sample susceptibility, was insufficient for the strong demands imposed by fast gradient switching. Typical applications in Biospec imagers require resolutions of 1mm^3, while the foam experiments attempted to push in-plane resolution to $100\mu\text{m}^2$, with 1mm slice thickness. The limited gradient strength imposed the slice thickness, and was the main contributing factor in the failure to distinguish bubble structure. The foams at the time were not stable enough to allow significant coarsening, so that the largest bubbles during imaging were less than 600μm in diameter, which was roughly half the selected slice thickness.

While the visits to the University to Chicago failed to produce usable images, we were able to draw several valuables lessons from these first experiments:

1. The foams needed to drain and coarsen before imaging.

2. Gradient echo methods, - while intrinsically much faster - are too sensitive to magnetic field inhomogeneities and to induction of Eddy currents. Three-dimensional imaging of foams must rely on spin echoes, or possibly constant time imaging.

3. High isotropic resolution would require strong gradient strengths, which could run high duty cycles over long periods of time.

4. Acquisition times for single images should be as fast as possible, and ideally should not exceed the integration time achieved by Gonatas *et al.* for two-dimensional slices.

We obtained a first three-dimensional data set of a liquid foam [94], during a site visit to Bruker Instruments in Billerica, MA in March 1995. We used an 89 mm vertical bore 9.4 Tesla (400Mhz) Bruker primary magnet, with an AMX console

and water cooled gradients providing 38 Gauss/cm for the experiment. The choice of a high field, small bore imager with strong gradients was a response drawn from our conclusions after the experiments in Chicago. Smaller bore sizes result in much more homogeneous primary magnetic fields, which are less aggravating to intrinsic magnetic inhomogeneities in the sample. We designed the experimental method with Dr. Samuel Gravina at Bruker Instruments, and for the first time obtained a true volumetric image of foam.

We placed a whipped gelatin foam inside a 3ml plastic syringe, with an outer diameter of 10mm, and an inner diameter of 8mm. The foam drained for about 90 minutes. A longer drainage time was preferable, but impossible due to the imaging time constraints during the visit. A 20mm shielded birdcage rf transmitter/receiver provided stronger signal to noise ratio than during the previous experiments. More ideally sized 10mm to 15mm transmitters were not available at the time.

We doped with $CuSO_4$ and $DyCl_3$, following Gonatas *et al.* [46]. An inversion recovery sequence measured the longitudinal relaxation time T1 in the sample, which was a surprisingly long 105 ms. This T1 limited the possibility of reducing the repetition time below 160 ms (ideally TR should not be lower than 1.5 * T1 to prevent steady state saturation). A three-dimensional spin echo sequence provided 80 data points along each axis. Taking two averages gave a total acquisition time of 34 minutes. Table 3.2 summarizes the imaging parameters.

Table 3.2. Acquisition Parameters: Billerica, March 1995.

Field of View (mm)	TE (ms)	TR (ms)	Sweep Width (kHz)	Resolution (μm)
8 x 9.2 x 8	0.868	160	125	100 x 115 x 100

Before reconstruction we appended a number of zeros to the time domain data set (FID), a standard procedure known as zero filling [81], increasing the number of

data points to process during the Fourier transform to 128 in each dimension. The reconstructed image required extensive processing, involving application of intensity thresholding and unsharp masking filters. We will discuss the specific details of image processing for three-dimensional data sets and particularly MRI images of foams in Chapter 4. Figure 3.8 shows a three-dimensional surface rendering of the sample, in which round bubbles of varying sizes are visible suspended inside the liquid.

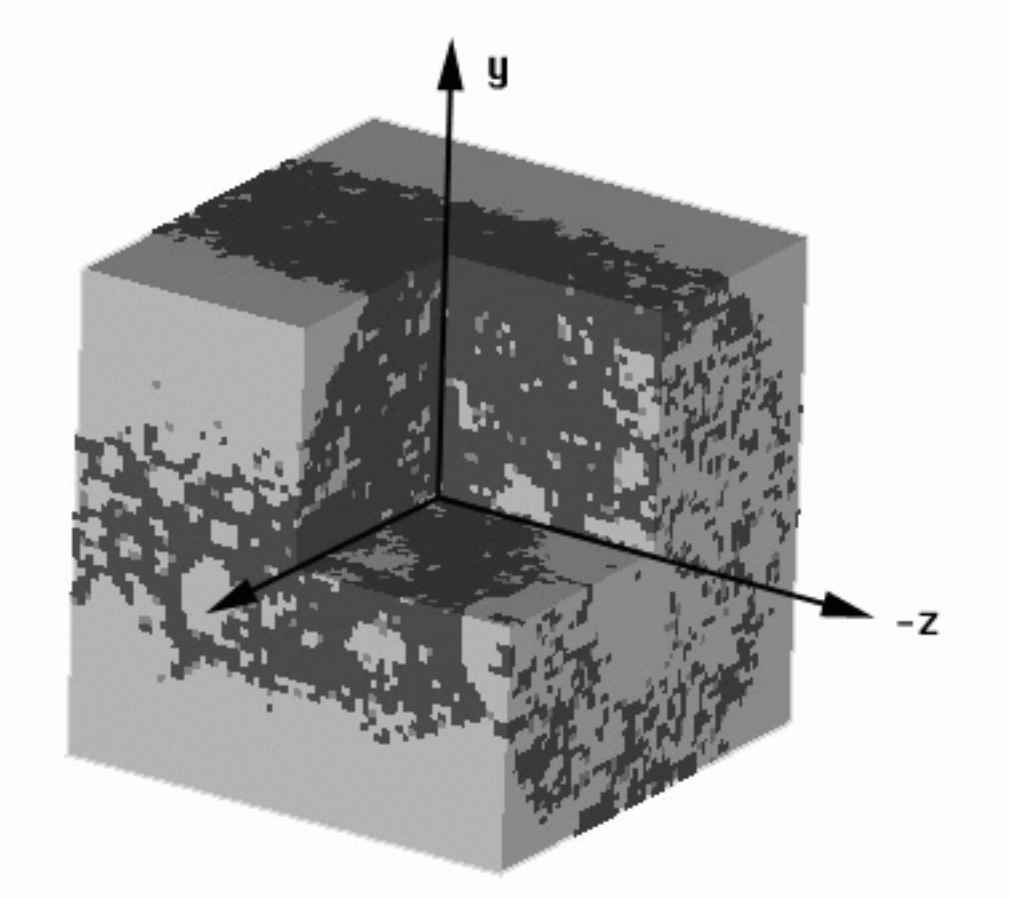

Figure 3.8. Surface Rendering of a Liquid Foam: A three-dimensional MRI image of a liquid foam with high water content. Surface renderings with selective cutouts are the preferred visualization technique, since the high liquid content prevents a ray-traced projection.

The experiment proved that true volumetric imaging of liquid foams was possible, albeit while making high demands on the imaging hardware. The sample was still very wet at the time of imaging, providing a much stronger signal than could be expected in a much dryer foam. The expected low signal intensities in dryer foams, as well as the time constraints faced at the predominantly biomedical imaging facilities that allow outside experimenters (as well as the issue of hardware limitations at these facilities), required the search for a more specialized facility.

The conclusions drawn from the experiments to this point also defined the performance envelope for a dedicated research MRI facility at the University of Notre Dame, which could be optimized for imaging suspensions, particulates, as well as solid and liquid foams.

A suitable high performance imager for high resolution imaging has been operational since the fall of 1995 at the National High Magnetic Field Laboratory (NHMFL) in Tallahassee, FL. This Bruker DMX 600 imager provided an, at the time, unique 14 Tesla (600 MHz) primary magnet with an 89 mm vertical bore, and high performance 96 Gauss/cm gradients. We contacted the NHMFL with a request to use the 600MHz imager to evaluate the effects of high fields on the imaging of liquid foams. Our primary contact was Dr. Steven Gibbs, who raised the issue of worsening susceptibility mismatches in high magnetic fields. An application to perform an evaluation experiment at the facility justified the use of high fields by comparing quantitatively the effects of field strength on polarization density and transverse relaxation time T2. While the signal (polarization density) increases nearly linearly (at room temperature) with field strength, T2 decreases as $T2 \sim \sqrt{f}$ [78].

Subsequently we became the first outside users accepted for an extended trial run at the facility in October 1996.

During our visit at NHMFL we encountered numerous technical problems due to an incomplete imager installation. Particularly, the lack of water cooling for the magnetic gradient coils, missing temperature sensors, and insufficient data storage capacity and acquisition buffers, limited acquisition rates and gradient capabilities, triggering numerous crashes while running experiments.

Despite the technical difficulties, our hypothesis that high fields would achieve superior signal to noise proved right. Figure 3.9 shows an isosurface reconstruction of a liquid foam after about 30 hours of coarsening. Table 3.3 summarizes the acquisition parameters for this experiment. We chose the slow repetition time to prevent the gradient set from overheating in the absence of water cooling and temperature sensors. The foam was considerably more stable, after a switch in the base gelatin brand from Sigma Chemical, to a considerably more expensive Norland Products Hi-Pure brand gelatin. While previous foams would polymerize and break within less than 24 hours, the foams based on Hi-Pure gelatin lasted for over two days.

Table 3.3. Acquisition Parameters: NHMFL, October 1996

Field of View (mm)	TE (ms)	TR (ms)	Sweep Width (kHz)	Resolution (μm)
11 x 11 x 11	2.7	300	125	86 x 86 x 86

In three days of imaging we were not able to obtain a time series of images, due to technical problems. The image we did obtain for a late stage liquid foam was by far the best to date, and proved the viability of our proposal. The results of the evaluation were published in the NHMFL annual report for 1996 [98]. We were encouraged to apply for extended experiment time at the facility for the following summer, following an imager upgrade and component installations.

We received nine days of free experiment time from the NHMFL in July 1997 after a very positive review of our initial work. However, despite software upgrades,

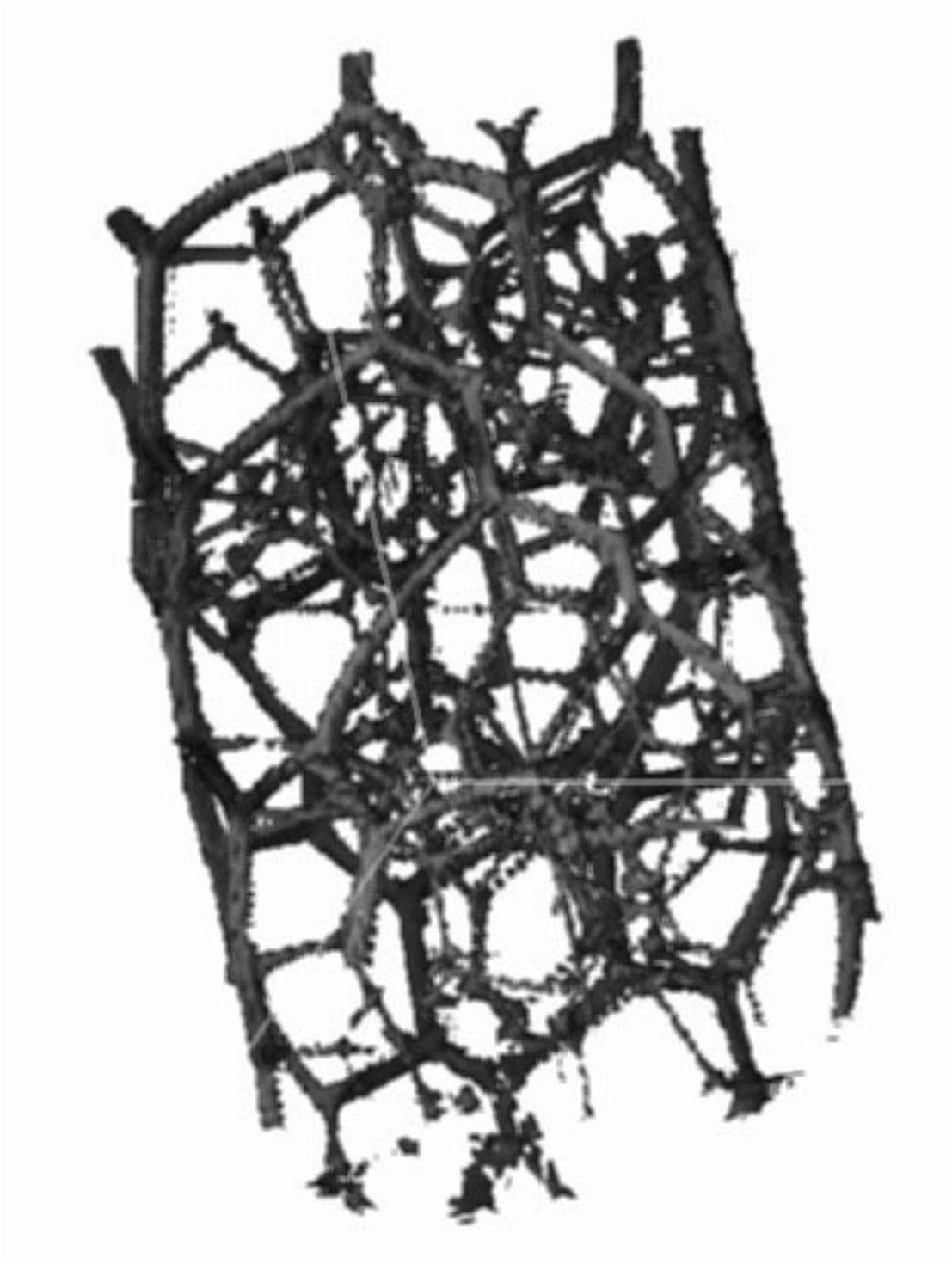

Figure 3.9. Liquid Foams: A ray-traced isosurface rendering of a late stage liquid foam obtained in October 1996. The volumetric image is the first of a liquid foam at very low liquid fraction. The voxel resolution is $86^3 \mu\text{m}^3$, and the image is 11 mm in height.

the imager was even less stable than during our previous visit. We were unable to compile acquisition macros which would have enabled us to automate the acquisitions. Local disk storage was not available. Local network crashes and buffer overflows terminated several acquisitions. We also faced the same technical limitations, including missing temperature sensors and inadequate cooling.

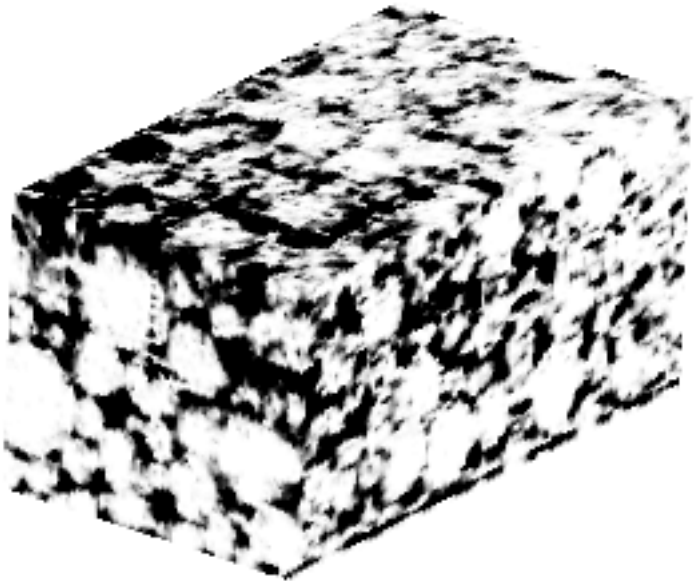

Figure 3.10. Liquid Foams: A surface rendering of an early-stage liquid foam obtained in July 1997.

While trying to overcome the technical problems, we were able to improve the sample's stability and reduce its coarsening rate by actively cooling the sample using a liquid nitrogen evaporator. Several experiments searched for the ideal temperature range, which would not freeze the sample, but keep it in the highly viscous regime just above the freezing transition. Between 279°K and 285°K proved to be a safe

temperature range. During the last three days we were able to slow the coarsening sufficiently to obtain images of liquid foams during early stages of coarsening, at which time the rates of diffusion, drainage and volume changes are faster than in later stages, and image quality depends crucially on the rate of image acquisition. Since we had already succeeded in obtaining high quality images of very dry foams during late stages of coarsening (Figure 3.9), we focussed our attention on early foams, which we needed to master in order to obtain reasonably long time series.

Figure 3.10 shows a surface rendering of a liquid foam that is about two hours old. In comparison to Figure 3.8 the image reveals more detail, but required an acquisition time of 2 hours and 40 minutes for two averages. The sample was kept very near freezing at 278°K during that time, and it subsequently collapsed before we obtained more than a few images.

Overall, the experiment did not provide a usable time series of a liquid foam as we had hoped. Instead it provided us with further insight for the planning of a dedicated imaging facility, and a set of requirements for future experiments:

1. We are able to visualize liquid foams during early and late stages of coarsening.

2. We need to control the coarsening rate of the sample by using temperature control.

3. A robust imager setup with all components fully tested and operational would be absolutely necessary.

4. An MRI facilities requires full-time dedicated staff.

5. None of the MRI facilities we visited (including visits to Bruker and Varian in 1995 and 96 during which we did not image liquid foams) were equipped to handle the large amounts of data (in excess of 20 Gigabytes) required for

serial three-dimensional image acquisitions. Similarly, in order to efficiently transfer large data sets, we required large capacity storage devices, such as writable CD-R, optical media or high capacity tape.

6. A dedicated image processing workstation is necessary to process data sets offline while acquisitions are running, to allow assessment of automated experiments while they are under way, without interfering with the acquisition.

3.2.3 The Notre Dame 300MHz Imager

We submitted an instrumentation funding request to the NSF and secured matching funds from the University of Notre Dame for an MRI facility in February of 1996. The NSF grant was approved in July that year, at which time we contacted Varian, Bruker Instruments, and ChemMagnetics to solicit quotations. These three were the only companies that provide integrated MRI research imagers, including all console hardware, computers, magnet, gradients, probes and software. The high degree of specialization we had in mind for our imager favored buying separate components from specialized manufacturers, and we did look at some components from that point of view. We felt however, that integrating diverse components would require considerable experience and time, and involved risks such as not meeting performance requirements and incompatibilities.

Instrumentation selection involved testing several imagers from all three manufacturers, of which only Bruker was able to provide an imager that very nearly matched our specifications. The Varian imagers we tested (at Palo Alto and Kyoto, Japan) both suffered from thermal problems, due to a lack of water cooling for the gradients and malfunctioning temperature sensors. During a visit to Kyoto we tested a 15cm bore, 300MHz vertical imager which came close to our specifications. However, the Varian pulse sequence libraries did not include three-dimensional imaging

methods. We attempted a standard multi-slice 2DSE sequence on a water filled polyurethane sample, during which the gradient set overheated. Inadequate circuit protection caused one gradient to fail internally, rendering the gradient set useless. We deemed the Varian imagers inadequate to perform the high duty cycle, temperature controlled experiments we designed.

ChemMagnetics provided an interesting 400 MHz imager for our inspection at their facility in Fort Collins. The imager was very stable during testing, and provided a useful, flexible software interface and pulse program library. Water cooled gradients and high powered amplifiers were also available. We tested a liquid foam at a customer site at the University of Wyoming, using a narrow bore 200MHz magnet. The images (without much time for optimization) were very good, and we did not encounter any technical problems. Our imager would have required extensive customization of the rf-probes, which were provided by an independent German manufacturer. We were also concerned about support issues for a project of this size from a very small company, which was reinforced by a somewhat arbitrary and confusing pricing policy, which made it nearly impossible to understand the bottom line, as well as delivery and installation conditions. ChemMagnetics was subsequently purchased by Varian in 1997, and the continuation of their manufacture of high field MRI research imagers was in doubt.

We visited Bruker Instruments twice: in March of 1995 (see previous section), and in October 1996. During both visits we succeeded in imaging our samples. We made velocity measurements of suspension flow (October 96), and imaged liquid and solid foams. During the visit to Rheinstetten, Germany, we tested a 300MHz superwide bore (15cm) imager with water cooled 96 G/cm gradients, a DMX console and Indy workstation running ParaVision 1.0+. The imager performed flawlessly. Equally important, we gained a very positive impression of, and very good working

relationship with, the responsible technical and scientific staff at Bruker, particularly Dr. Mark Mattingly at Billerica, and Dr. Dieter Gross in Germany. We deemed this support to be of crucial importance to the operation of such a complex machine.

Parallel to the selection of a suitable imager, we had to locate and renovate a site for the imaging facility at Notre Dame. Due to changing requirements within the Department of Chemistry, we could not use the location we had originally proposed in the NSF grant. During 1997 and early 1998, we inspected and subsequently dismissed existing locations inside the Radiation Laboratory (the Department of Energy objected), and two locations that were primarily used for storage, which were dismissed due to excessive vibrations and high renovation costs. The construction of a new NMR and MRI facility to house all Notre Dame spectrometers (currently 6) proved too costly as well.

After finding a suitable location within the Department of Physics, we decided in April 1997 to purchase a complete imager from Bruker Instruments, Billerica MA, listed in Table 3.4.

Table 3.4. Notre Dame 300MHz Magnetic Resonance Imaging Facility

Bruker DRX 300 MHz Imager

Primary Magnet	7 Tesla
Proton Resonance	300 MHz
Bore Size	150 mm (Vertical)
Gradients	MINI0.36 at 14.5 G/cm max.
	MICRO2.5 at 100 G/cm max.
Gradients Amplifiers	3 x 40W
Resonators	60mm H_1 for MINI0.36
	2mm, 5mm, 10mm, 15mm, 25mm H_1 for MICRO2.5
Rf- Amplifiers	100W H_1
	300W Broadband

The magnet was assembled and tested in Rheinstetten, Germany by January 1998. During the testing we obtained a first time series of coarsening in a liquid foam.

We were able to further optimize the imaging parameters with the help of Dr. Gross at Bruker (also see Section 3.3.3: Three-Dimensional Imaging Experiments). A very crucial factor for the success of this test was our ability to use high repetition rates (short TR), because for the first time we were able to use water cooled gradients. Figure 3.11 shows two slices from different stages of coarsening inside a foam sample.

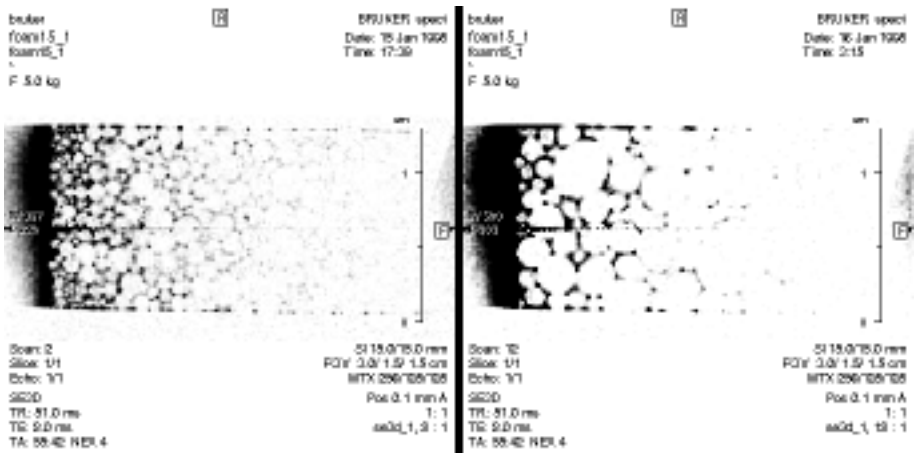

Figure 3.11. Liquid Foams: Two images from our first three-dimensional time series of a liquid foam. The gelatin based liquid was imaged inside a 3 ml plastic syringe of 12mm inner diameter. The liquid content was above 10% during the experiment.

The magnet arrived at Notre Dame in February and was installed in a 5 ft. deep pit to allow for a required 15 ft. ceiling height above the center of the magnet. It was powered up between March 3rd and March 6th 1998, and component testing continued through the middle of April. During that time we replaced an HADC imaging digitizer (maximum bandwidth of 125kHz) with an upgraded HADC-2 (theoretical 1 GHz bandwidth) model. Aside from some difficulties in getting the vibration isolating legs pressurized, and the gradient water cooling to work (leaks, fitting and pressure problems, which explains why water cooling did not work in Florida), the imager met or exceeded all specifications. While we largely used the North American Bruker software distribution, including ParaVision release

1.1.23 [96] with XWINMR 1.2, we also installed some imaging specific source code (IMND class codes) we obtained from Germany, which is more robust and flexible, particularly for SE3D experiments! The facility was operational by the end of April 1998.

3.2.4 Three-Dimensional Imaging Experiments at Notre Dame

After imager installation we began testing the imaging methods provided by Bruker Instruments for US customers, which we keep under the BII acronym in the imaging protocol directories. We obtained a first series of liquid foam images using the BII three-dimensional spin echo sequence. Surprisingly, we were not able to program the short echo times and repetition times we were accustomed to from the earlier tests in Germany. The source code contained too many fixed delays, which we attribute to their design for slow-switching biomedical scanners (which overheat more easily, and which have much larger time constants for the gradients). Accordingly, signal to noise suffered in these first images shown in Figure 3.12, compared to the images we obtained just three months earlier on the same imager (see Figure 3.11). A further bug in the se3d.ppg pulse program prevented averaging multiple acquisitions, which we fixed by eliminating a 180° phase shift in the readout direction, that had effectively canceled consecutive averages.

We encountered other problems with BII protocols, such as the Three-Dimensional Constant Time implementation **SPI**. The easiest solution to the problem was to install the imaging methods provided by Dr. Gross at Bruker in Germany under a separate protocol directory called **Bruker**. While we have not extensively tested many of the protocols provided, the SE3D method that we devised in Germany worked as expected after installation.

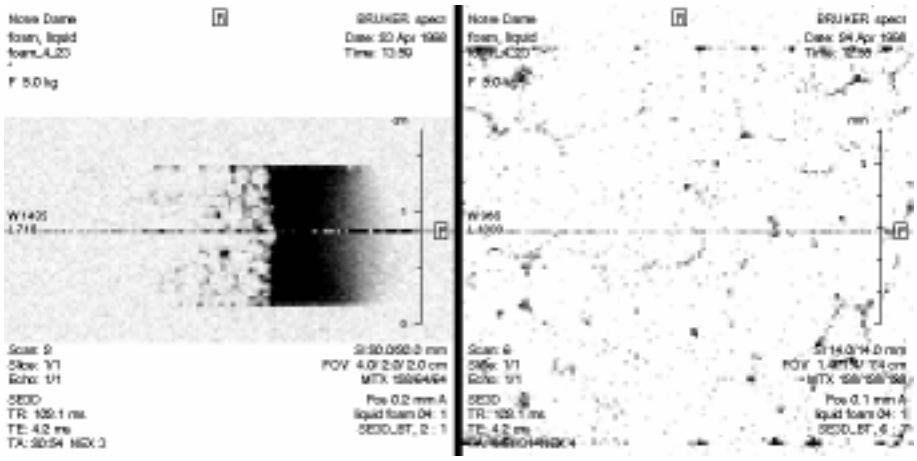

Figure 3.12. Liquid Foams: The first images we obtained in April of 1998 with the 300MHz imager at Notre Dame. Both TE (4.2ms) and TR (150ms) were too long to optimize the S/N, due to the BII IMND source code which prevented shorter echo and repetition times. The gelatin based liquid was imaged inside a 3 ml plastic syringe with 12mm inner diameter.

Between the months of May and July of 1998 we used the imager primarily for biomedical applications, including the imaging of bird brains and clusters of embryonic chicken cells. The experiments tested several performance criteria of the imager, including low flip-angle gradient echo imaging in three dimensions, and high resolution microscopy (see Chapter 2).

During that time we also tested methods of cooling the foam samples, including a liquid nitrogen evaporation/heating system. We repeatedly encountered condensation inside the magnet bore, caused by the temperature of the chilled water used to cool the gradients, and insufficient air conditioning, which to this date fails to provide adequate humidity and temperature control in the MRI facility. Condensation throughout the laboratory caused several shutdowns during the summer months, as excess water had to be removed from insulation materials in the ceiling above the console electronics.

By late July we had established a permanent bore venting system, which provided dry air flow through the bore of the magnet, and prevents condensation under near all operating conditions. We also found that the chilled water supply for the gradients provided sufficient cooling under the tight conditions inside the magnet to effectively maintain a constant temperature (equal to the temperature of the chilled water) in the sample, provided that the sample was already cold when placed in the magnet. This auto-cooling eliminated the problem of having to continuously monitor the nitrogen levels in the evaporator during extended experiments. The evaporator would also regularly freeze, making it a much less reliable means of maintaining a constant temperature for extended periods of time.

Another possible benefit of combining chilled water cooling with a low flow dry air stream, is the prevention of overheating of the rf-transmitter during high power pulsing. The three-dimensional spin-echo sequences require maximum power output in the 25 mm rf-transmitter during the liquid foam experiments, under which the transmission frequencies can experience sudden shifts and jumps [96]. While the absence of such drifts may be due to built in rf-stability rather than efficient cooling, the cooling certainly provided a safety margin here as well.

We resumed imaging of liquid foam samples in July and August, during which time we obtained several moderately good series of images. We were still experimenting with the liquid composition and details of the foam generation at that time, which resulted in several unstable samples. One aspect we tested was both hydrophyllic and hydrophobic coating of the glass container walls, to study the influence of drainage along the walls on the foam's overall stability and wetness. Neither helped stabilize the samples over time, and both actually contributed to early decay of the foam. By preventing the foam from sticking to the side walls of the container, the column essentially collapsed slowly under its own weight, possibly because the

water inside the network had insufficient means to drain (through the "internal" network only), thus contributing to excess weight. Allowing the water to evenly coat the glass walls had an equally disturbing effect, efficiently draining all liquid pockets (the vertices) in the vicinity of the walls. The signal in these parts of the image was severely reduced, and the samples dried out much quicker.

The experiments in July and August succeeded in imaging liquid foams at very high isotropic resolutions, better than 100μm, and at obtaining short time series of twelve to twenty acquisitions each. Figures 3.13 and 3.14 illustrate the progress and changes we made between the data runs in this period. At this point the improvements in the imaging protocol reflected adjustments in field homogeneity, frequency matching, receiver gains and minor protocol changes.

We made significant changes in the experiment preparation and sample geometry that we used until July 1998, shown in Figure 3.13, and the protocol we devised in August 1998, shown in Figure 3.14. The images shown from experiments in January, April and July 1998 all show moderately wet liquid foams with volume liquid fractions above 10%. The foams therefore have some rounded faces, with no distinguishable films separating two adjacent bubbles, close to a suspension where isolated round bubbles "float" in a liquid. Until July we imaged such foams in 10mm NMR tubes, or syringes of equal outer diameter, inside a 10mm rf resonator. The small volume combined with the relatively high liquid fraction had the advantage of producing good signal, but was not sufficiently dry to study polyhedral cells.

In August 1998 we began using 15mm glass tubes and a 15mm birdcage resonator, providing twice the imaging volume of a 10mm resonator, but at the same time requiring doubled rf power output, while losing sensitivity. The switch allowed us to image much dryer foams produced using a millipore air filter placed inside a base liquid reservoir. We connected the glass tube to the reservoir several cen-

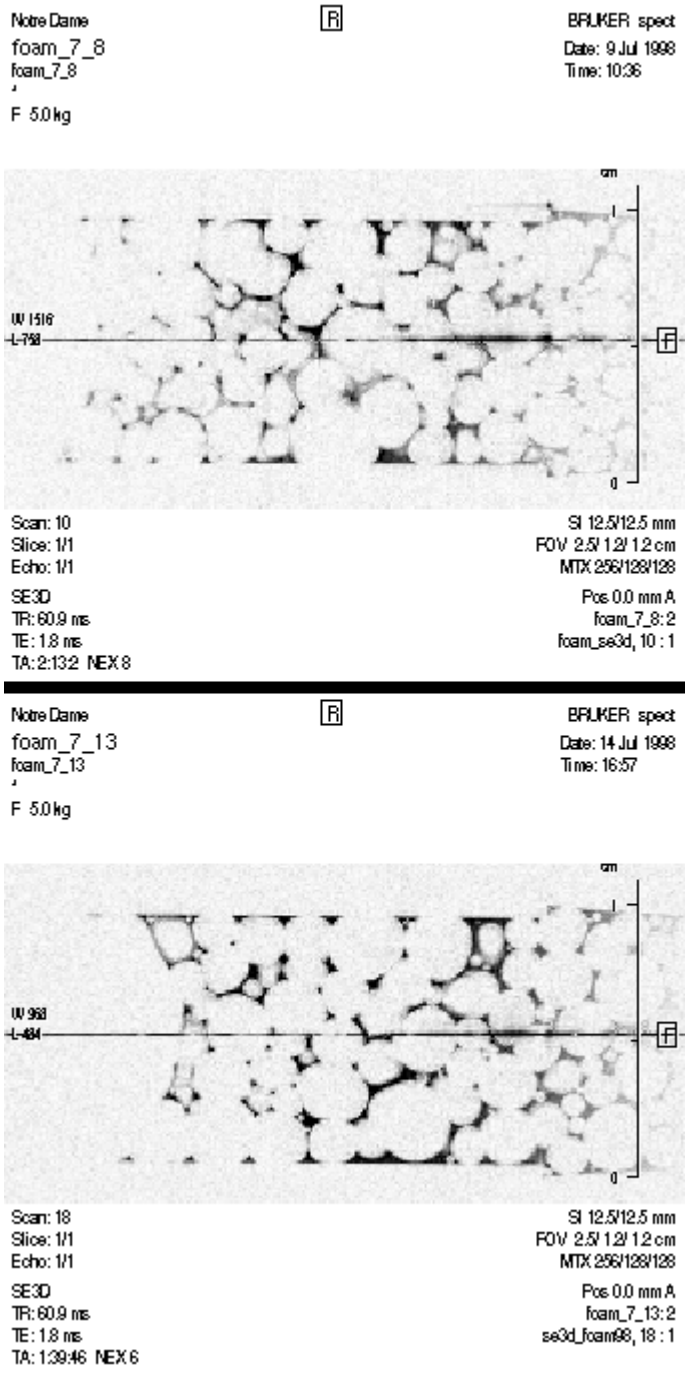

Figure 3.13. Liquid Foams: Two experiments from July 1998. Whipped gelatin foam imaged inside 10mm NMR tubes using a 10mm resonator at isotropic resolution of 93μm.

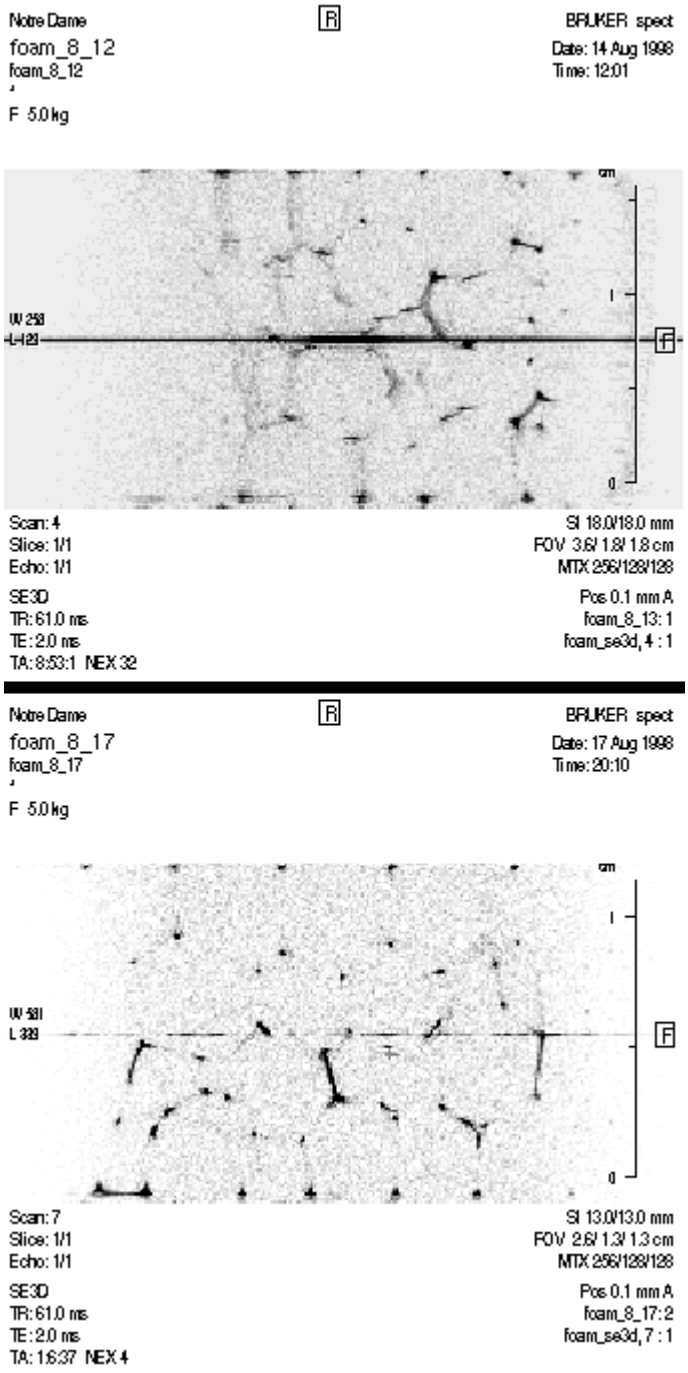

Figure 3.14. Liquid Foams: Two experiments from August 1998. Filtered gelatin foam imaged inside 15mm glass tubes, using a 15mm resonator at isotropic resolution of 101μm.

timeters above the liquid level, so that bubbles that flowed into the glass tube were consistent in wetness and approximately homogeneous in shape (with about a 10% variation in diameter). The imaging protocol was able to pick up good signal from these samples.

We decided to retain this setup, and shorten the repetition time even further, by lowering T1 to about 30 ms (using a 16 mM concentration of $CuSO_4$). We obtained the first usable extended time series of a liquid foam between September 18 and September 21, 1998 (foam_9_18). We used the imaging parameters in this acquisition for all further experiments, and stored them in the 15mm pulse program protocol directory as "foam_se3d" and "foam_98". Figures 3.15 and 3.16 show slices from three time steps of this experiment, and a ray traced maximum intensity projection of the foam at about 48 hours.

Table 3.5. Summary of Acquisition Parameters

	foam10_16	foam1_21	foam2_02
Imaging Method	SE3D	SE3D	SE3D
Pulse Program	se3d.ppg	se3d.ppg	se3d.ppg
Nucleus	H	H	H
Acquired Data Points	256 x 128^2	256 x 128^2	256 x 128^2
Spectral Width (Hz)	125000	125000	125000
Isotropic Voxel Size (μm^3)	101^3	141^3	141^3
Echo Time TE (ms)	2.0	1.9	1.9
Repetition Time TR (ms)	50	50	50
Homospoil	0.1ms	0.1ms	0.1ms
Dummy Scans	1.0s	1.0s	1.0s
Pulse Shape	bp	bp	bp
Excitation Pulse Length	19.5μs	25μs	25μs
Refocusing Pulse Length	39μs	50μs	50μs
Transmitter Attenuation	+1.0 dB	+5dB	+5dB
Receiver Gain	595-2000%	720-4500%	890-6300 %
Averages	4 to 8	2 to 12	2 to 16
Acquisition Time/Ave. (min)	13:40	13:40	13:40

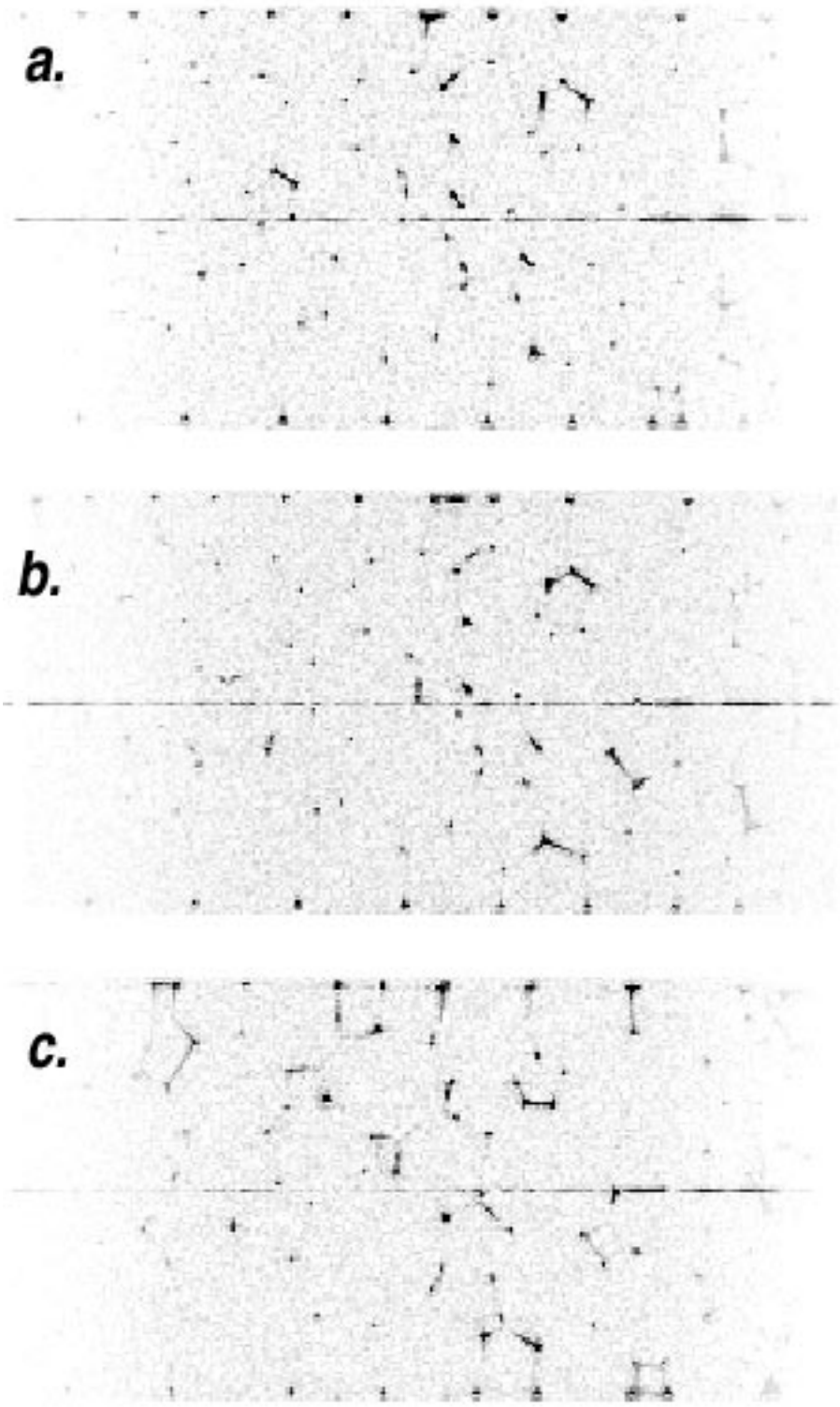

Figure 3.15. Liquid Foams: Slices from three images of the first extended time series obtained in September 1998 (foam_9_18). Filtered gelatin foam imaged inside 15mm glass tubes, using a 15mm resonator at isotropic resolution of 101μm. The sample diameter is 12mm. The imaging parameters are summarized in Table 3.5.

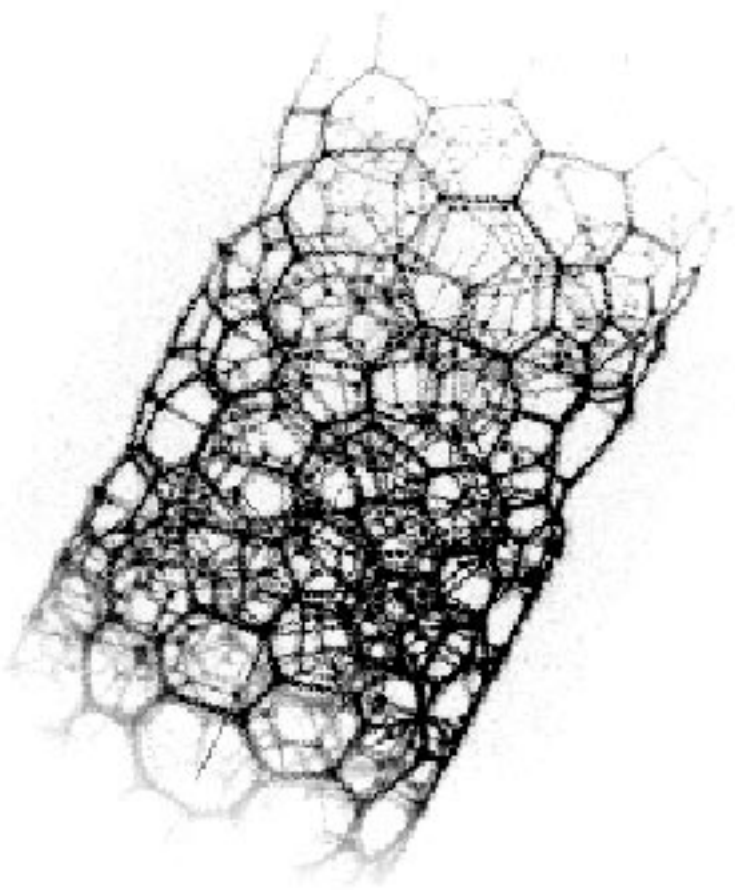

Figure 3.16. Three-Dimensional Rendering: A maximum intensity projection of the MRI image of foam_9_18 after two days of coarsening, showing the three-dimensional structure of the sample. The sample diameter is 12mm. The imaging parameters are summarized in Table 3.5

Subsequently we collected one more data run using the "filtered" foam and 15mm resonator setup on October 16, 1998 (foam_10_16). We used the same protocol to conduct two more experiments (foam_1_21 and foam_2_02) using a 20mm glass tube and 25mm resonator. We "whipped" these foams to produce smaller bubbles, which we let dry to a liquid fraction of less than 10% before placing the foam in the tubes. Using a larger tube and smaller bubbles enabled us to study the foam for longer periods of time, allowing us to study larger volume changes. The disadvantage is a further reduction in signal intensity, which required a doubling of the rf power output. Table 3.5 summarizes the acquisition parameters for the last three experiments. We will present a full analysis of these experiments in the following chapters.

A single image acquisition average during the experiments took about 14 minutes. To improve the signal to noise ratio, initial scans employed two averages, extended to four and later eight, as the sample drained. Thus a "snapshot" of the foams took 30 minutes initially (for about 24 hours) and 120 minutes at the end of the runs. We took data for both relatively homogeneous (filter method) and polydisperse (whipping method) foams in 15mm and 25mm rf-coils. The experiments each lasted for several days, during which we acquired forty or more images of the foams as they evolved. We automated the actual acquisitions through an acquisition macro, which is a UNIX shellscript that invokes a series of ParaVision specific commands [96]. Approximately every four to six acquisitions we had to adjust the base frequency (due to magnet drift) and receiver gains. Gradient and bore temperature remained constant throughout the experiments. Typically the gradients would reach a stable working temperature of 310°K. Table 3.6 summarizes the experiments.

Figure 3.17 shows three-dimensional, maximum intensity reconstructions of a dry, initially homogeneous foam at different stages of development.

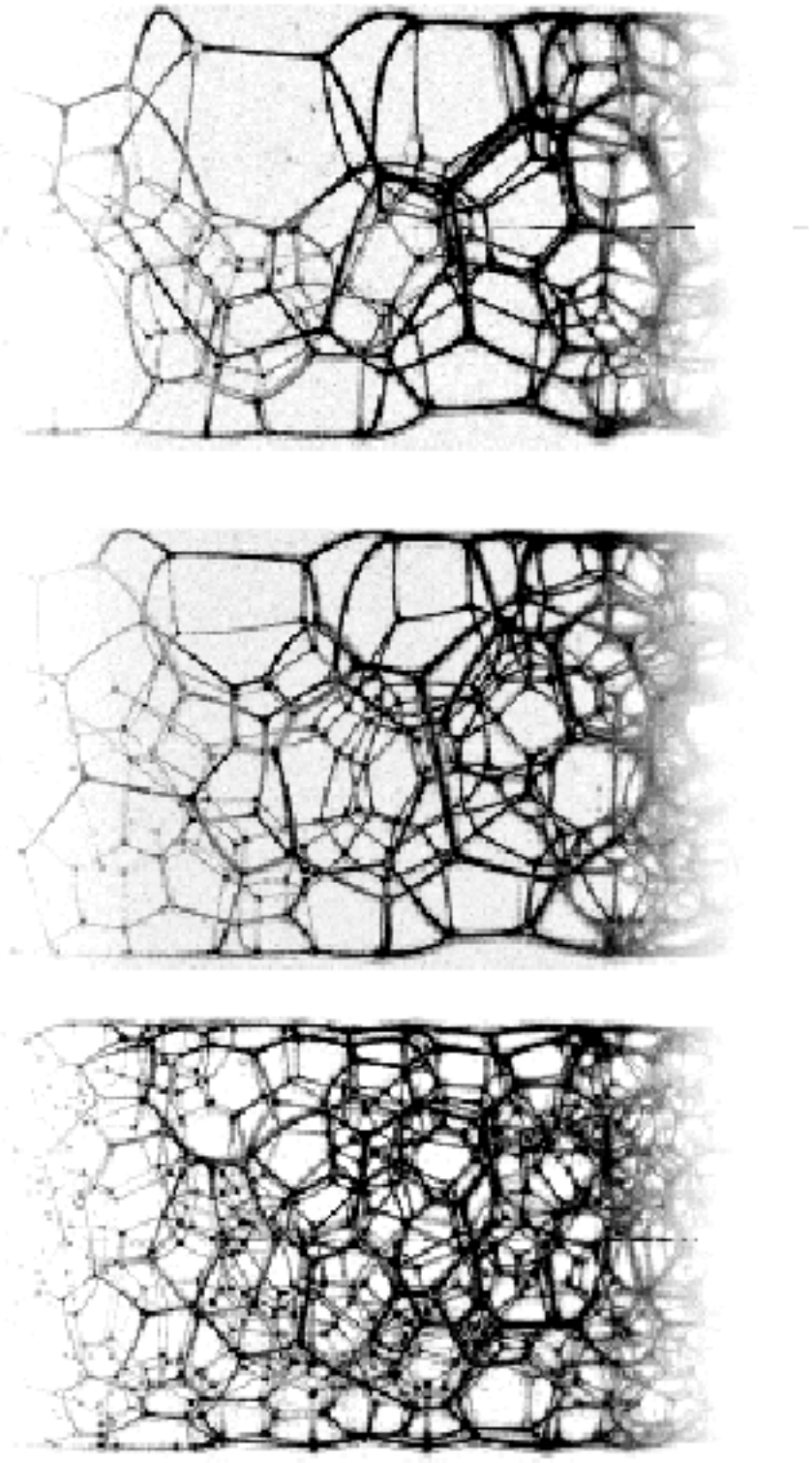

Figure 3.17. Maximum Intensity Projections of Three-Dimensional MRI Reconstructions. The foam is shown at three stages of development: a = 12 hrs, b = 28 hrs, c = 48 hrs. The sample diameter is 12 mm. See Tables 3.5 and 3.6 for acquisition and experimental details.

Table 3.6. Experiment Summary

	foam10_16	foam1_21	foam2_02
Dates	10.16.98	1.21.99	2.02.99
	to 10.19.98	to 1.24.99	to 2.07.99
Foam Type	Filtered	Whipped	Whipped
Sample dia. x length (mm)	15 x 30	20 x 40	20 x 40
Initial Bubble Sizes	2.0 $\pm$ 0.3mm	30 - 300μm	30 - 300μm
Sample Temperature (°K)	282	281	281
Wetness after 4 hrs.	$< 2.0\%$	$\sim$10.0%	$\sim 10.0\%$
Wetness during imaging	$< 2.0\%$	<2.0%	$< 2.0\%$
Imaging Method	SE3D	SE3D	SE3D
Acquisition Time (min)	13:40	13:40	13:40
Number of Data Runs	59	40	52
Runs Analyzed	48	28	39

CHAPTER 4

DATA ANALYSIS

4.1 Background

Visualizing and analyzing three-dimensional data, particularly spatially complex structures or paths, are notoriously difficult. Most visual inspection of data is restricted to two dimensions, such as a display on a computer screen or charts on paper. Many tools exist to create quasi three-dimensional representations of multivariate data. Geological and meteorological sciences use three-dimensional isosurface charts to represent, for example, height variations, wind speeds and water distributions [14]. Color coding in conjunction with isosurfaces can contain additional information, or add clarity.

Advances in computer processing over the last ten to fifteen years have added the ability to represent such data at oblique angles, showing the third dimension in surface charts more intuitively [14, 99].

Such methods cannot easily represent more complex structural data to be readily understood by the human eye. Projections from a single perspective will hide features from view. Three-dimensional renderings of the layout of organs or blood vessels, distributions of underground deposits or aquifers, the complex three-dimensional wind pattern in a cyclone, or a true appreciation of the layout of the Carlsberg Caverns, cannot be understood by the human eye without providing additional information [95, 100].

Stereoscopic displays can address these shortcomings to some extent [101], while the most widely used method to visualize complex three-dimensional structures, is data animation [95]. A three-dimensional data set can be rendered from a variety of viewing perspectives, either from within or outside of the data set. By displaying closely spaced perspectives in rapid succession, the data become animated, revealing features from many different perspectives. In conjunction with stereoscopic rendering, this technique of visualization has become the state of the art in displaying, for example, complex protein structures, or machine parts in the final stages of design [102, 101].

We can render images of three-dimensional foams in the same way, allowing the eye to inspect and combine information about the structure from many perspectives. While this step in data analysis is the most interesting visually – giving direct proof that the complete three-dimensional structure has indeed been captured – it is only a first necessary step to extract precise structural information.

While many images readily reveal the object of interest – such as a tumor in a three-dimensional body scan, or a crack revealed by x-ray inspection of a work piece, – the structure of individual bubbles, their sizes and shapes, can not be directly inferred from the three-dimensional foam images. These contain secondary information, specifically the location of water concentrations inside the Plateau borders (the vertices and edges of the bubbles). Our areas of interest are investigating the three-dimensional growth law, and the shapes of individual bubbles, requiring extensive data processing, partially using established techniques and available software, in part using new programs.

The first section of this chapter focuses on three-dimensional image processing, vital to preparing the data for further analysis. The rest of the chapter describes how we extract information about the bubbles themselves from these images. We

have developed two independent techniques that have specific advantages in determining bubble structure, but only automated reconstruction can address coarsening dynamics in a reasonably efficient manner, without undue amounts of manual labor.

4.2 Image Processing

4.2.1 Introduction

The term image processing according to John C. Russ [95] describes two processes: One which improves the visual appearance of images to the human viewer, and one which measures images for structures and features present. In many cases accepted and widely used techniques are available for both purposes, and, as is the case with MRI images of foams, visual improvements are a necessary step before accurate feature extraction becomes possible. An advanced reference for two- and three-dimensional image processing techniques is *The Image Processing Handbook* [95], written by Russ.

The majority of image processing done today is on two-dimensional photographs, or sections (slices) of an object of interest. Radiologists use multiple MRI or CAT sections through a region of interest, to approximately understand the three-dimensional extent of features. Drafters have had to rely on representing three-dimensional objects with orthogonal planes on a two-dimensional space. With the development of powerful drafting software and computers this limitation has decreased over the last decade, and a workpiece can now be represented by as many sections in the third dimension as there are picture elements along the axes of the plane. Such rendering allows visual inspection of workpieces, and even functional analyses before they are built. Geological and archaeological exploration take advantage of the same development, allowing precise localization of findings (visualized

with sound, X-rays or NMR), thereby saving cost and limiting environmental impact.

If the resolution along all three axes matches reasonably well, and if consecutive sections have no spacing or overlap, a data set consisting of multiple sections forms a *volumetric image*. Ideally a volumetric image contains isotropic picture elements, called voxels, in which the extensions along all three orthogonal axes are equal (the voxel is a cube). This voxel length is the *isotropic linear resolution*. The MRI images we obtained of liquid foams are isotropic, volumetric images, with voxel resolutions between 101μm and 147μm. The x,y,z extension of a voxel is the smallest observable size object in a given data set.

Reaching back to the early days of black and white film photography, many ways have been found to manipulate two-dimensional images, to reveal or enhance otherwise hidden features, or to eliminate distortions or low contrast effects [95]. Before the advent of computerized processing this was achieved by using color pass filters and out of focus, over- or under-exposure of the print positives. In the age of digital image processing this same process involves gradient or averaging operations applied to pixels and their neighbors, histogramming, thresholding and banding, as well as selective alterations of individual colors or color tables.

While a three-dimensional image is fundamentally a series of two-dimensional images, we cannot treat it as such when dealing with techniques to lower or eliminate random or systematic noise. Three-dimensional structures can easily be distorted, connections eliminated or created when simply applying two-dimensional image filters to individual sections of an image. Figure 4.1 shows a two-dimensional section from a three-dimensional data set. Visible are two types of noise. Uncorrelated *white* noise appears as random *buckshot* throughout the section. Radio-frequency

leakage from the high powered rf-transmitter creates a *center artifact*, which appears as a broadening spike along the center of the $\hat{x}$-axis in the image.

As discussed in Chapter 3, the very small volume which houses the water makes standard calculations of signal to noise ratios meaningless. We therefore cannot use thresholding, which simply suppresses signal below a certain intensity, to eliminate low intensity noise completely, without eliminating some parts of the structure (mostly in edges at or near the midpoint between two vertices, where the amount of signal producing liquid is smallest). We need a more complicated approach, which at first reduces both random noise and artifacts, then an erosion/dilation "closing" operator fills gaps in the structure that could have been created by the noise reduction, or that could have been present because the signal within an edge location was not sufficient to be distinguishable during the discrete Fourier transform.

4.2.2 Regions of Interest

We acquired all data with twice as many voxels along the vertical axis as within the perpendicular plane. This geometry was dictated by the rf-coil geometries, which have a resonator length of approximately 40 mm, with diameters of 15 and 25 mm respectively. Water accumulation near the bottom, and very dry foam boundaries near the top of the resonator volume produce less signal than the foam near the center, where the excitation pulse is optimized. Also the rf-artifact is much broader inside the liquid rich area near the bottom, wide enough to mask existing structural features. Near the top, the signal from the liquid in the boundaries becomes increasingly discontinuous, which makes it impossible to reconstruct complete boundaries in this region, without masking too many small features throughout the data set. Closing a gap of three voxels across would also possibly eliminate bubbles or faces less than six voxels in diameter.

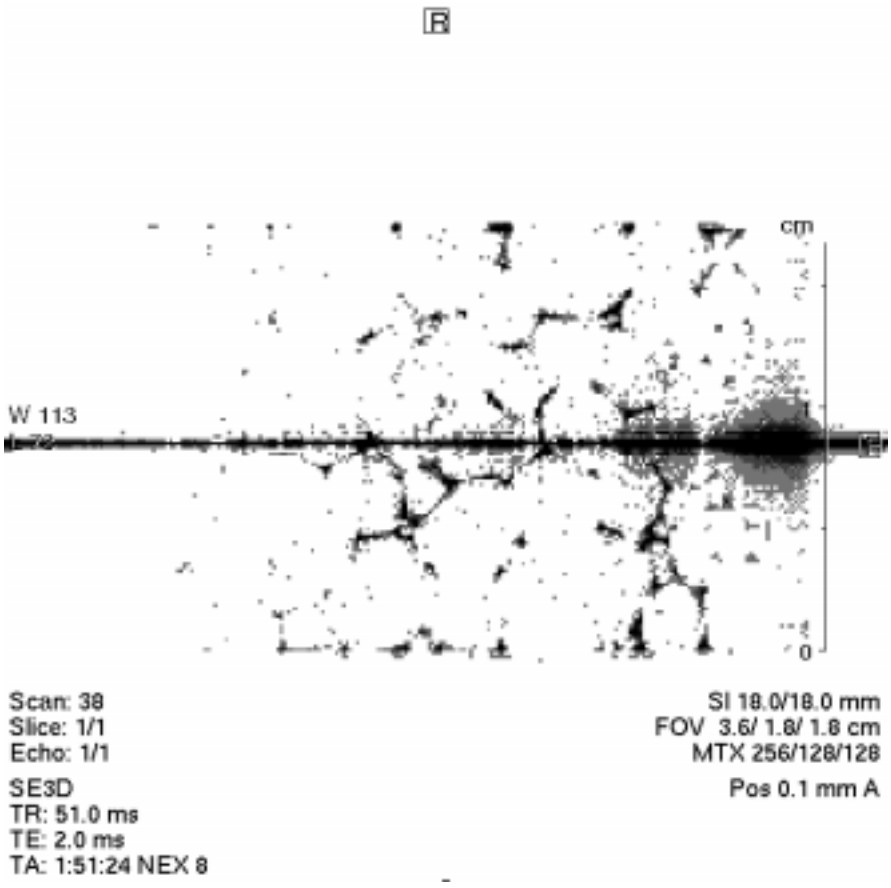

Figure 4.1. Slice From a Three-Dimensional Data Set (foam2-02 run 38): "Buckshot" noise, as well as a strong center artifact, appear clearly in the image, along with parts of real water signal from the liquid in the sample.

We must therefore truncate the data sets at the top and bottom. Also, since the samples are never perfectly centered within the field of view, and the field of view closely corresponds to the sample size, some aliasing occurs (typically, in the analyzed data runs, about three to six voxels at one edge each in the $\hat{x}$ and $\hat{y}$ directions). Due to these limitations, we concentrated our analysis on a region of 120^3 voxels at the center of the original data sets. This truncation of data is common in MRI images, and often done in the reconstruction. We chose to reconstruct the full images first, and perform the truncation during the early stages of analysis. This sequence allowed us to inspect the full images at later times (which is less sensitive to low signal or noise than most processing algorithms). All remaining image processing and data analysis used the extracted cubes of 120^3, or 1,728,000 voxels.

4.2.3 Artifact Elimination

Radio frequency noise leaking from the rf-amplifier and at the transmitter connections, where the transmitted and received signal pass through in short succession [74], creates rf-artifacts. In MRI images rf-artifacts commonly appear as zero offset frequency lines at the centers, referred to as *zippers* along the phase encode axes. Zipper artifacts are usually strong when high rf-power is required, or when the switching time between signal transmission and reception is very short.

The 90° pulses used in the spin echo imaging of liquid foams require near full power from the 100 Watt rf-transmitter. This high power in conjunction with the very short T2, which requires rapid signal acquisition after the rf-pulse is emitted, contributes to the very prominent zipper artifact seen along the center of Figure 4.1. Another similar zipper structure is present along the plane perpendicular to the slice, which is the second phase encode direction during the three-dimensional acquisition.

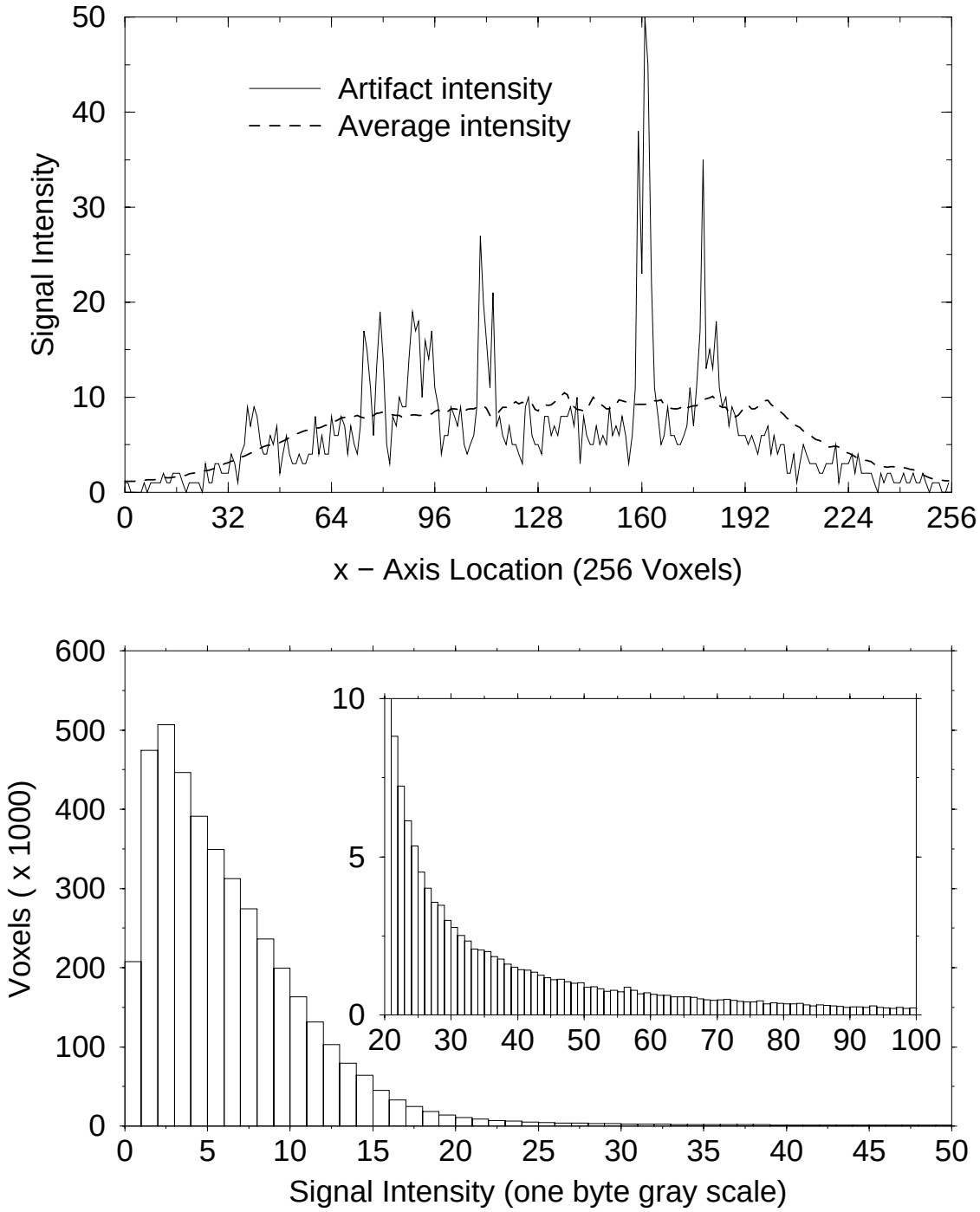

Figure 4.2. Spatial and Intensity Distributions (foam-10-16 run 28): Top: Comparison of signal intensities inside and outside the center artifact. Bottom: Histogram of intensity distributions in the entire data set. The inset extends the intensity scale to show the small number of voxels with intensities above 50.

Figure 4.2 shows the signal intensities within the artifact along the $\hat{x}$-axis in the top graph. The shape of the distribution resembles the averaged intensity distribution of non-artifact signal voxels along $\hat{x}$, measured for the entire sample. The averaged values for non-artifact voxels at times exceeds the artifact intensities. Overall the signal intensities in the artifact are nearly centered within the range of values obtained from true foam signal. The bottom graph in Figure 4.2 shows a histogram distribution of signal intensities in the whole sample. Measurements of single background voxels in this particular data run confirm that the upper threshold for random noise is at a signal intensity of about 20. While some signal from liquid or artifact has intensities below 20, all signal with intensities above 20 is due to liquid or an artifact. Since the intensity ranges for signal and noise overlap, band suppression or thresholding will not eliminate random or artifact noise.

0	**1**	**0**	**15**	**2**	**0**	**0**
2	**0**	**1**	**26**	**3**	**1**	*18*
1	**2**	**0**	**45**	**1**	*26*	**0**
13	**35**	**55**	**87**	**49**	*64*	**22**
0	**2**	**0**	**34**	**0**	*25*	**2**
3	**0**	**1**	**27**	**1**	**0**	*29*
0	**2**	**1**	**14**	**2**	**0**	**0**

0	**1**	**0**	**1**	**2**	**0**	**0**
2	**0**	**1**	**2**	**3**	**1**	*18*
1	**2**	**0**	**1**	**1**	*26*	**0**
1	**2**	**0**	**0**	**1**	*26*	**1**
0	**2**	**0**	**0**	**0**	*25*	**2**
3	**0**	**1**	**1**	**1**	**0**	*29*
0	**2**	**1**	**2**	**2**	**0**	**0**

Figure 4.3. Neighborhood Ranking: Values along the center row and column are replaced by the average of their two nearest neighbors in the same row or column. The center value is replaced by the average of its four *diagonal* neighbors. The light-gray colored pixels on the left, indicating true signal, are left unchanged.

Hence an algorithm to eliminate the artifacts has to work along the known center voxel locations (technically the zipper is centered about the N/2+1 voxel for N phase encode steps), along two axes of the data. Since the zipper represents no

real structure, we can replace its value by the average value of neighboring voxels. This procedure is usually part of NMR acquisition software toolkits, and is included as an application with ParaVision[96]. The supplied algorithm eliminates zipper artifacts only along a single axis, and averages only the two nearest neighbors of a one voxel wide artifact. Due to the high rf-power and short echo times during our 3DSE acquisitions the artifacts in the foam images are up to 7 voxels wide (see Figure 4.1). We designed a more flexible and powerful algorithm, that could adapt to the varying sizes of the artifacts.

Figure 4.3 shows a schematic 7 x 7 voxel cross section of an artifact at the center of an image on the left side. The voxel values represent signal intensity. The gray cross shaped voxels at the center highlight the extent of the artifact (high signal), which for illustration purposes is seven voxels wide. Typically the artifact ranges from three to seven voxels in width. The light gray voxels on the right side of the left figure contain real signal from the foam structure, which we need to leave unchanged. In Figure 4.3 each element inside the dark gray area is replaced by a simple average of its two closest neighbors. The right side shows the area after the averaging filter has been applied. With the exception of the voxel connecting two signal containing elements, the values inside the originally gray area are now equal to or lower than their surrounding noise.

The geometry of artifacts in real three-dimensional MRI is considerably more complex, and even in this example, the voxel at the very center actually had to be replaced by the average of its four diagonal neighbors. Typically it is sufficient to examine the shape of the artifact for one early and one late data run in an experiment, and record its maximum extensions and shape. We can choose a number of two- and three-dimensional neighborhood ranking filters to best eliminate all artifact noise. The strongest artifacts occur in experiments using the 25 mm rf coil,

and +5 dB transmitter attenuation. Best results are achieved by a three-dimensional ranking filter, which combines first and second nearest neighbor averages with the third nearest neighbors inside the two-dimensional plane, and weights each value by its distance to the voxel that is replaced.

The cross shape of the artifact extends up to three voxels from the center in each direction, and is sometimes three voxels wide. So we must first process any non-center columns of the artifact, to avoid averaging elements that are part of the artifact to replace other artifact voxels. Figure 4.4b shows the result of this region selective replacement operation for experiment foam-10-16, in which the artifact from Figure 4.4a has been removed, without otherwise altering the image. Figure 4.5 shows a second case for experiment foam-2-02. The artifact is significantly wider and signal to noise is only half as good as in foam10-16 (corresponding to the ratios of the imaged volumes). The artifact elimination algorithm works just as well in this case.

4.2.4 Removing Uncorrelated Noise

Figure 4.1 shows the large amount of uncorrelated noise present in the data sets, often referred to as *buckshot* noise from the way it produces featureless random spots on the image. The intensity of this noise compared to the intensity of real signal in MRI usually scales as Signal/Noise $\sim N/\sqrt{N}$ for N averages [74]. Most data acquisitions during foam experiments use two or four averages, with very late stages of development often requiring eight or twelve.

While the above $\sqrt{N}$ relation between signal and noise is reasonably accurate in a static tissue or in a fluid filled environment, the signal intensity during foam imaging changes (decreases) constantly during image acquisitions, due to drainage (changing liquid content for each voxel), and line broadening caused by changes in

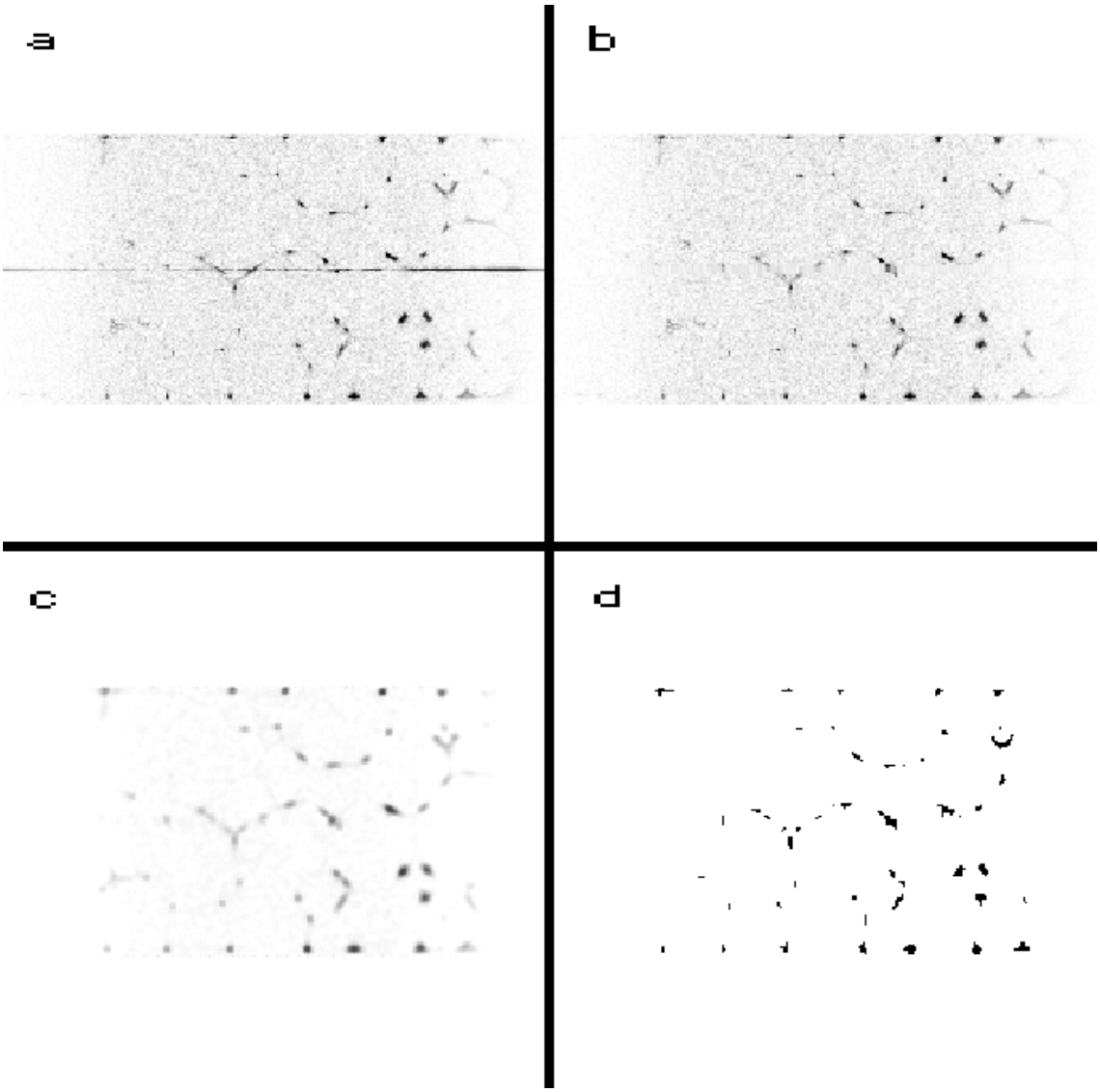

Figure 4.4. Processed Image (foam10-16 run 28): a) Raw image with a one voxel wide artifact and random noise. b) The slice after artifact removal. c) After median filtering and thresholding. d) Binary image, with all non-zero voxels set to gray scale value 255. A worm algorithm removed all remaining non-connected voxels from the image.

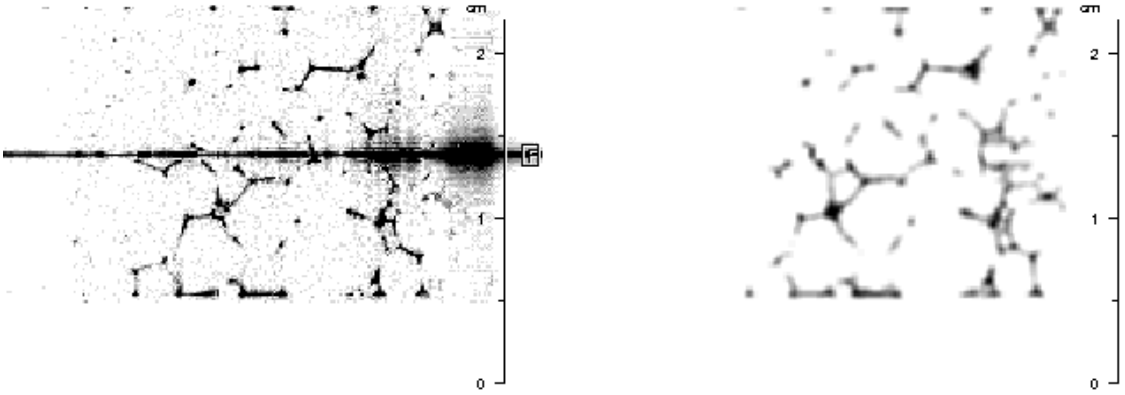

Figure 4.5. Processed Image (foam2-02 run 38): Left) The data set artifact extends over 9 pixels in some areas, with strong random noise. Right) The same image after processing to remove random noise and artifacts. The foam structure has not been altered in the process.

interfacial areas. Adjustment in pulse power and rf-frequencies during the experiment change the signal intensities for each image, while, other than due to minor thermal fluctuations, the level of noise usually stays constant for any single average and throughout the experiment.

Eliminating or significantly reducing random noise is desirable for two reasons:

One: to enhance images for visual inspection. The presence of significant buckshot noise when viewing a volumetric rendering obscures structure at deeper levels of the image.

Two: to aid in further computerized image processing, which will eventually require a noise free image, and to aid in visually based tracing of structures, by reducing chances of misinterpreting signal.

We have already cut areas of the image in which larger gaps exist within the generally continuous foam structure (see Section 4.2.2), and where liquid accumulations generate significantly stronger signal. This selection simplifies the noise reduction process. Two general observations about the three-dimensional liquid foam images are relevant:

1. Voxels which contain actual signal do not occur in isolation. The liquid is really continuous.

2. Gaps in the structure tend to be small, so that in a disconnected edge, each edge point and "gap" has at least one direct neighbor that also contains signal.

The continuous nature of the signal we are trying to preserve allows us to use a neighborhood ranking filter to reduce the intensity values of isolated noise voxels to those of their surroundings [95]. Figure 4.7 shows the application of a stepped 5 x 5 mask. The median value of all voxels contained in the defined neighborhood replaces the center voxel of the gray region. This operation is linear, and preserves all information of the original image [95]. The mask is then shifted by one voxel at a time and applied again. We allow for only parts of it to be used near the image boundaries. We can refine this process to include weighted ranking, whereby nearer elements are given stronger weighting (in which case the mask consists of a

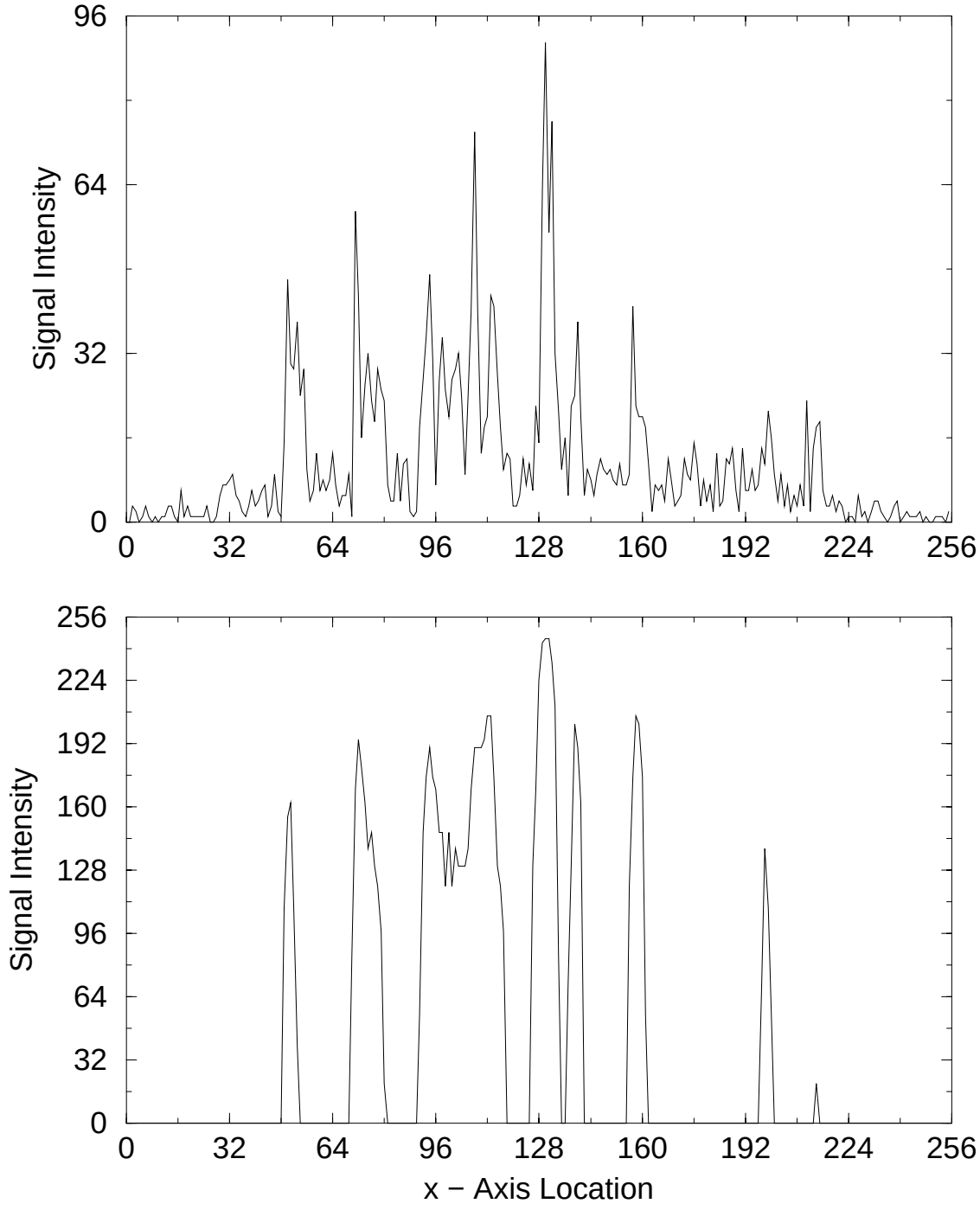

Figure 4.6. Histo-Equalization: Intensity values of a single data row are scaled, histo-equalized, binned and thresholded to improve signal to noise.

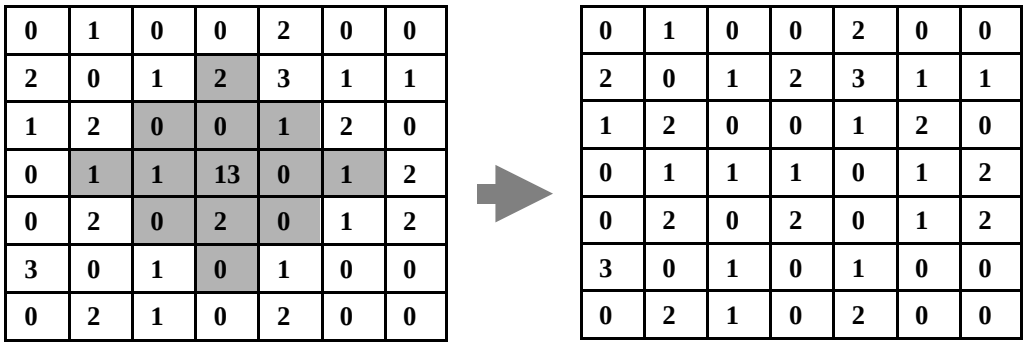

Figure 4.7. Effect of a Median Filter: A stepped 5 x 5 neighborhood shown in gray is chosen around a voxel. The median value of the surrounding gray area replaces the center voxel of this region.

set of points, each of which has a corresponding multiplication factor). A three-dimensional 5 x 5 x 5 mask with differential weighting sweeps the foam data sets, effectively reducing random noise to background level. The weighting insures that voxels which have one or more nearest neighbors containing true signal, and which contain signal themselves, receive a new value that is above the background values.

A median filter with a minimal extension of three voxels along each axis, considering nearest neighbors with factor three, second nearest with factor two multiplication and so on, produces the result shown in Figure 4.4c). In this image, we first applied the median filter, and then used a low threshold of gray scale value 6 to set most residual background to zero. Finally we linearly expand the dynamic range of the image by scaling the gray-scale values to the maximum allowed value (for an eight bit binary image this is $2^8 = 256$), which is referred to as *histo-equalization*. Figure 4.6 shows the effect of these operations on a single row of signal values along the x-axis. The top graph shows the raw data intensities corresponding to the noisy image in Figure 4.4. The bottom graph shows the same intensity profile after all filtering operations. The peaks correspond to liquid accumulations in vertices

that intersect the row, while the broader regions stem from edges. At this stage almost all noise has been eliminated, and only a few disconnected "noise regions" remain, which originally contained several noise pixels, and which the filters could not distinguish from vertex or edge signal.

4.2.5 Dilation and Erosion

Morphological operations collectively describe an extensive class of image processing operations [103]. These operations include erosion and dilation, as well as combinations of these. A morphological *closing operator* fills a missing pixel within features, or a gap between portions of a feature, and consists of successive applications of dilation and erosion processes [95].

The operations involve value replacements for each voxel in the original image, using the original pattern and a set of replacement rules. Similar to other neighborhood filters, we define a neighborhood volume around a center voxel. The simplest erosion application would then replace the center voxel value with a zero, if any one voxel in the neighborhood is zero. This operation is shown in Figure 4.8. We first evaluate a nearest neighbor region around each voxel in the original image. If a zero is present, the center value is replaced. Otherwise it remains. The net result is the erosion of an existing boundary by a single layer of pixels.

The opposite of erosion is dilation, which expands boundaries of features. The morphological closing operation performs both dilation and erosion. It uses a neighborhood kernel to dilate feature boundaries, and then applies the same kernel to perform erosion. The net result is that gaps or holes in the structure that are smaller than the applied kernel fill or close, while existing boundaries remain otherwise unchanged [95]. The IDL programming environment [104] provides sufficiently

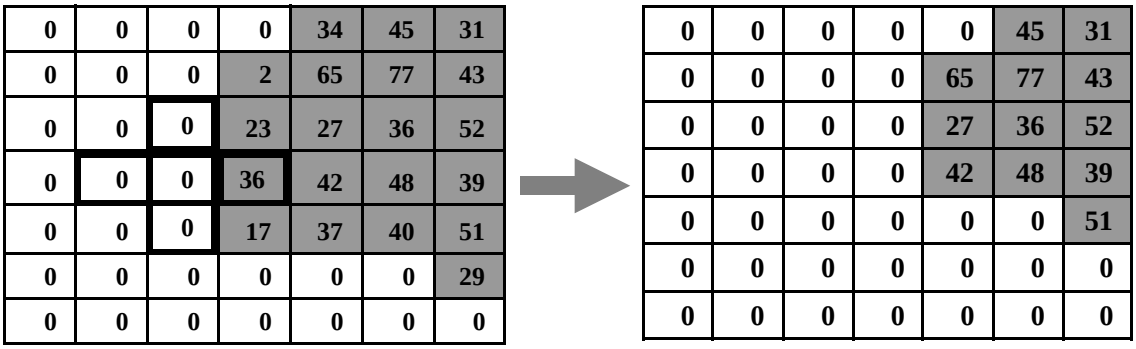

Figure 4.8. The Erosion Operation: A simple nearest neighbor kernel around each pixel replaces the pixel value with zero only if one element inside the kernel is zero. The result is shown on the right.

flexible compiled erosion and dilation routines, which we use in all erosion/dilation operations on foam data sets.

The foam data sets contain some very small bubbles, so that the closing operation would almost certainly destroy some structure. We have to weigh this disadvantage against the advantage of gaining complete liquid edges, aiding in the reconstruction of bubble volumes and shapes.

Figures 4.9 and 4.10 show the same data set before and after application of the above image enhancement techniques. While the processed, non-animated three-dimensional image in Figure 4.10 looks "flat" to the eye (histo-equalization and binning erases contrast), the absence of misleading false structures and noise, as well as the closure of gaps in the signal distinguish it from the raw image.

4.2.6 Connected Regions: Creating a Binary Image

Any remaining noise has become insignificant for rendering or optical analysis of the data sets. However, computer analysis of foam structure requires a complete elimination of these remaining regions, to avoid false distance mapping and topological reconstructions.

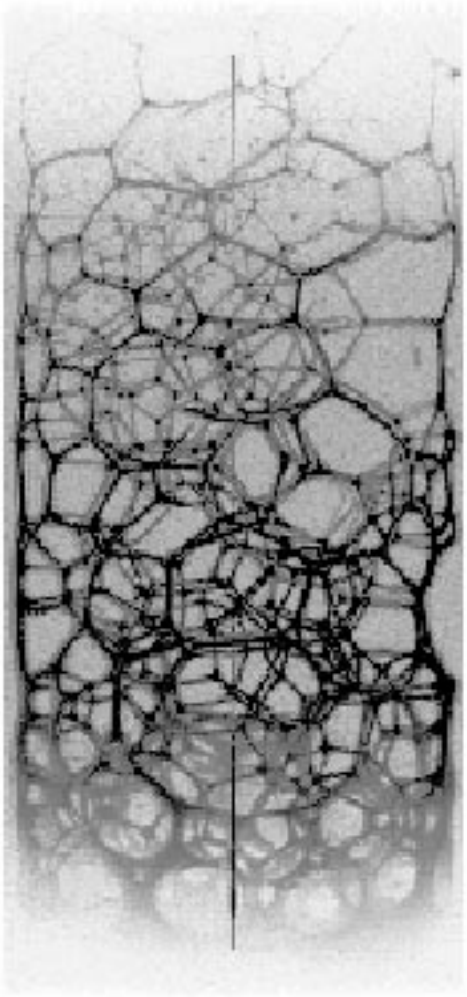

Figure 4.9. Three-Dimensional Maximum Intensity Projection (foam-10-16 run 28).

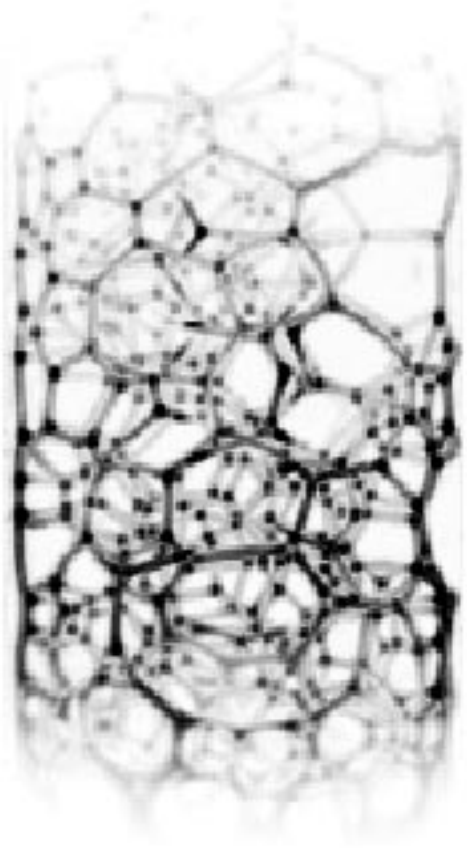

Figure 4.10. Processed Data: The same data run as in Figure 4.9 after artifact elimination, noise reduction, smoothing and histo-equalization. Gaps have been closed using the morphological closing operation.

For this last step, we transform the image into a binary format, in which all non-signal voxels contain a zero, while signal voxels are set to one. Figure 4.6 shows the near binary nature of the image after histo-equalization, with most background voxels already set at zero. We need to determine a threshold for the values which will be set to one instead of zero. The purpose of this processing step is to create a network consisting of only ones to replace the original signal data points. This creates an unambiguous data set, in which all signal is represented by the same number, and which helps processing intensive algorithms to perform more efficiently. We do not require an exact correspondence, so long as the binary network closely resembles the previous structure. A rough estimate of the number of voxels which should contain signal (*i.e.*, ϕ, the liquid fraction) is sufficient. If our threshold produces a higher voxel percentage than we expect from the liquid fraction, we choose a lower threshold. This matching also serves to check (somewhat intuitively), if the parameters chosen in earlier processing steps were successful. If too few voxels scale as signal, either in absolute terms, or in comparison with previously processed data sets from the same experiment, we can adjust any of the processing steps to produce consistent results.

Algorithms that search a data set to find connected regions are referred to as snake, or worm operations [102]. The operation performed on the foam data requires the identification of a single voxel location, whose connectedness with the rest of the lattice is to be investigated. We select a signal containing voxel near the center of the data set (the program simply grabs a voxel of value one from a list). A 3^3 kernel is placed around the voxel, and the values of all non-zero neighbors are recorded in a list. The kernel is moved to the first neighbor in the list, and its neighbors are evaluated. All non-zero locations are again added to the list, while a separate list is kept of locations that have been evaluated. The two lists are sorted and compared

after each step. When both lists have become equal, there are no more non-zero voxels in the lattice that are connected to the original location. On rare occasions the initial voxel is not actually part of the liquid network, but one of the few remaining noise elements. In that case the list of connected neighbors is extremely short, and the program simply chooses another voxel. The list of connected voxels is usually 99% or more of the number of voxels containing ones in the original binary image. This means that less than 1% of voxels in the binary image contained disconnected noise.

A new image lattice can be created, in which the locations of all connected non-zero voxels are input as ones, while the rest remain at zero. This image will be absolutely free of uncorrelated noise. Figure 4.4d) shows this final result of the image processing on a single slice. The total lack of differentiating contrast makes the binary image of a three-dimensional foam utterly uninteresting to look at without some kind of animation.

For further image processing we write the lists of connected voxels for each data set into binary files. The lists usually contain between 20,000 and 60,000 connected voxels.

4.3 Geometric Analysis

4.3.1 Hand Tracing and Hull Construction

A somewhat labor intensive method concentrates on the exact semi-manual reconstruction of individual bubble shapes. Kose [52] and Monnereau [41] previously used similar manual reconstruction techniques.

We have already processed the images to eliminate artifacts and random clusters of noise. We now cut the data run into slices, each one pixel deep, which corresponds to the natural resolution limit. The images show signal along all intersections of

bubble faces (edges). Scanning through the slices, we identify any point at which such edges converge as a vertex and record its location. While scanning process for vertices might at some point be automated, we have not yet solved some fundamental problems with this approach. Vertices generally consist of identifiable clusters, which a scanning program would be able to identify. However, the inhomogeneous nature of our samples, local changes in wetness (thus varying sizes of liquid accumulations) and signal inhomogeneities conspire against such an approach. Manual identification is tedious but safe.

We process the lists of three-dimensional vertices, shown for a single bubble in Figure 4.11a), that belong to each bubble using a triangulation algorithm. The so-called Quick Hull (qhull) algorithm [105] which we used is available for free from the University of Minnesota Geometry Center. It is useful in generating connecting hyper-planes in a large variety of degenerate and non-degenerate geometric problems. We use it here to create a list of simplical (triangular) facets, shown in Figure 4.11b, that constitute the smallest convex hull around the set of vertices for a bubble, shown in Figure 4.11c.

From this list we calculate the approximate bubble volumes. We then merge the facets to create non-simplical faces. The merging algorithm uses the direction of the normals of each facet's hyper-plane as an initial merging criterion. For a bubble with a finite number of sides, the normals for adjacent faces must have identifiably different directions. We use a very safe initial merging threshold of 10°, allowing for 36 faces to exist within each possible cutting plane of a bubble. After merging we calculate the topological charge χ of the resulting bubble:

$$\sum_f n_f * (n_f - 6) = \chi, \tag{4.1}$$

where n_f is the number of edges for each face *f*. If the topological charge χ is -12, we have only four-fold vertices outlining the bubble. If it is greater than -12 we have degenerate vertices, and we increase the merging angle by increments of 0.5°, up to a maximum of 20°. Conversely, if the charge is less than -12 we lower the merging angle. The exact hull is "joggled" this way, until we find the correct charge, or reach a maximum angle. Figure 4.11d shows the result of this step, in which case 36 triangular facets have merged into an irregular dodecahedron.

The method involves a selection bias towards four-fold junctions, which are under mathematically ideal conditions (*i.e.* a perfectly dry foam) the only stable junctions [32]. Non-ideal foams, which have finite radii of curvature at the junctions can have degenerate vertices at which more than four edges meet. Indeed, about 10% of the bubbles we processed this way did not reach a non-zero topological charge before the maximum merging angle was reached. Especially for large, multi-sided bubbles, in which adjacent faces have small separation angles between their plane normals, the joggling possibly caused distinct faces to merge. However, the number of bubbles containing more than about twenty-five faces is very small. So while not quantifiable (due to the non-regular geometry of the bubbles), the selection bias will probably not have a noticeable effect on the calculation of numbers of faces and edges per side.

This method allows us to investigate the detailed shapes of interior bubbles, and it is limited only by the cumbersome procedure of tracing all vertices in the sample.

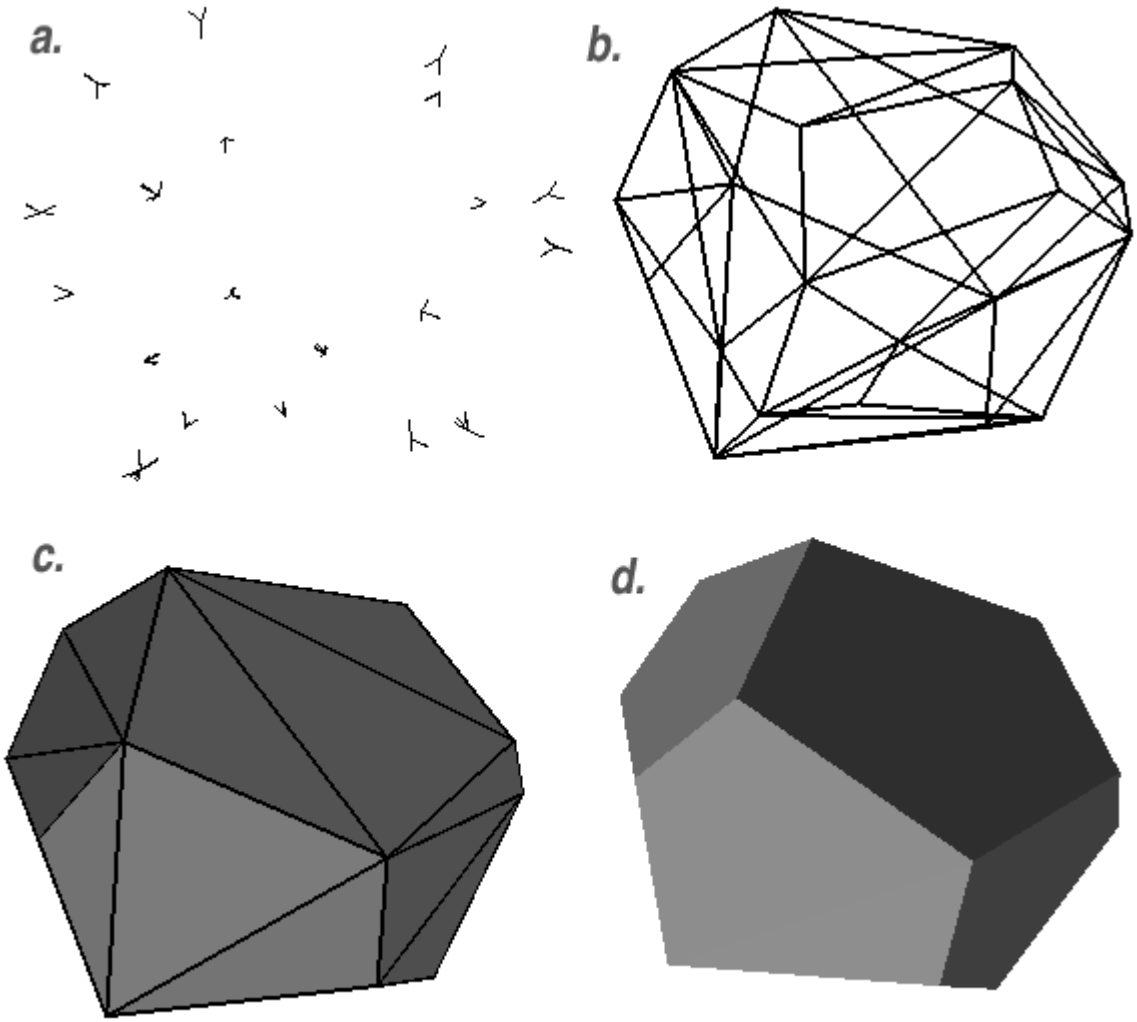

Figure 4.11. Simplical Reconstruction: a) Vertices marking the shape of a single bubble. b) Triangulation of the minimal surface connecting the vertices. c) Simplical hull spanning the triangular surfaces. d) Non-simplical faces, created by merging near parallel hyper-planes.

4.3.2 Distance Maps and Delauney Triangulation

We developed a second method to eliminate the manual identification of vertices. We first processed the reconstructed three-dimensional images to remove all imaging artifacts and random noise.

We used the list of connected voxels to create a Euclidean distance map of the lattice as shown in Fig. 4.13. A distance map of a data array finds the minimum Euclidean distance, $r_{min} = (x - x_i)^2 + (y - y_i)^2 + (z - z_i)^2$, from each voxel to the nearest voxel that contains signal. If the array is free of noise, *i.e.* no arbitrarily located voxels contain signal that is not part of a truly existing structure, a Euclidean distance map will have local maxima at points that are the farthest removed from any boundary (signal), within any empty volume that is contained by boundaries.

Next we group localized clusters of local maxima into single centers using a third nearest neighbor scan. This grouping is required due to the non-spherical nature of the domains. Figure 4.13 shows the nature of a distance map for polygonal bubbles. Ridges converge into a cluster that, depending on the shape of the domain may contain more than one local maximum, or a group of voxels with equal values. We group the maxima in descending order of magnitude. We then select the first maximum in the list, and record all maxima that are closer to its location (Euclidean distance) than that maximum's value (its *neighborhood*. All maxima in this neighborhood are then removed from the scan for further bubble centers.

This process also eliminates spurious maxima that can occur at the centers of bubble faces by requiring a zero overlap between the zones of influence of all pairs of maxima, imposing the geometric constraint that the diameters of adjacent bubbles are larger than that of their joining face. We use a three-dimensional Delauney triangulation [106, 107] from the center locations to compute neighbors for each center. The averaged radius of the equivalent sphere for each center n_c is estimated

as the mean of the distances d_i to all its neighbors n_i, each divided by $(1 + V_i/V_c)$, where V_c and V_i are the Euclidean distance map values for the center and each neighbor. Finally, we discard bubbles in contact with an outside wall or the edge of the image.

We could thus track individual bubbles over time, identifying bubbles that did not change their number of faces between consecutive images. For each time step we compared the centers to those in the previous image and determined the most probable pairings according to center location, volume and number of faces.

The number of bubbles which do not change their number of sides between two consecutive data runs is very small. Figure 4.12 shows the number of bubbles found for each data run in the three analyzed experiments. While the slopes are meaningless, due to different time intervals between acquisitions, the number of bubbles identified between consecutive acquisitions decreases dramatically. In foam-2-02, the number of identified bubbles between the first and last acquisition is reduced by nearly a factor of ten. While this reduction is good from the perspective of studying a long period of growth, it also means that between two consecutive data acquisitions, a sizeable fraction of bubbles disappear. Since all direct neighbors of these bubbles will change their topology at least once, they will not be counted. So while during 36 analyzed acquisitions in experiment foam-2-02, we identify a total of 4799 bubbles, only 879 bubbles (mostly at later times) remained at constant topology between two acquisitions. All three experiments have between 15% and 20% of bubbles that remain at constant topology for at least two consecutive acquisitions.

While both methods for analyzing the data have limitations and some potential for error, they represent the only technique we know to date, to extract the information we seek from the data sets we have obtained. We present our results

in the following chapter, together with a discussion on the status of the current experimental method, and future possibilities.

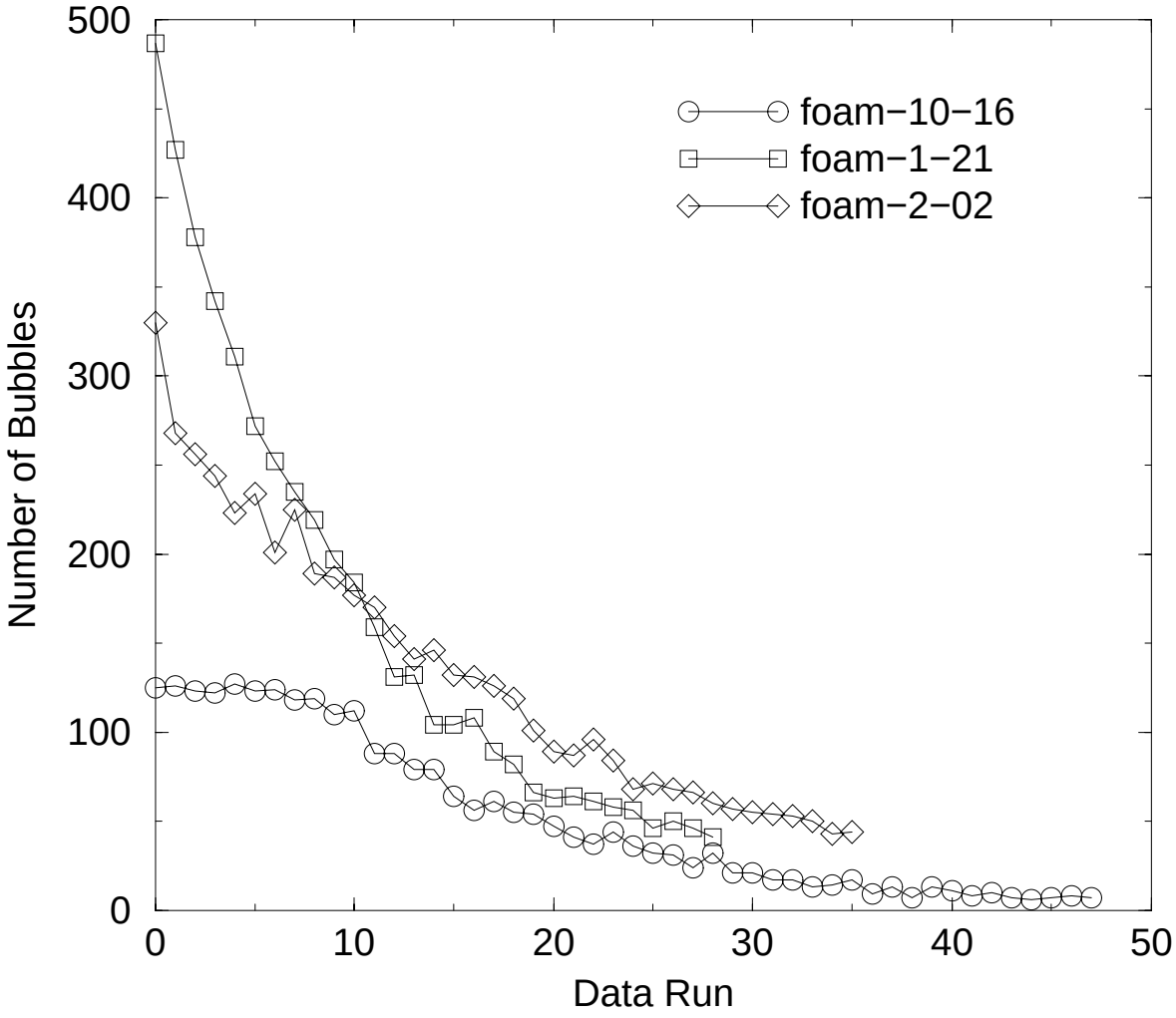

Figure 4.12. Numbers of Bubbles in Each Experiment: A significant fraction of bubbles disappears between consecutive acquisitions (data runs), changing the topologies of all their neighboring bubbles.

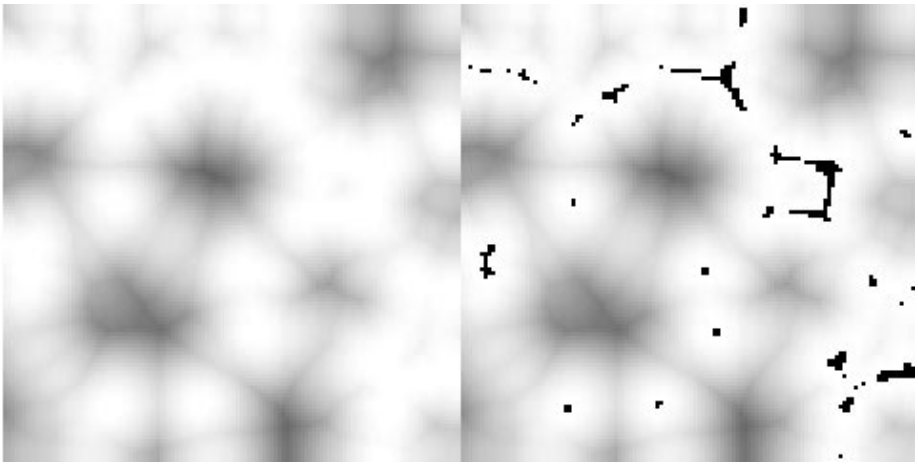

Figure 4.13. Euclidean Distance Map: Left) Slice of a three-dimensional Euclidean distance map. Right) The same map superposed on the corresponding raw image slice in a late stage foam. Darker pixels are farther from the nearest fluid edge.

CHAPTER 5

RESULTS AND CONCLUSIONS

5.1 Bubble Structure

We used hand-tracing and hull reconstruction to investigate the shapes and sizes of about 350 bubbles in experiment foam-2-02. Tracing the thousands of bubbles in all data runs for a single experiment would require many months (possibly years) of manual work. Instead, we concentrated on identifying all bubbles within the center of the sample in a set of five individual data runs. Thus for individual data runs, we could extract all relevant topological distributions: The numbers of edges for all faces, the numbers of faces for all bubbles, and the volumes for all bubbles. Figure 5.3 shows the distributions of volumes, edges and faces for data run 32 from experiment foam-2-02, at which time the foam has coarsened for about 28 hours. Figure 5.1 shows the relative locations and varying sizes of some fifteen reconstructed bubbles (out of 97 measured) from this data run. The picture illustrates the strong variations both in sizes (note the small tetrahedral shape attached to a larger bubble in the lower left) and shapes that we are able to reconstruct using this method.

In the introduction we stated that Glazier [38] found that in simulations the averaged volume rate of change for a group of bubbles with f sides depends only on its number of sides

$$\langle \mathrm{V}_f \rangle^{-1/3} \langle \frac{\mathrm{dV}_f}{\mathrm{dt}} \rangle = k(f - f_0), \tag{5.1}$$

which implies that, on average, bubbles with f greater than f_0 will grow, while bubbles with a smaller number of faces will shrink (see Section 1.5.2 for more details). From this, Weaire and Glazier deduced for the relation between f and f_0 [39]:

$$f_0 = \langle f \rangle \left(1 + \frac{\mu_2}{\langle f \rangle^2} \right), \tag{5.2}$$

where $\mu_2 = \langle f^2 \rangle - \langle f \rangle^2$ measures the disorder of the foam. Eqn. 5.2 is exact provided that the average volume of a bubble with f faces scales as $\langle V_f \rangle \propto f^3$, which was true in Glazier's Potts model simulations.

Using the data shown in Figure 5.3a), for $\langle V_f \rangle \propto f^\alpha$ we found $\alpha = 2.7 \pm 0.4$, which is consistent with Glazier's simulations. Using equation 5.2 we found the zero growth value $f_0 = 16.3 \pm 0.7$, and an average number of faces $\langle f \rangle = 12.3 \pm 0.6$. The average number of edges per face is $\langle n \rangle = 5.1 \pm 0.4$.

Our zero growth value $f_0 = 16.3 \pm 0.7$ is consistent with the value $f_0 = 15.8 \pm 0.1$ obtained by Glazier [38]. The average number of faces $\langle f \rangle = 12.3 \pm 0.6$ is slightly lower than values reported by Glazier ($\langle f \rangle = 14.08 \pm 0.02$), Matzke [50, 51] ($\langle f \rangle = 13.7$), Kose [52] ($\langle f \rangle = 13.6$) and Monnereau [41, 53] ($\langle f \rangle = 13.4$). Foams consisting of ideal Kelvin ($\langle f \rangle = 14$) or Weaire-Phelan ($\langle f \rangle = 13.5$) partitions also require slightly larger $\langle f \rangle$. The average number of edges $\langle n \rangle = 5.1 \pm 0.4$ per face agrees with the values found by Matzke, Kose and Monnereau. Also the number of five-sided faces was larger than for any other number of sides (see Figure 5.3c), similar to Matzke's finding. However the ratios of five- to six-, and five- to four-sided faces are significantly smaller than those found by Matzke. Monnereau also reported finding predominantly five-sided faces, but failed to give exact ratios.

A possible explanation is the distribution of bubble sizes in the foam we studied. The volumes in this data set range from 36 voxels^3, all the way to several tens of thousands of voxels^3, a range of three decades. We found several small bubbles

which possessed exclusively three-sided faces, such as the regular tetrahedron shown in Figure 5.2. At the same time some of the largest bubbles had many six and seven-sided faces. Hence a more monodisperse foam should possess relatively more five-sided faces, as Matzke found.

The large range of bubble sizes also explains the relatively low value we find for the average number of faces $\langle V_f \rangle$. Figure 5.3a) shows the relation between bubble volume and number of faces. We find that 22% of small internal (not in contact with a wall) bubbles have four or six sides, a geometry not reported by any other investigator. Few very large bubbles exist with 20 or more faces on the other hand. The statistical average $\langle V_f \rangle$ then can be expected to be lower than for less polydisperse samples studied by Matzke, Kose and Monnereau.

Table 5.1 summarizes the distributions of edges and faces, and their averages, for the two proposed minimal area partitions and the various experimental results.

Table 5.1. Geometry of Space Filling Polyhedra

	Ratio of edges (3:4:5:6:7)	Ratio of faces 12:13:14:15)	Ave. number of faces	Ave. number of sides
Kelvin [49]	0:43:0:57:0	0:0:100:0	14	5.14
Weaire-Phelan [29]	0:0:89:11:0	25:0:75:0	13.5	5.11
Matzke [50, 51]	0:11:67:22:0	12:30:36:18	13.7	5.11
Kose [52]	-:9:70:21:-	13:38:25:25	13.6	5.12
Monnereau [41, 53]	-	-	13.4	5.11
Glazier [38]	–	–	14.1	–
This study	5:27:40:22:6	10:7:9:5	12.3	5.1

We recorded the number of faces and the number of edges per face for all bubbles. We then scanned the individual records to see if any Kelvin or Weaire-Phelan structures would emerge. Neither complete structures were found, however, we found several irregular pentagonal dodecahedra. These pentagonal dodecahedra are part

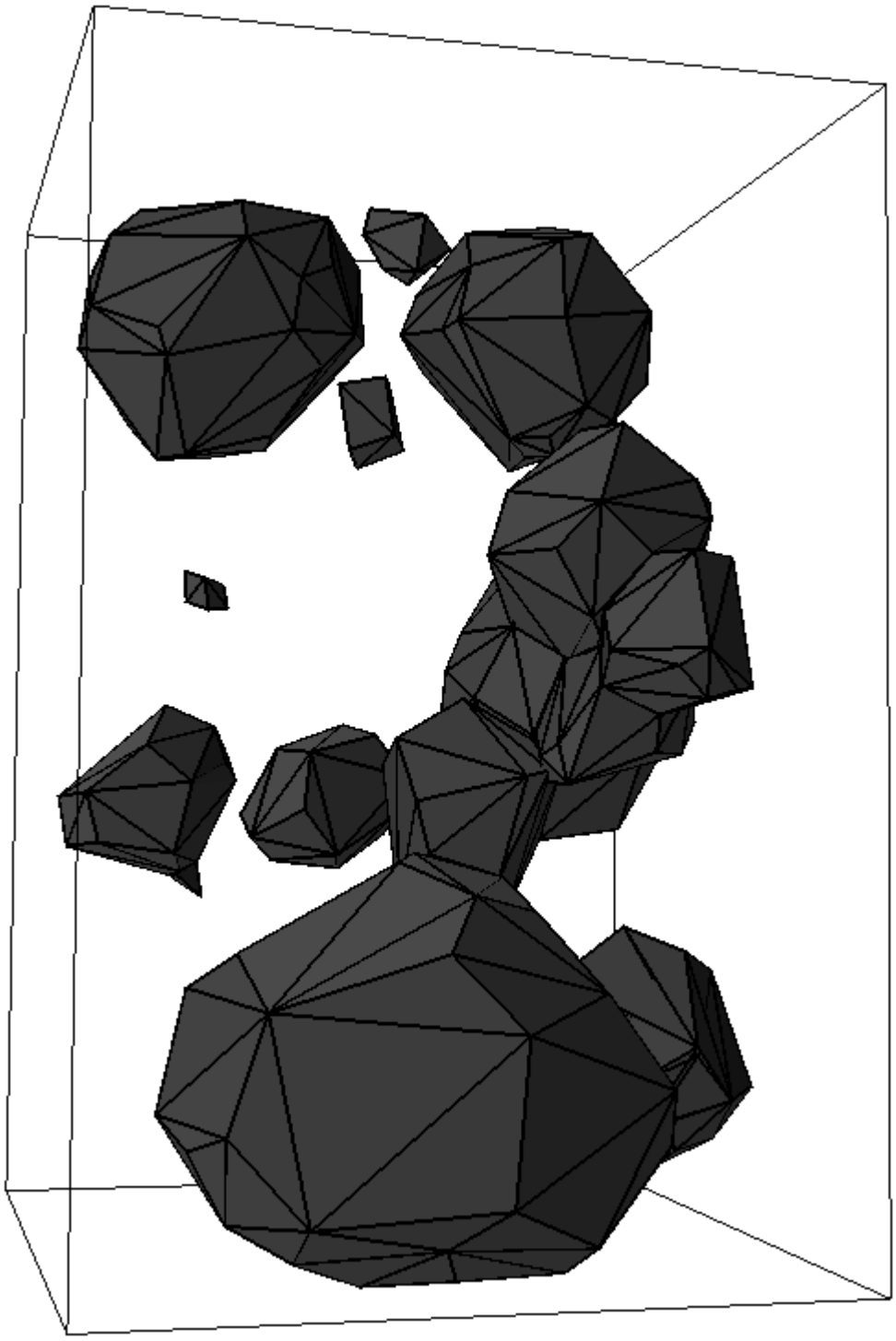

Figure 5.1. Hull Reconstruction: A set of hulls constructed around some of the bubbles traced in foam-2-02 run 32. The tracing and reconstruction method can even discern bubbles as small as 36 voxels^3 in size.

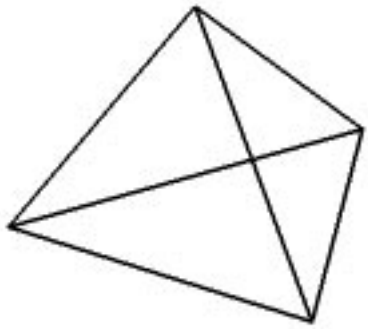

Figure 5.2. Regular Tetrahedra: The smallest distinguishable bubbles in the foams were several regular tetrahedra, with a volume of 36 voxels.

of the Weaire-Phelan partition, and have been observed before. Data run 32 in experiment foam-2-02 contained two such structures, one of which is shown in Figure 5.4. The two dodecahedra were very irregular, and not connected. Four more dodecahedra occurred in other data runs of foam-2-02 and foam-10-16.

The data confirm earlier observations that neither Kelvin's nor Weaire-Phelan's space filling partitions are present in disordered liquid foams. The global level of disorder, which was considerable in the foams we inspected, may not allow ordered structures to emerge. Matzke and Monnereau went to great pains to ensure that their foams were very homogeneous. Nonetheless they found not one of the predicted structures. This lack leads us to conclude that even a minor perturbation in a foam's homogeneity prevents the structure from evolving to what we believe is a minimal energy state. The freedom to evolve appears to be limited.

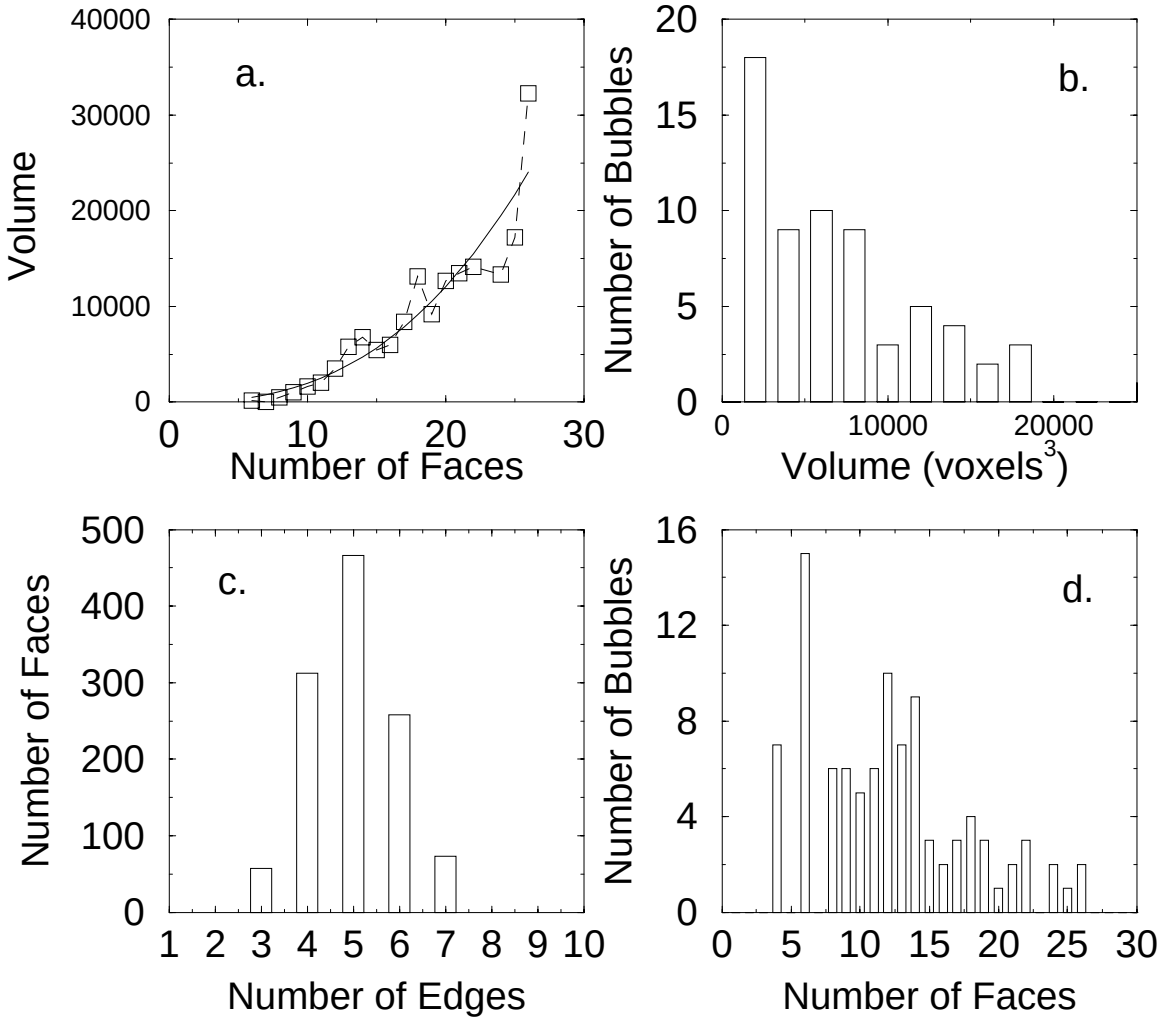

Figure 5.3. Distributions: a.) $\langle V_f \rangle$, b.) $\rho(V)$, c.) $\rho(n)$, d.) $\rho(f)$

.

Interestingly, the sample we investigated most thoroughly, foam-2-02, started out with fairly homogeneous (see experiment summary in chapter 3) bubble sizes ($d = 2.0mm \pm 0.3mm$). The disorder in the numbers of faces, $\mu_2(f)$ decreases over time, as shown in Figure 5.7, while the distribution of volumes increases (as some bubbles shrink, while others expand).

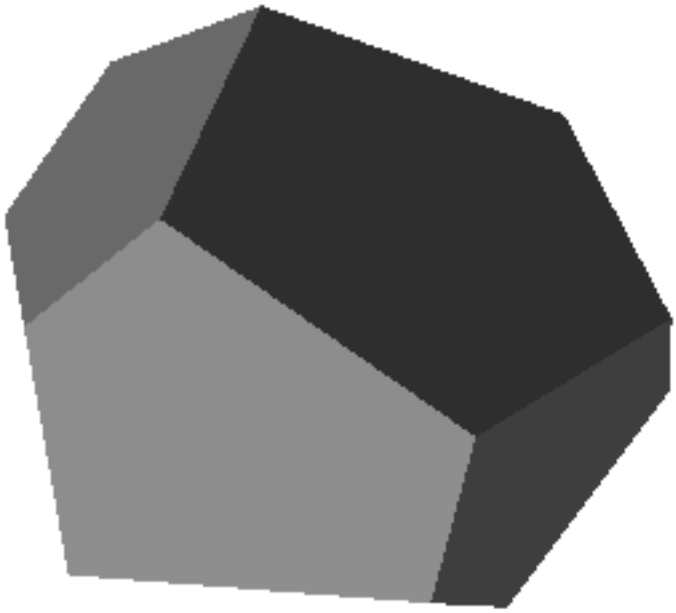

Figure 5.4. Irregular Pentagonal Dodecahedron: The only component of the Weaire-Phelan partitions observed in a disordered foam.

5.2 The Growth Law for Three-Dimensional Grains

The information obtained from tracking individual bubbles, and recording f and V(t) for bubbles that do not change their number of faces between data runs, allows us to investigate Glazier's growth law in Equation (5.1) directly. Computing the

derivative of Equation (5.1) for constant topology yields for the volume rate of change:

$$\frac{\mathrm{dV}_f^{2/3}}{\mathrm{dt}} = \kappa(f - f_0). \tag{5.3}$$

Figure 5.5 shows the volume rate of change as a function of f for the three experiments. The values calculated for the diffusion coefficient κ and the zero growth value f_0 are shown in Table 5.2. For comparison f_0 is also calculated using Equation 5.2. The values for f_0 found by the two methods for the three samples are consistent with each other, due to the large error in the volume determination used in Equation 5.3.

Table 5.2. Growth Law Results

	foam10_16	foam1_21	foam2_02
κ (10^{-6}mm^2/s)	7.33 ± 2.43	7.21 ± 2.83	7.42 ± 1.98
f_0 (graph)	11.6 ± 3.8	10.9 ± 4.3	12.1 ± 3.2
f_0 (Equation 5.2)	14.1 ± 0.3	14.8 ± 0.6	14.9 ± 0.5

The diffusion coefficient κ depends upon the fixed diffusion constant for the liquid in the sample, as well as the surface tension of the separating walls. While the samples initially have different liquid content and degree of polydispersity, the samples drain sufficiently quickly that liquid filled Plateau borders obstruct only a small fraction of the thin membranes of the walls, through which diffusion occurs. Because the wetness during imaging is similar, κ is the same for all three samples. We can thus combine the statistics from all three experiments for the volume rate of change as a function of f. Figure 5.6 shows the combined rate of change. The error in the slope $\kappa = 6.0 * 10^{-2} \frac{mm^2}{s} \pm 1.1 * 10^{-2} \frac{mm^2}{s}$ decreases by a factor $\sqrt{3}$. The zero growth intercept increases to $f_0 = 12.2 \pm 2.2$.

The value for f_0 is lower, but within error of the values found by using Equation 5.2 and by optical tomography [41].

While the spread in the growth rates for fixed f is considerable, they are consistent with a non-zero, linear slope. The linearity of the computed derivative in f strongly supports the linear dependence on topology of Glazier's growth law. The large error in our volume determination made it difficult to determine whether the scatter in the growth rate was intrinsic or due to measurement error. After combining the results from three independent measurements, the standard deviation of growth rates within a topological class remained the same, while we would expect a $\frac{1}{\sqrt{N}}$ dependence if it resulted from random measurement errors. This result suggests that the volume scatter is intrinsic, *i.e.* that the law holds only on average, not for individual bubbles, as in the Potts model.

Figure 5.7 shows the development of the average number of faces $\langle f \rangle$, the zero growth intercepts f_0 and the second moment $\mu_2(f)$ over time for all three experiments. The variance in f is very large initially, particularly in foam-1-21, which we began analyzing after 300 minutes. The variance in f decreases in all three samples and reaches values around 17 after some 3000 minutes. The average number of faces stays constant for all samples.

5.3 Conclusions

Magnetic Resonance Imaging is a rapidly developing experimental technique. Research is on the way to extend the performance envelope and application range of MRI in many fields. In this spirit our success in imaging liquid foams attains considerable significance.

MRI can be used for near microscopic applications, with linear resolutions of a few tens of microns becoming standard at high primary $\mathbf{B}$ fields. Volumetric imaging

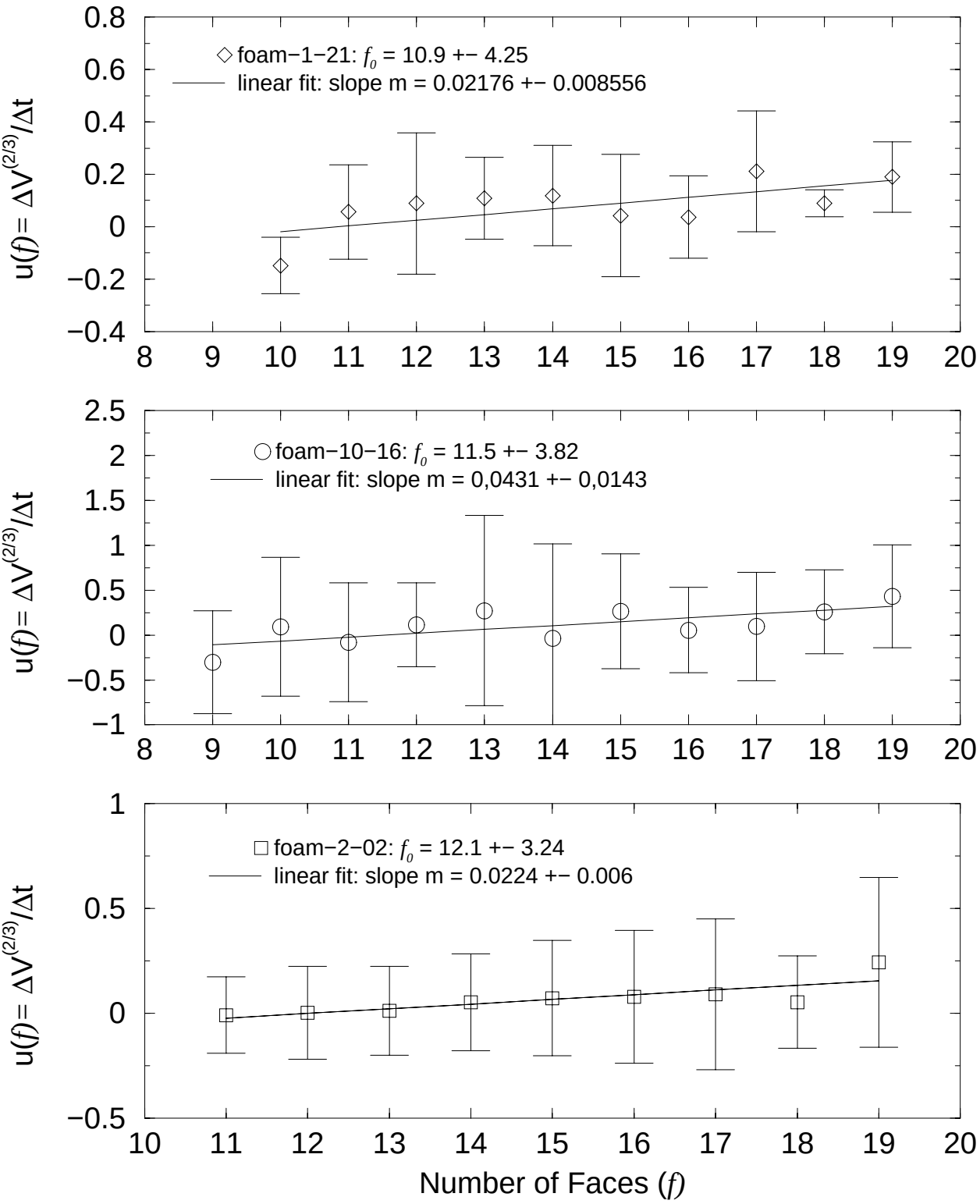

Figure 5.5. Volume Rates of Change as a Function of *f*: Three independent experiments.

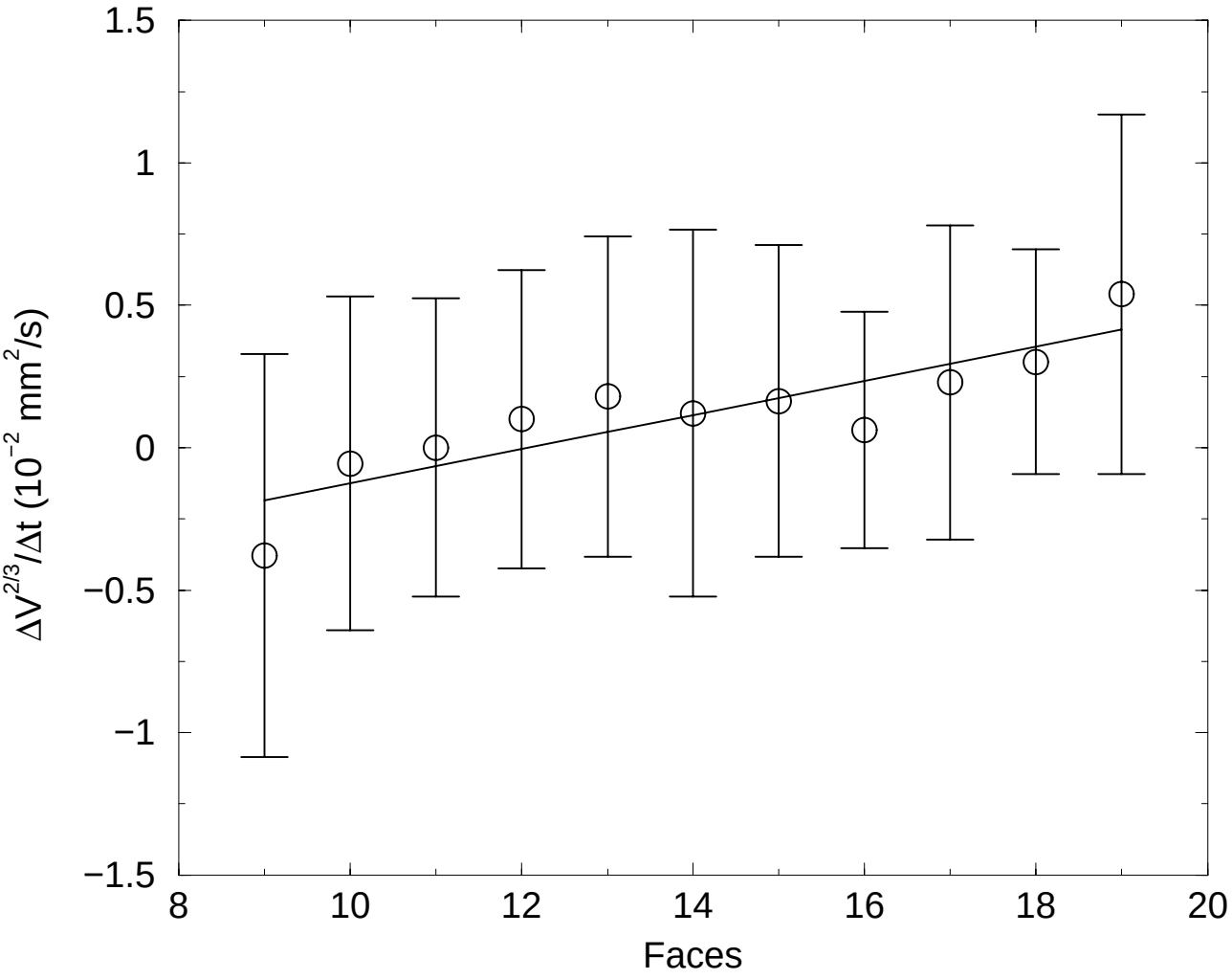

Figure 5.6. Combined Volume Rates of Change vs. *f*.

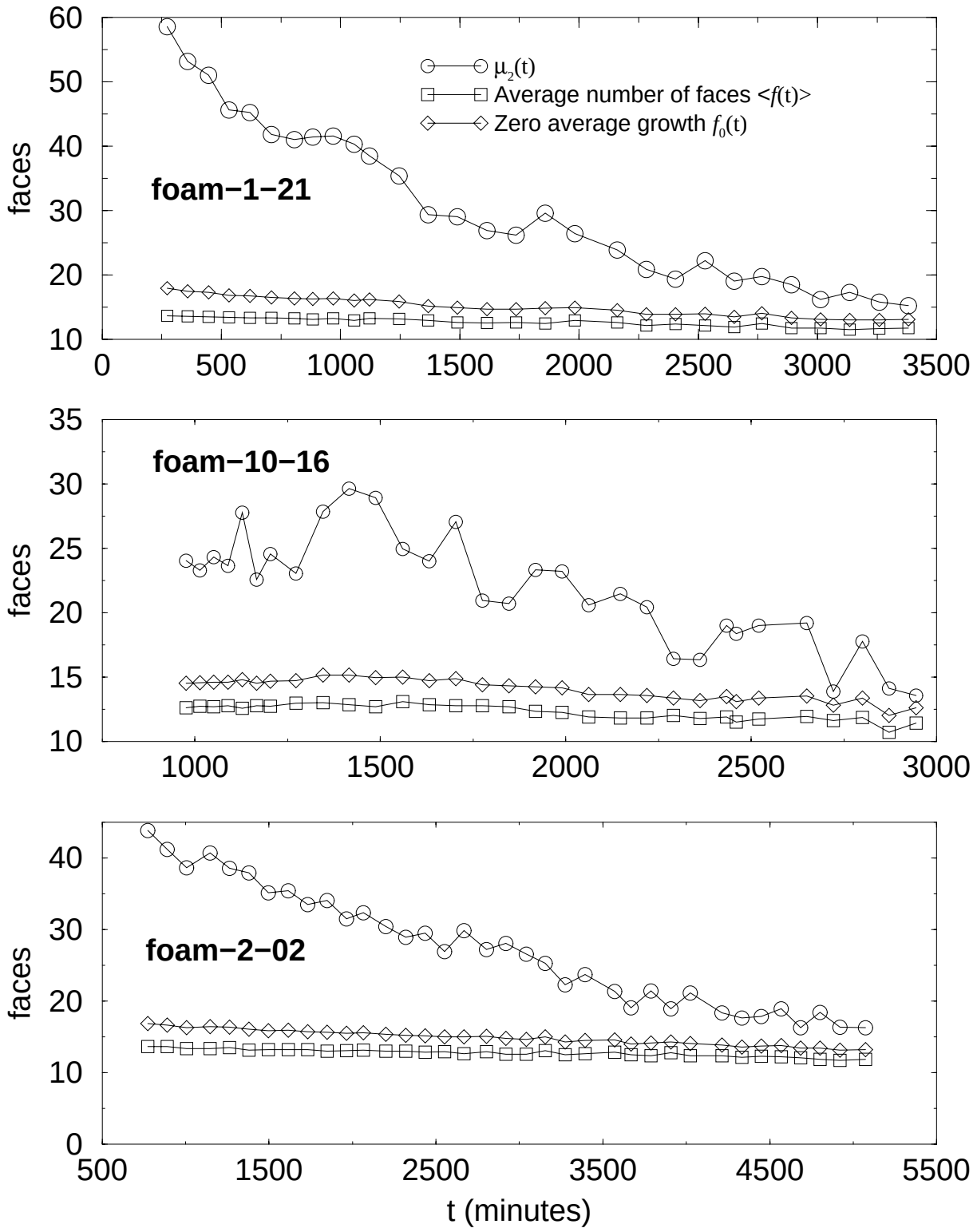

Figure 5.7. Time Evolution of the Numbers of Faces in Foams: The graphs show the evolution of the disorder (variance) in f, μ_2, the average number of faces $\langle f \rangle$, and the zero growth intercept f_0 for the three experiments.

in biological environments can be achieved in just a few seconds. Even solids can be imaged given appropriate hardware and sufficient time.

Our experiments for the first time combined a series of capabilities of MR imagers, to successfully image a material that is intrinsically hostile to this method of visualization.

Imaging of materials with low proton densities is difficult. Magnetically inhomogeneous conditions, such as those created by solids or multiple phases, are even more problematic. Adding to that imaging time constraints, caused by the temporal evolution of the foam, and the need for the entire three-dimensional structure of the subject, creates a set of uniquely restrictive conditions. We believe imaging of extended time series under such conditions has not been attempted in MRI anywhere before.

The experimental procedure, including consideration of the liquid's properties, signal optimization, careful preparation and control of environmental factors, is a useful study in the complexities of MRI experiments. The technique is a success, enabling us to study foams with well below 1% volume liquid fraction, while maintaining reasonably short integration times, and while keeping the samples stable for several days.

The images we obtained of liquid foams are themselves a success, showing the capability of MRI to accurately visualize three-dimensional complex structures that evolve in time.

Automated structural analysis from a sparse three-dimensional network of connected domains presents a challenging problem. Our methods show workable approaches, which can be used for many similar materials, such as asphalt and concrete, bone, ceramics and a multitude of granular materials. Hand tracing distinguishes very small bubbles, with volumes near the MRI resolution limit. It also

allows faithful reconstruction of bubble shapes. Values for $\langle f \rangle$, f_0, and growth exponents for $V(f)$ and $V(t)$, are fairly accurate. The method is too labor intensive to determine the time evolution of large numbers of bubbles.

Automated analysis using Euclidean distance maps and Delauney triangulations is computation intensive. Its current implementation loses small bubbles because it requires absolutely noise free data. In future experiments we can improve the large error bars for f_0 by slowing coarsening rates and further reducing imaging times. Faster imaging will allow us to track more bubbles between rearrangements, improving statistics. To improve our volume estimates, we are currently incorporating a three-dimensional Voronoi tessellation [107] into our automated analysis, to reconstruct exact hulls around individual bubbles as in our manual method.

The verification of Glazier's growth law for three-dimensional grains should aid rational metallurgy, in which the growth rate of domains cannot be observed directly.

5.3.1 Future Improvements

With analysis of several data runs complete, we can identify two areas to improve future experiments:

1. We need to extend the time during which we observe foam coarsening. More precisely, we need to look at a larger total volume change over time, preferably over two decades or more. This would require us to generate smaller polyhedral bubbles initially. A less viscous base liquid, combined with an attempt to slow its coarsening rate through careful temperature control may be the answer.

2. The temporal resolution between consecutive data runs is currently only marginally acceptable. Too many topological changes occur during a single acquisition to make tracing of topologically constant bubbles efficient. The sequence we currently use will allow further decreases in repetition time, requiring further T1

adjustments inside the sample. Tradeoffs in T2 will have to be evaluated, but it should be possible to achieve nearly twice the acquisition rate we currently employ. A more challenging approach would be to rewrite the acquisition method to allow multiple echoes (similar to the echo trains of a CPMG pulse train used in NMR spectroscopy), or to use technically difficult low flip angle spin-echo acquisitions, which allow much faster repetitions.

BIBLIOGRAPHY

[1] R. A. Komoroski, "Nonmedical Applications of NMR Imaging," Analytical Chemistry **65,** 1068A–1077A (1993).

[2] H. Pereira, M. E. Rosa, and M. A. Fortes, "The Cellular Structure of Cork from Quercus Suber L.," IAWA Bulletin **8,** 212–217 (1987).

[3] J. Bernholc, "Computational Material Science: The Era of Applied Quantum Mechanics," Physics Today **52,** 30–35 (1999).

[4] F. T. Lewis, "The Geometry of Growth and Cell Division in Columnar Parenchyma," Am. J. of Botany **31,** 619–629 (1944).

[5] J. C. M. Mombach, M. A. Z. Vasconcellos, and R. M. C. de Almeida, "Arrangements of Cells in Vegetable Tissue," J. Phys. D **23,** 600–606 (1990).

[6] A. M. Kraynik, "Foam Flows," Ann. Rev. Fluid Mech. **20,** 325–357 (1988).

[7] D. A. Reinelt and A. M. Kraynik, "On the Shearing Flow of Foams and Concentrated Emulsions," J. Fluid Mech. **215,** 431–455 (1990).

[8] D. A. Reinelt and A. M. Kraynik, "Simple Shearing Flow of a Dry Kelvin Soap Foam," J. Fluid Mech. **311,** 327–343 (1996).

[9] J. A. Glazier, Ph.D. thesis, University of Chicago, 1989.

[10] M. Hasegawa and M. Tanemura, "On the Pattern of Space Division by Territories," Ann. Inst. Statist. Math. **28,** 509–519 (1976).

[11] K. J. Dormer, *Fundamental Tissue Geometry for Biologists* (Cambridge University Press, Cambridge, 1980).

[12] A. Spry, "The Origin of Columnar Jointing, Particularly in Basalt Flows," J. Geol. Soc. Australia 8 (1961).

[13] W. B. Krantz, K. J. Gleason, and N. Caine, "Patterend Ground," Sci. Am. **259,** 68–76 (1988).

[14] S. A. Drury, *Image Interpretation in Geology* (Allen and Unwin, London, 1987).

[15] C. S. Smith, "Grain shapes and other metallurgical applications of topology," In *Metal Interfaces*, pp. 65–108 (American Society for Metals, Cleveland, 1952).

[16] F. T. Lewis, "The Analogous Shapes of Cells and Bubbles," Proc. Amer. Acad. Arts and Sci. **77,** 147–186 (1949).

[17] F. T. Lewis, "A Further Study of the Polyhedral Shapes of Cells," Proc. Amer. Acad. Arts and Sci. **61,** 1–34 (1925).

[18] F. T. Lewis, "A Geometric Accounting for Diverse Shapes of 14-Hedral Cells: The Transition from Dodecahedra to Tetrakaidecadhedra," Am. J. of Botany **30,** 74–81 (1943).

[19] Y. Jiang, Ph.D. thesis, University of Notre Dame, 1998.

[20] P. Ball, *The Self-Made Tapestry* (Oxford University Press, Oxford, 1999).

[21] J. Cassidy, *The Unbelievable Bubble Book* (Klutz Press, Palo Alto, 1987).

[22] D. Lovett, *Demonstrating Science with Soap Films* (IOP Publishing, Bristol, 1994).

[23] C. Isenberg, *The Science of Soap Films and Soap Bubbles* (Dover publications, 1992).

[24] N. Rivier, "Statistical Crystallography Structure of Random Cellular Networks," Philos. Mag. B **52,** 795–819 (1985).

[25] N. Rivier, "Statistical Geometry of Tissues," in *Thermodynamics and Pattern Formation in Biology* (Walter de Gruyter, Berlin, 1988), pp. 415–455.

[26] J. Stavans, "the Evolution of Cellular Structures," Rep. Prog. Phys. **56,** 733–789 (1993).

[27] D. Weaire, S. Hutzler, and N. Pittit, "Cylindrical Packings of Foam Cells," Forma **7,** 259–263 (1992).

[28] D. Weaire and R. Phelan, "The Structure of Monodisperse Foam," Philos. Mag. Lett. **70,** 345–350 (1994).

[29] D. Weaire and R. Phelan, "A Counter-Example to Kelvin's Conjecture on Minimal Surfaces," Phil. Mag. Lett. **69,** 107–110 (1994).

[30] D. Weaire, "Structural Transformations in Foam?," Phil. Mag. Lett. **69,** 99–105 (1994).

[31] D. Weaire and R. Phelan, "Cellular Structures in Three Dimensions," Phil. Trans. R. Soc. Lond. A **354,** 1989–1997 (1996).

[32] D. Weaire, *The Kelvin Problem* (Francis & Taylor, London, 1996).

[33] S. Hutzler, D. Weaire, and R. Crawford, "Moving Boundaries in Ordered Cylindrical Foam Structures," Philos. Mag. B **75,** 845–857 (1997).

[34] D. Weaire and R. Phelan, "Vertex Instabilities in Foams and Emulsions," J. Phys. Condens. Matt. **8,** L37–L43 (1996).

[35] D. Weaire, S. Findlay, and G. Verbist, "Measurement of Foam Drainage using AC Conductivity," J. Phys. Condens. Matter **7,** L217–L222 (1995).

[36] D. Weaire, S. Hutzler, G. Verbist, and E. Peters, "A Review of Foam Drainage," Advances in Chemical Physics **102,** 315–373 (1997).

[37] S. Findlay, Ph.D. thesis, University of Dublin, 1997.

[38] J. A. Glazier, "Grain Growth in Three Dimensions Depends on Grain Topology," Phys. Rev. Lett. **70,** 2170–2173 (1993).

[39] D. Weaire and J. A. Glazier, "Relations Between Volume, Number of faces and Three-dimensional Growth laws in Coarsening Cellular patterns," Phil. Mag. Lett. **68,** 363–365 (1993).

[40] C. Sire, "Growth laws for 3D Soap Bubbles," Phys. Rev. Lett. **72,** 420–423 (1994).

[41] C. Monnereau and M. Vignes-Adler, "Dynamics of Real 3D Foam Coarsening," Phys. Rev. Lett. **80,** 5228–5231 (1998).

[42] R. M. C. de Almeida and J. C. M. Mombach, "Scaling Properties of Three-Dimensional Foams," Physica A **236,** 268–278 (1997).

[43] D. J. Durian, D. A. Weitz, and D. J. Pine, "Dynamics and Coarsening in Three-Dimensional Foams," J. Phys. Condens. Matt. **2,** SA433–SA436 (1990).

[44] D. J. Durian, D. A. Weitz, and D. J. Pine, "Multiple Light-Scattering Probes of Foam Structure and Dynamics," Science **252,** 686–688 (1991).

[45] D. J. Durian, D. A. Weitz, and D. J. Pine, "Scaling Behavior in Shaving Cream," Phys. Rev. A **44,** R7902–R7905 (1991).

[46] C. P. Gonatas, J. S. Leigh, A. G. Yodh, J. A. Glazier, and B. Prause, "Magnetic Resonance Images of Coarsening Inside a Foam," Phys. Rev. Lett. **75,** 573–576 (1995).

[47] D. W. Thompson, *On Growth and Form* (Cambridge University Press, Cambridge, 1942).

[48] J. A. F. Plateau, *Statique Expérimentale et Théoretique des Liquides Soumis aux Seules Forces Molécularies* (Gauthier-Villars, 1873).

[49] L. Kelvin, "On the Division of Space with Minimal Partitional Area," Philos. Mag. **24,** 503–515 (1887).

[50] E. B. Matzke, "The Three Dimensional Shape of Bubbles in Foam. An Analysis of the Role of Surface Forces in Three Dimensional Cell Shape Determination," Am. J. Bot. **33,** 58–80 (1946).

[51] E. B. Matzke, "Volume-Shape Relationship in Variant Foams. A Further Study of the Role of Surface Forces in Three Dimensional Cell Shape Determination," Am. J. Bot. **33,** 130–144 (1946).

[52] K. Kose, "3D NMR Imaging of Foam Structures," Journal of Magnetic Resonance A **118,** 195–201 (1996).

[53] C. Monnereau and M. Vignes-Adler, "Optical Tomography of Real 3-Dimensional Foams," J. Colloid Interface Sci. **202,** 45–53 (1998).

[54] N. Rivier, "Kelvin's Conjecture on Minimal Froths and the Counter-Example of Weaire and Phelan," Phil. Mag. Lett. **69,** 297–303 (1994).

[55] J. von Neumann, "Discussion," In *Metal Interfaces*, pp. 108–110 (American Society for Metals, Cleveland, 1952).

[56] J. Stavans and J. A. Glazier, "Soap Froth Revisited: Dynamic Scaling in the Two-Dimensional Froth," Phys. Rev. Lett. **62,** 1318–1321 (1989).

[57] J. A. Glazier, M. P. Anderson, and G. S. Grest, "Coarsening in the Two-Dimensional Soap Froth and the Large-Q Potts Model: a Detailed Comparison," Phil. Mag. B **62,** 615–645 (1990).

[58] M. O. Magnasco, "Two-Dimensional Bubble Rafts," Phil. Mag. B **65,** 895–920 (1992).

[59] M. Seul and C. A. Murray, "Scale Transformation of Magnetic Bubble Arrays: Coupling of Topological Disorder and Polydispersity," Science **262,** 558–560 (1993).

[60] E. M. Purcell, H. C. Torrey, and R. V. Pound, "Resonance Absorption by Nuclear Magnetic Moments in a Solid," Phys. Rev. **69,** 37–38 (1946).

[61] F. Bloch, W. W. Hansen, and M. Packard, "Nuclear Induction," Phys. Rev. **69,** 127 (1946).

[62] F. Bloch, "Nuclear Induction," Phys. Rev. **70,** 460–474 (1946).

[63] F. Bloch, W. W. Hansen, and M. Packard, "The Nuclear Induction Experiment," Phys. Rev. **70,** 474–488 (1946).

[64] N. Bloembergen, E. M. Purcell, and R. V. Pound, "Relaxation Effects in Nuclear Magnetic Resonance Absorption," Phys. Rev. **73,** 679–694 (1948).

[65] E. L. Hahn, "Spin Echoes," Physical Review **80,** 580–594 (1950).

[66] H. Y. Carr and E. M. Purcell, "Effects of Diffusion on Free Precession in Nuclear Magnetic Resonance Experiments," Physical Review **94,** 630–638 (1954).

[67] R. C. Ferguson and W. D. Phillips, "High-resolution Nuclear Magnetic Resonance Spectroscopy," Science **157,** 257–267 (1967).

[68] M. Goldman, *Quantum Description of High-Resolution NMR in Liquids* (Clarendon Press, Oxford, 1988).

[69] E. Fukushima and S. B. W. Roeder, *Experimental Pulse NMR - A Nuts and Bolts Approach* (Addison-Wesley, Reading, 1981).

[70] *Advances in Magnetic Resonance*, J. S. Waugh, ed., (Academic Press, New York, 1976), Vol. 8.

[71] *Advances in Magnetic Resonance*, J. S. Waugh, ed., (Academic Press, New York, 1988), Vol. 12.

[72] P. C. Lauterbur, "Image Formation by Induced Local Interactions: Examples Employing Nuclear magnetic resonance," Nature **242,** 190–191 (1973).

[73] P. Mansfield and P. K. Grannell, "NMR Diffraction in Solids?," J. Phys. C: Solid State Phys. **10,** L55–L58 (1973).

[74] A. D. Elster, *Questions and Answers in Magnetic Resonance Imaging* (Mosby-Year Book, St. Louis, 1994).

[75] M. NessAiver, *All you really need to know about MRI physics* (Simply Physics, Baltimore, 1997).

[76] P. Woodward and W. W. O. Jr., *MRI Optimization* (McGraw-Hill, New York, 1997).

[77] M. R. Prince, T. M. Grist, and J. F. Debatim, *3D Contrast MR Angiography* (Springer Verlag, Berlin, 1999).

[78] P. Mansfield and P. Morris, *NMR Imaging in Biomedicine* (Academic Press, New York, 1982).

[79] *NMR in Biology and Medicine*, S. Chien and C. Ho, eds., (Raven Press, New York, 1986).

[80] *Biomedical Magnetic Resonance Imaging. Principles, Methodology and Application*, F. W. Wehrli, D. Shaw, and J. B. Kneeland, eds., (VCH Publishers, Weinheim, 1988).

[81] *Magnetic Resonance Spectroscopy in Biology and Medicine*, J. D. de Certaines, W. M. M. J. Bovée, and F. Podo, eds., (Pergamon Press, 1992).

[82] W. Kuhn, "NMR Microscopy - Fundamentals, Limits and Possible Applications," Angew. Chem. **29,** 1–19 (1990).

[83] P. T. Callaghan, *Principles of Nuclear Magnetic Resonance Microscopy* (Clarendon Press, Oxford, 1991).

[84] S. Gravina and D. G. Cory, "Sensitivity and Resolution of Constant-Time Imaging," J. Mag. Res. B **104,** 53–61 (1994).

[85] P. Blümler and B. Blümlich, "Aging and Phase Seperation of Elastomers Investigated by NMR Imaging," Macromolecules **24,** 2183–2188 (1991).

[86] J. R. Heil, M. Özilgen, and M. J. McCarthy, "Magnetic Resonance Imaging Analysis of Water Migration and Void Formation in Baking Biscuits," Food Dehydration, AIChE Symposium Series **89,** 39–45 (1993).

[87] J. B. German and M. J. McCarthy, "Stability of Aqueous Foams: Analysis Using Magnetic Resonance Imaging.," J. Agric. Food Chem. **37,** 1321–1324 (1989).

[88] J. R. Heil, K. L. McCarthy, J. B. German, and M. J. McCarthy, "Use of Magnetic Resonance Imaging for Evaluation of Beer Foam Characteristics," J. American Society of Brewing Chemists **48,** 119–122 (1990).

[89] M. S. Albert, G. D. Cates, B. Driehuys, W. Happer, B. Saam, C. S. S. Jr, and A. Wishnia, "Biological Magnetic Resonance Imaging Using Laser-Polarized ^{129}Xe," Nature **370,** 199–201 (1994).

[90] B. Saam, N. Drukker, and W. Happer, "Edge Enhancement Observed with Hyperpolarized ^{3}He," Chem. Phys. Lett. **263,** 481–487 (1996).

[91] Y.-Q. Song, H. C. Gaede, T. Pietraß, G. A. Barrall, G. C. Chingas, M. R. Ayers, and A. Pines, "Spin-Polarized ^{129}Xe Gas Imaging of Materials," J. Magn. Res. A **115,** 127–130 (1995).

[92] M. S. Albert and D. Balamore, "Development of Hyperpolarized Noble Gas Imaging," Nucl. Instr. and Meth. in Phys. Res. A **402,** 441–453 (1998).

[93] R. A. Assink, A. Caprihan, and E. Fukushima, "Density Profiles of a Draining Foam by Nuclear Magnetic Resonance Imaging," AIChE Journal **34,** 2077–2079 (1988).

[94] B. A. Prause, J. A. Glazier, S. J. Gravina, and C. D. Montemagno, "Three-Dimensional Magnetic Resonance Imaging of a Liquid Foam," J. Phys. Condens. Matter **7,** L511–L516 (1995).

[95] J. C. Russ, *The Image Processing Handbook* (CRC Press, Boca Raton, 1995).

[96] *ParaVision Manual*, 1.1.4 ed., Bruker Medizintechnik, 1996.

[97] M. J. McCarthy, "Interpretation of the magnetic resonance Imaging Signal from a Foam," AIChE Journal **36,** 287–290 (1990).

[98] B. A. Prause, J. A. Glazier, and S. J. Gibbs, "Magnetic Resonance Imaging of Foams," In *National High Magnetic Field Laboratory 1996 Annual Report*, pp. 121–122 (NHMFL, Tallahassee, 1996).

[99] *Three Dimensional Surface Topography: Measurement, Interpretation and Applications*, K. J. Stout, ed., (Penton Press, London, 1994).

[100] E. Trucco, *Introductory Techniques for 3D Computer Vision* (Prentice Hall, Upper Saddle River, 1998).

[101] D. Scharstein, *View Synthesis Using Stereo Vision* (Springer, New York, 1999).

[102] L. Wojnar, *Image Analysis Applications in Materials Engineering* (CRC Press, Boca Raton, 1999).

[103] J. Serra, *Image Analysis and Mathematical Morphology* (Academic Press, London, 1982).

[104] *IDL Reference Guide*, Research Systems, Inc., Boulder, CO.

[105] C. B. Barber, D. P. Dobkin, and H. T. Huhdanpaa, "The Quickhull Algorithm for Convex Hulls," ACM Transactions on Mathematical Software **22,** 469–483 (1996).

[106] P. E. Danielsson, "Euclidian Distance Mapping," Comput. Graphics Image Proc. **14,** 227–248 (1980).

[107] F. Aurenhammer, "Voronoi Diagrams - a Survey of a Fundamental Geometric Data Structure," ACM Computing Surveys **23,** 345–405 (1991).